Fracture of a Brittle-Particle Ductile Matrix Composite with Applications to a Coating System

Submitted in Partial Fulfillment of the Requirements

For the Degree of

DOCTOR OF PHILOSOPHY

in

MECHANICAL ENGINEERING

STEVEN J. BIANCULLI

B. S., Mechanical Engineering, University of Pittsburgh

M. S., Mechanical Engineering, University of Pittsburgh

Carnegie Mellon University
Pittsburgh, Pennsylvania
May, 2016

Abstract

In material systems consisting of hard second phase particles in a ductile matrix, failure initiating from cracking of the second phase particles is an important failure mechanism. This dissertation applies the principles of fracture mechanics to consider this problem, first from the standpoint of fracture of the particles, and then the onset of crack propagation from fractured particles. This research was inspired by the observation of the failure mechanism of a commercial zinc-based anti-corrosion coating and the analysis was initially approached as coatings problem. As the work progressed it became evident that failure mechanism was relevant to a broad range of composite material systems and research approach was generalized to consider failure of a system consisting of ellipsoidal second phase particles in a ductile matrix.

The starting point for the analysis is the classical Eshelby Problem, which considered stress transfer from the matrix to an ellipsoidal inclusion. The particle fracture problem is approached by considering cracks within particles and how they are affected by the particle/matrix interface, the difference in properties between the particle and matrix, and by particle shape. These effects are mapped out for a wide range of material combinations. The trends developed show that, although the particle fracture problem is very complex, the potential for fracture among a range of particle shapes can, for certain ranges in particle shape, be considered easily on the basis of the Eshelby Stress alone. Additionally, the evaluation of cracks near the curved particle/matrix interface adds to the existing body of work of cracks approaching bi-material interfaces in layered material systems.

The onset of crack propagation from fractured particles is then considered as a function of particle shape and mismatch in material properties between the particle and matrix. This behavior is mapped out for a wide range of material combinations. The final section of this dissertation qualitatively considers an approach to determine critical particle sizes, below which crack propagation will not occur for a coating system that exhibited stable cracks in an interfacial layer between the coating and substrate.

Acknowledgements

Table of Contents

List of Illustrations

List of Tables

Nomenclature

A	crack face area
a	ellipsoidal particle half-height, crack half-length
b	ellipsoidal particle half-length
c	ellipsoidal particle half-depth
b/a	ellipsoidal particle aspect ratio
h	coating thickness
E	Young's modulus
Ep	particle Young's modulus
Em	matrix Young's modulus
Ep/Em	Young's modulus ratio
$E(k)$	elliptic integral of the second kind
G_I	mode I energy release rate
G_{Ic}	critical mode I energy release rate
$\overline{G_I}$	mode I average energy release rate
$\overline{G_{In}}$	normalized mode I average energy release rate
K_I	mode I stress intensity factor
K_{In}	normalized mode I stress intensity factor
K_{Ic}	critical mode I stress intensity factor (fracture toughness)
r	radial distance
$\upsilon(r)$	crack opening displacement
δ	displacement
ν	Poisson's ratio
σ	normal stress

Chapter 1

Introduction

1.1 BACKGROUND

The topic of this dissertation is the fracture of a two-phase composite system consisting of brittle particles in a ductile matrix. This research was inspired by observations of the fracture of GALVALUME^{R*}, an anti-corrosion coating for steel sheet that consists of a ductile metallic matrix containing brittle silicon particles. Fracture of this system occurred during bend forming of the coated sheet. The observed failure mode was brittle particle fracture followed by crack propagation through the matrix from the cracks introduced by particle fracture. Cracks that propagated entirely through the coating thickness would expose the steel substrate to environmental corrosion.

The GALVALUME^R coating is a multi-phase system formed in-situ as a molten zinc-aluminum alloy solidifies on a steel substrate, consisting primarily of hard, second phase (silicon) particles in a ductile (aluminum-zinc) matrix. The general morphology of GALVALUME^R is similar to and representative of a broad family of materials that consist of hard second phase particles in a ductile matrix. Examples include particulate reinforced metal matrix composites, where hard second phases particles are added to improve strength and stiffness, and various metal alloys where hard second phase precipitates are formed in situ either to enhance mechanical properties or as a byproduct of the production process. Although this research was initially inspired by the GALVALUME^R thin film problem, the problem considerer in this dissertation is much

---

* GALVALUME^R is an internationally registered trademark of BISC International, Inc. and some of its licensed producers.

1

more general and is applicable to the broad family of two phase brittle particle/ductile matrix material systems.

A significant body of literature pertaining to these materials, particularly for particulate reinforced metal matrix composites, exists. A literature review aimed at illustrating failure mechanisms of these materials is given in the next section.

1.2 LITERATURE REVIEW

One of the most common damage mechanisms associated with particulate reinforced metal matrix composites consists of damage events initiating at the particles and this also is the predominant failure mechanism observed for the GALVALUME^R system. It is generally accepted that particle fracture or particle-matrix debonding results in decreased stiffness, flow strength and ductility, ultimately leading to failure of the composite structure [1-14]]. Both particle fracture and particle-matrix debonding are void nucleation events that can lead to failure through void growth and coalescence, making damage initiation at particles the first in the sequence of events leading to failure of the composite system. Because of this, it is reasonable to expect that the factors that control damage initiation at particles are also controlling factors for overall failure.

In composite systems, for a given particle composition, particle size, shape, and, to a lesser extent, clustering are reported to be relevant factors affecting particle damage. It has been reported that larger particles fracture more easily than smaller particles [1,4,6,14,15], with this behavior attributed to a lower fracture stress for larger particles [6,14] or the presence of larger flaws in larger particles [10].

2

A number of authors have reported on the effects of particle shape [2,14,16,17,18,19,20]. In particular, Goods and Brown [19], reported that equiaxed particles debond (instead of fracturing) while higher aspect ratio particles fracture. The authors do not give a basis (particle size, volume, etc.) for particle comparison. Horstmeyer, et al. [17] conducted two-dimensional finite element analysis of circular and elliptical silicon particles in an aluminum matrix and considered particle fracture on the basis of maximum principal stress within the particle. Romanova, et al. [20] considered the fracture of spherical and irregular equiaxed particles with a maximum equivalent stress criterion. No fracture mechanics criterion was used in either of these analyses. Dighe, et al. [14] reported that higher aspect ratio particles fracture more easily than equiaxed or spherical particles. Particle clustering was also observed to have an effect on particle fracture, with particles in clusters more likely to fracture [6,10] because clustering results in elevated stress in the particles.

A number of studies have been conducted in which mathematical modeling was used to explain or predict the mechanical behavior of metal matrix composites. The primary aim of most of the work reviewed was to predict the overall stress-strain response of the composite system. Several studies focused on stress build-up or load transfer to particle reinforcements [9,21]. Others also included the effect of particle fracture on the tensile response [7,8,10,11,12,13,15,22,23,24,25,26]. In these studies, the primary focus was on the change in stress-strain behavior due to particle fracture, not the particle fracture event itself. Particles were either assumed to be fractured or fracture was governed by stress based criteria. Particle shapes studied included spheres, cylinders and ellipsoids.

Several numerical studies applying fracture mechanics, using cohesive zone simulations, to metal matrix composites were found in the literature. Finot et al. [1] compared the fracture of cylindrical and truncated cylindrical particles, along with subsequent crack growth through the matrix. Needleman et al.[3] examined void nucleation through the debonding of spherical inclusions and Zhai et al.[27] examined crack growth in alumina/titanium diboride composites. Systematic studies of the relationship between particle shape and particle fracture were not found in the literature either in relation to particles in a continuum or particles in coatings.

Although most of the literature reviewed dealt with metal matrix composite systems, another area of relevance dealt with fracture in steels. James et al. [28] and Ortner [29] considered the onset of cleavage fracture in the ductile-to-brittle transition region due to particle fracture in reactor pressure vessel steels. These authors considered particle fracture with a stress based statistical criterion which did not involve fracture mechanics. Particle size effects were considered but particle shape effects were not. Hauert et al. [30] conducted similar work for a metal matrix composite system.

While the literature review related to particle fracture considered monotonic loading, it is also noted that particle fracture has important implications for fatigue life of a composite system. Under cyclic loading conditions, fractured particles can serve as initiation sites for fatigue cracks, potentially resulting in significant reductions in fatigue life.

1.3   RESEARCH OBJECTIVES

The objective of this research is to investigate the fracture behavior two-phase composite system consisting of brittle particles in a ductile matrix.   While GALVALUME^R system is used as a model system for this research, the work is not focused on that particular coating system. Instead, observation of the GALVALUME^R system is used to define fracture mechanisms, which are then investigated with a combination of finite element analysis and analytic solutions. The work is generalized to consider alternate combinations of material properties for the matrix and particle inclusions.

Chapter 2 presents microstructural observations of GALVALUME^R and its fracture characteristics, which provide the basis for the research presented in the succeeding chapters. Chapter 3 investigates the role of particle shape and the mismatch in properties between the particle and matrix in particle fracture. Chapter 4 considers the onset of matrix crack propagation from particles after they have fractured. The analyses of Chapters 3 and 4 both consider a broad range of particle/matrix material property combinations. In Chapter 5 the observation that cracks in the GALVALUME^R intermetallic interface layer do not propagate is used to suggest particle sizes for which crack propagation will not occur for that particular system.

Chapter 2

GALVALUME^R Microstructure and Fracture

2.1 CHAPTER INTRODUCTION

In this dissertation, the GALVALUME^R coating system is used as a model system to study fracture of a general two phase brittle particle/ductile matrix coating system, with implications for analogous two phase composite materials. An experimental study to characterize the microstructure and fracture behavior of the GALVALUME^R system was conducted. This study evaluated nine types of commercially produced sheet samples. Four samples were produced by U. S. Steel Corporation, four by BHP and one by Galvalange. Two of the BHP samples contained low-level additions of strontium in the coatings. The coating produced by Galvalange contained a higher level of strontium, as well as vanadium. Strontium and vanadium have been used by several GALVALUME^R producers in an attempt to improve the fracture resistance of the coatings. The samples were strained in tension and examined metallographically with optical and scanning electron microscopes.

2.2 TEST MATRIX OF GALVALUME^R COATING SPECIMENS

The matrix of coating specimens is shown in Table 2.1. The four BHP samples are identified with the letters A, B, C and D. Samples A and B were 0.4 mm thick. Samples C and D were 0.6mm thick. One sample of each pair (A and C) contained a very low level of strontium, likely added more to improve wetting characteristics than to reduce cracking. These samples had also been temper rolled. The four U. S. Steel samples are

identified with the letters E, F, G and J. Samples E and F were produced by U. S. Steel Fairfield Works and the GALVALUME[R] coating contained 1.3 weight percent silicon. Samples G and J were produced by U. S. Steel Mon Valley Works and contained 1.7 weight percent silicon. Samples F and J were temper rolled. The differences in the silicon level between the Fairfield and Mon Valley samples were dictated by the process requirements of the respective coating lines. However, coatings with lower levels of silicon were thought to be more resistant to fracture. The final sample, GL, was produced by Galvalange and contains significant levels of strontium and vanadium.

2.3 TESTING PROGRAM

A set of tensile specimens was machined from each sample. The specimens were 4 inches long with a gage section that was 2 inches long and 0.5 inches wide. Specimens from each set were strained in tension to values of 3, 5, 7, 9, and 11 percent strain, respectively. An additional Galvalange sample was strained to 13 percent because that material exhibited a greater resistance to coating fracture.

To quantify the performance of the strained samples, it was necessary to create a standard for assessing the cracks. The primary concern for the GALVALUME[R] system was through-coating fracture that would expose the substrate to environmental corrosion. To compare the performance of the samples, the number of through-coating cracks was recorded for each sample. This was done through optical microscopy of 1/2-inch-long segments of the gage section that were mounted in cross-section and polished half way through the width of the specimen. To provide additional information, the number of cracks spanning more than one half of the coating thickness was also recorded.

2.4 TENSILE STRAINING RESULTS

2.4.1 Crack Frequency

The results of the optical microscopy evaluation are listed in Table 2.2 and plotted in Figure 2.1. The column headings in the table refer to the strain level and the type of crack. For example, the heading "3% thru" refers to through-coating cracks in samples strained to 3 percent while "3% half" refers to cracks that span at least one half (but not all) of the coating thickness in samples strained to 3 percent. For each column entry the total number of cracks recorded for the sample is listed in bold typeface. Following in parenthesis are the number of cracks recorded for the top and bottom surfaces, respectively. In all cases the identification of a surface as top or bottom is arbitrary.

The samples tested are all from large-scale production runs, therefore some degree of variability can be expected. Depending on factors such as particle size or possibly pre-existing damage, some through-coating cracking might be expected to occur at relatively low strain levels, even for coatings that exhibit a relatively high strain tolerance. For this reason coating strain tolerance is interpreted on the basis of the presence of a "significant" number of through-coating cracks with "significant" arbitrarily interpreted as more than a few (say two or three).

BHP samples C, and D both exhibited a significant number of through-coating cracks on the 7 percent strain specimens. The remaining samples exhibited significant cracking on the 11 percent samples.

The low level strontium additions seemed to have a beneficial effect for the BHP material with the strontium containing samples exhibiting a lesser degree of through

8

cracking at 11 percent strain, 25 versus 44 through cracks for the 0.4mm specimens and 33 versus 64 for the 0.6mm specimens. At lower strain levels the apparent benefit of the strontium additions to the BHP samples was not as clear. The 0.6 mm thick specimen at 7 percent strain without a strontium addition exhibited fewer through-coating cracks than the specimen with a strontium addition.

The effect of silicon level on the USS samples was not clear. The best performing USS sample, F with 9 through cracks at 11 percent strain, had the lower silicon level. The worst performing sample, J with 55 through cracks at 11 percent strain had the higher silicon level. However two remaining samples, one each with low and high silicon levels had similar amounts of cracking, 38 and 36 through-cracks at 11 percent strain respectively. Temper rolling, a light mechanical deformation, did not have a clear affect on the cracking behavior of the USS samples.

The Galvalange specimens (GL) with strontium and vanadium exhibited the best performance, 7 through-cracks at 11 percent strain (with none on one side). Because of this, an additional specimen was strained to 13 percent. This specimen exhibited 30 through-cracks, similar to the performance of many of the other samples at 11 percent strain.

2.4.2 Microstructural Observations

In addition to the analysis of crack frequency, a metallographic examination of the samples with a scanning electron microscope (SEM) was conducted. This was done to compare the microstructure of the various coatings and to examine crack morphology and determine if any dominant mechanisms that controlled the cracking existed.

Microstructural examination of the series of specimens showed a general similarity of appearance among the specimens. Representative examples are shown in Figures 2.2-2.6, while images of the remaining samples in the unstrained condition are shown in Figures 2.7-2.14.

The typical appearance of unstrained GALVALUME^R is shown in Figure 2.2. The coating system consists of four distinct phases: aluminum rich dendrites that comprise the bulk of the coating matrix, regions of zinc rich material that solidify in between the aluminum rich dendrites, silicon particles dispersed throughout the coating matrix, and an iron-zinc-aluminum-silicon alloy layer that forms between the bulk of the coating and the steel substrate.

Typical appearance of the strained specimens, excluding the Galvalange material, is shown in Figures 2.3 and 2.4. Silicon particles in the matrix have fractured. In some cases the fractured silicon particles served as initiation sites for continued crack propagation through the matrix, while in other cases the cracks open and blunt, and further propagation does not occur. In some cases cracks extended from the surface of the coating to the substrate and in GALVALUME^R applications such cracks would expose the substrate to environmental corrosion. The primary mechanism of GALVALUME^R coating fracture was identified as the initial fracture of silicon particles at relatively low strains followed by crack propagation into and through the coating matrix as the applied strain increases.

The Galvalange samples are shown in Figures 2.5 and 2.6. These samples, evidently as a consequence of the strontium and vanadium additions, exhibited a silicon particle morphology that was significantly different than what was observed in the other

GALVALUME[R] specimens. The particles were generally smaller and equiaxed and distributed in clusters, primarily in the zinc rich regions of the microstructure. The reduced size of the particles appears to have improved the fracture resistance of the particles and fracture appears to have propagated along the clusters of particles without fracture of the individual particles occurring.

Among the remaining samples, Figures 2.7-2.14 the only significant differences in appearance and particle morphology are with the BHP samples, some of which contained low level strontium additions. In the samples without strontium (B and D) the silicon particles are relatively long and angular while the particles in the strontium containing samples (A and C) appear to be somewhat more rounded. Samples A and C exhibited significantly few cracks than B and D and it would seem that the difference in particle shape is responsible for this.

While some variations in coating appearance can be seen for the U. S. Steel samples, Figures 2.11-2.14, no characteristics specific to any individual coating type were identified.

A secondary affect observed in the strained specimens is the behavior of the intermetallic alloy layer. In all cases, as shown in Figures 2.3-2.6, the intermetallic layer cracked extensively but these cracks did not propagate into the matrix. This observation appeared to be significant because it was theorized that the length of the intermetallic layer cracks, which is established by the thickness of the intermetallic layer, are below a threshold at for which crack propagation through the matrix could occur. It was further theorized that comparison of stress intensity factors for fractured particles and the

fractured intermetallic layer could offer insight toward identifying silicon particle sizes for which matrix crack propagation would not occur.

2.5 CONCLUSIONS

The primary conclusion of the tensile straining study of commercial GALVALUME[R] specimens is that silicon particle fracture is the primary event in the sequence of events that lead to fracture of the composite coating system. The silicon particles fracture at relatively low applied strains and these cracks, with additional applied strain, can propagate into and through the coating matrix. Improvements in fracture resistance were observed for the BHP samples that contained strontium and the Galvalange samples that contained strontium and vanadium. The effect of these additions was to modify the shape and size of the silicon particles and this observation indicates, along with findings of the literature review, that particle shape and size play a key role in particle fracture.

The fracture of the intermetallic layer is also potentially significant because, although the intermetallic layer cracks extensively, cracks through it do not propagate into the coating matrix. This suggests that the intermetallic layer thickness may be below a threshold for which matrix crack propagation would occur. Knowledge of this can provide insight into particle configurations, which, upon fracture, would not lead to further crack propagation.

Table 2.1

GALVALUME[R] Samples for Tensile Straining

Identifier	Sample	Si Level	Temper Rolling	Sr Addition	Vn Addition
A	BHP-0.4 mm	Unknown	Yes	Very Low	
B	BHP-0.42 mm	Unknown			
C	BHP-0.6 mm	Unknown	Yes	Very Low	
D	BHP-0.6 mm,	Unknown			
E	USS-AZ55 g50	Low			
F	USS-AZ55 g50	Low	Yes		
G	USS-AZ55 g50	High			
J	USS-Az55 g50	High	Yes		
GL	Galvalange	Unknown		Significant amt.	Significant amt.

Table 2.2

Number of Half- and Through-Thickness Cracks Observed in GALVALUME[R] Samples

		3% thru	3% half	5% thru	5% half	7% thru	7% half	9% thru	9% half	11% thru	11% half	13% thru	13% half
Sample													
A	BHP 0.4mm, Sr	**0**	**3** (1,2)	**1**(0,1)	**4**(2,2)	**2**(1,1)	**9**(7,2)	**1**(0,1)	**10**(3,7)	**25**(17,8)	**50**(25,25)	----------	----------
B	BHP 0.42mm, No Sr	**0**	**0**	**3**(1,2)	**11**(11,0)	**3**(1,2)	**21**(13,8)	**2**(0,2)	**13**(9,5)	**44**(25,19)	**66**(35,31)	----------	----------
C	BHP 0.6mm, Sr	**0**	**8**(2,6)	**0**	**2**(2,0)	**13**(5,8)	**18**(13,5)	**3**(0,3)	**13**(6,7)	**33**(10,23)	**46**(19,27)	----------	
D	BHP 0.6mm, No Sr	**1**(1,0)	**9**(4,5)	**2**(1,1)	**13**(6,7)	**9**(4,5)	**21**(8,13)	**12**(3,9)	**29**(17,12)	**64**(36,28)	**53**(26,27)	----------	----------
E	AZ55 g50 low Si	**2**(2,0)	**2**(2,0)	**0**	**5**(3,2)	**1**(1,0)	**5**(1,4)	**2**(0,2)	**18**(6,12)	**38**(21,17)	**41**(17,24)	----------	----------
F	AZ55 g50 low Si TM	**0**	**4**(3,1)	**0**	**5**(3,2)	**0**	**6**(3,3)	**2**(1,1)	**10**(7,3)	**9**(5,4)	**48**(20,28)	----------	----------
G	AZ55 g50 high Si	**0**	**0**	**0**	**1**(1,0)	**0**	**16**(7,9)	**0**	**13**(7,6)	**36**(15,21)	**46**(32,14)	----------	----------
J	Az55 g50 high Si TM	**1**(1,0)	**3**(2,1)	**0**	**4**(3,1)	**0**	**18**(11,7)	**3**(1,2)	**28**(13,15)	**55**(36,19)	**65**(42,23)	----------	----------
GL	Galvalange	**0**	**1**(1,0)-	**0**	**2**(1,1)	**0**	**1**(0,1)	**0**	**3**(2,1)	**7**(0,7)	**24**(7,17)	**30**(10,20)	**38**(17,21)
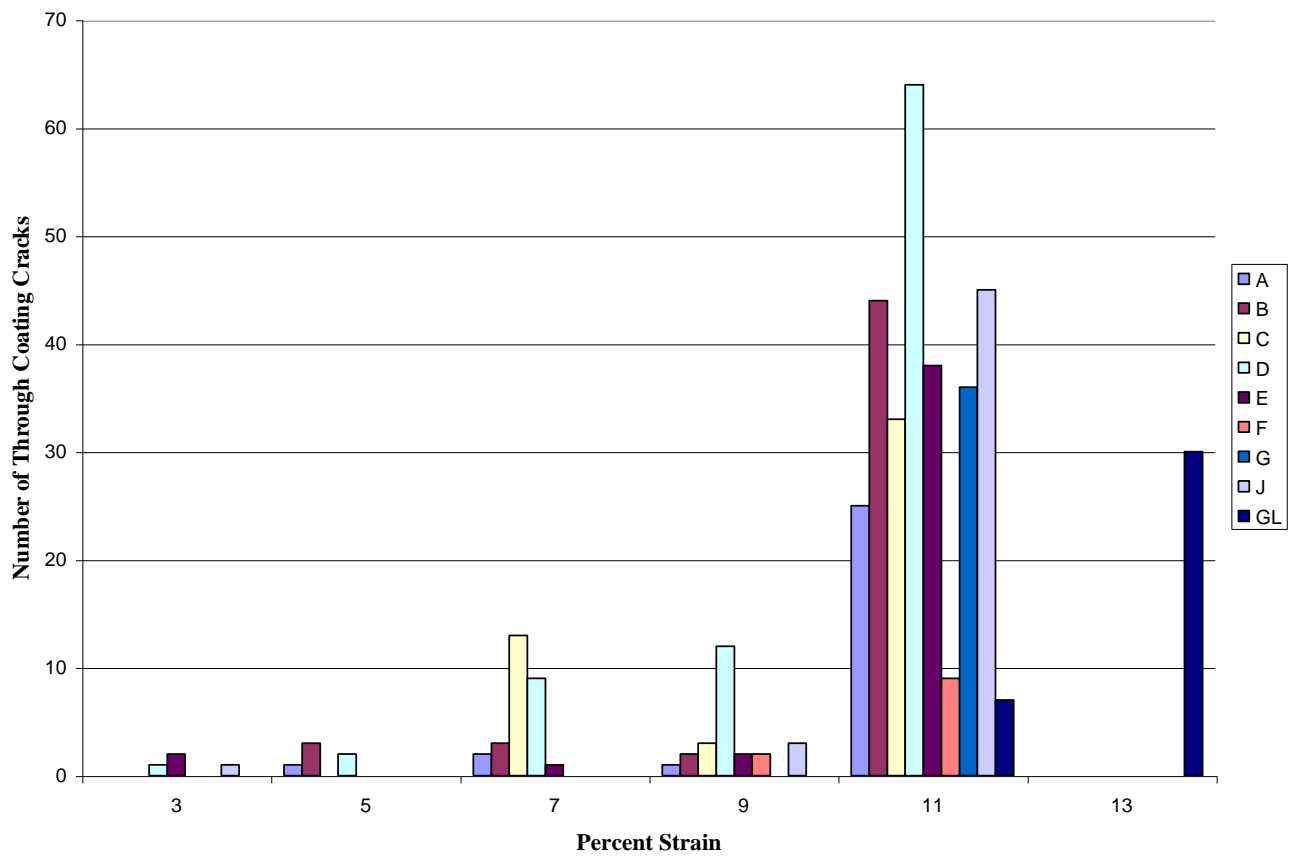
Figure 2.1   Occurrence of through-coating cracks in GALVALUME^{R} samples subjected to tensile strain.
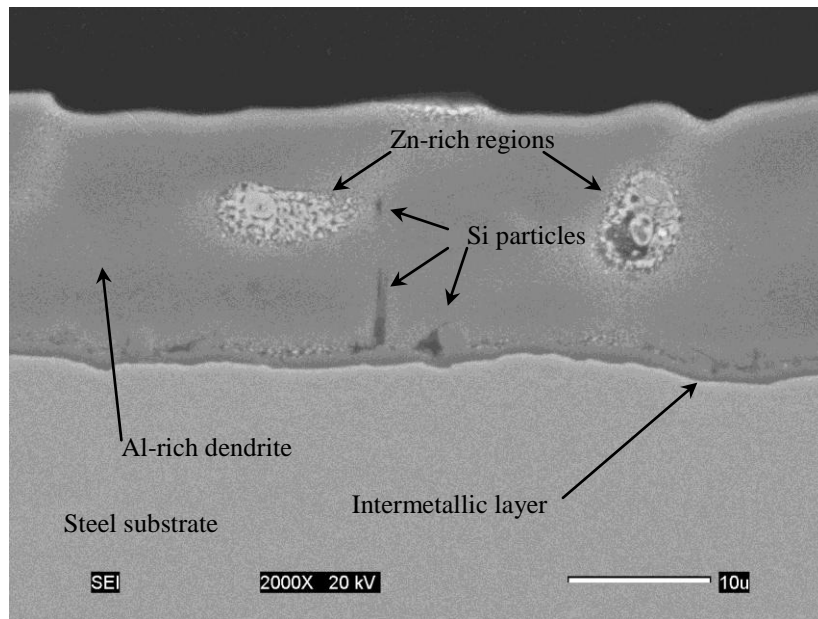
(a)
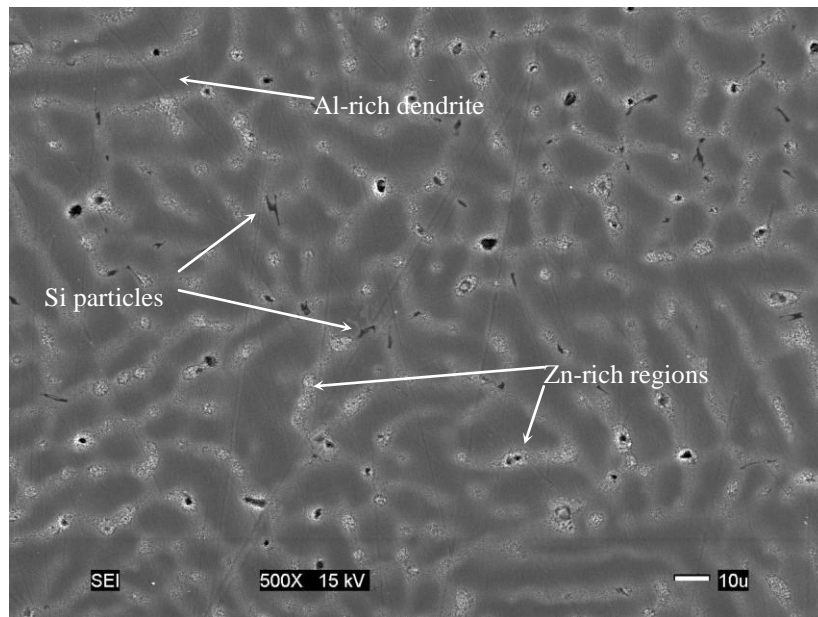
(b)

Figure 2.2   Typical unstrained coating structures, using Mon Valley Works Az55 g50 high-silicon, temper-rolled material as an example: (a) cross-section, (b) surface.

Si

Cracked intermetallic layer

steel substrate

SEI   1500X 15 kV   10u
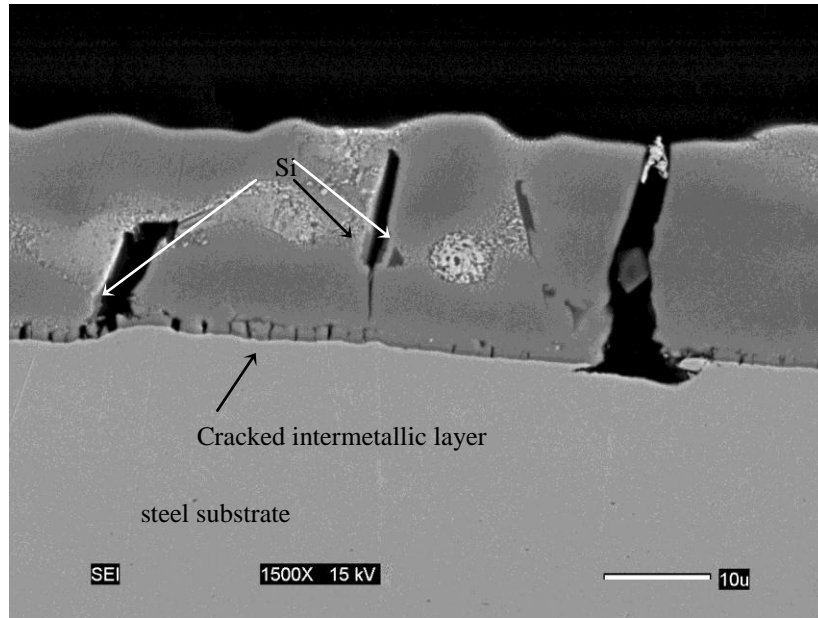
Figure 2.3   Typical features of GALVALUME[R] fracture using Sample J, using Mon Valley Works Az55 g50 high-silicon, temper-rolled material, at 11 percent strain as an example.

Si

SEI   2000X 15 kV   10u
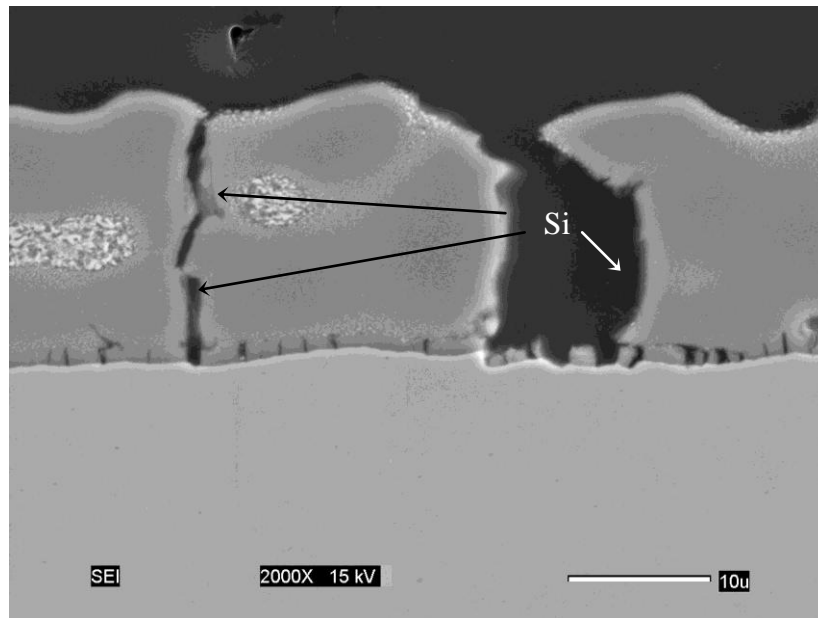
Figure 2.4   Sample J at 11 percent strain. The crack on the right side of the photograph resulted from the brittle fracture of a silicon particle. The angled portion of the crack near the surface of the coating suggests ductile fracture of the coating matrix.

17
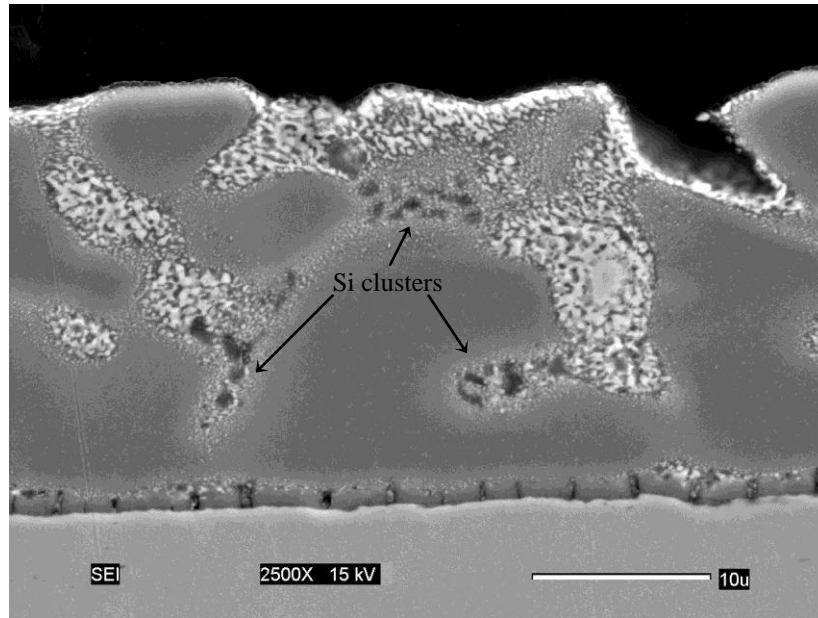
Figure 2.5   Galvalange coating at 11 percent strain.   Strontium and vanadium
             additions result in the formation of clusters of silicon particles in the
             zinc-rich interdendritic material.
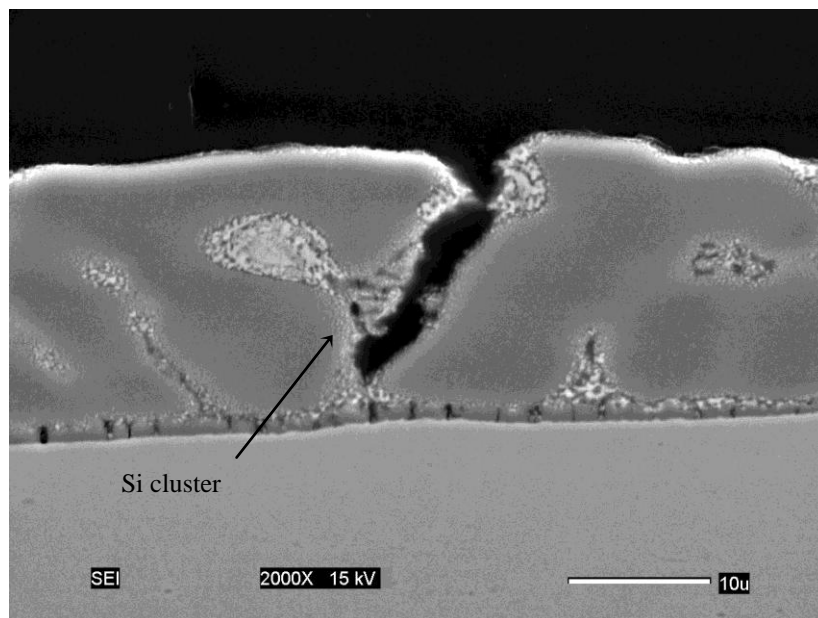
Figure 2.6   Galvalange coating at 11 percent strain with a crack extending along a
             cluster of silicon particles.
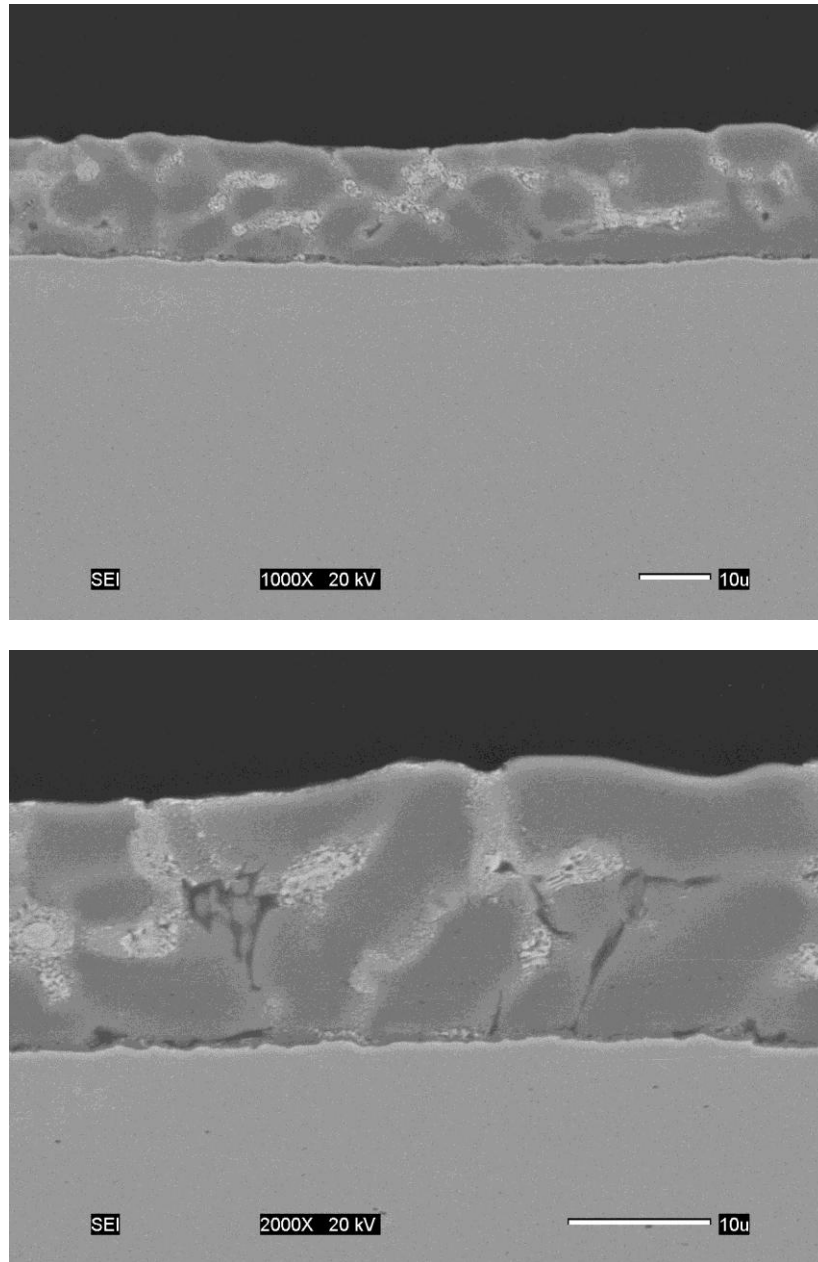
Figure 2.7   Unstrained Sample A at low and high magnification, BHP low-level
strontium addition, temper rolled.
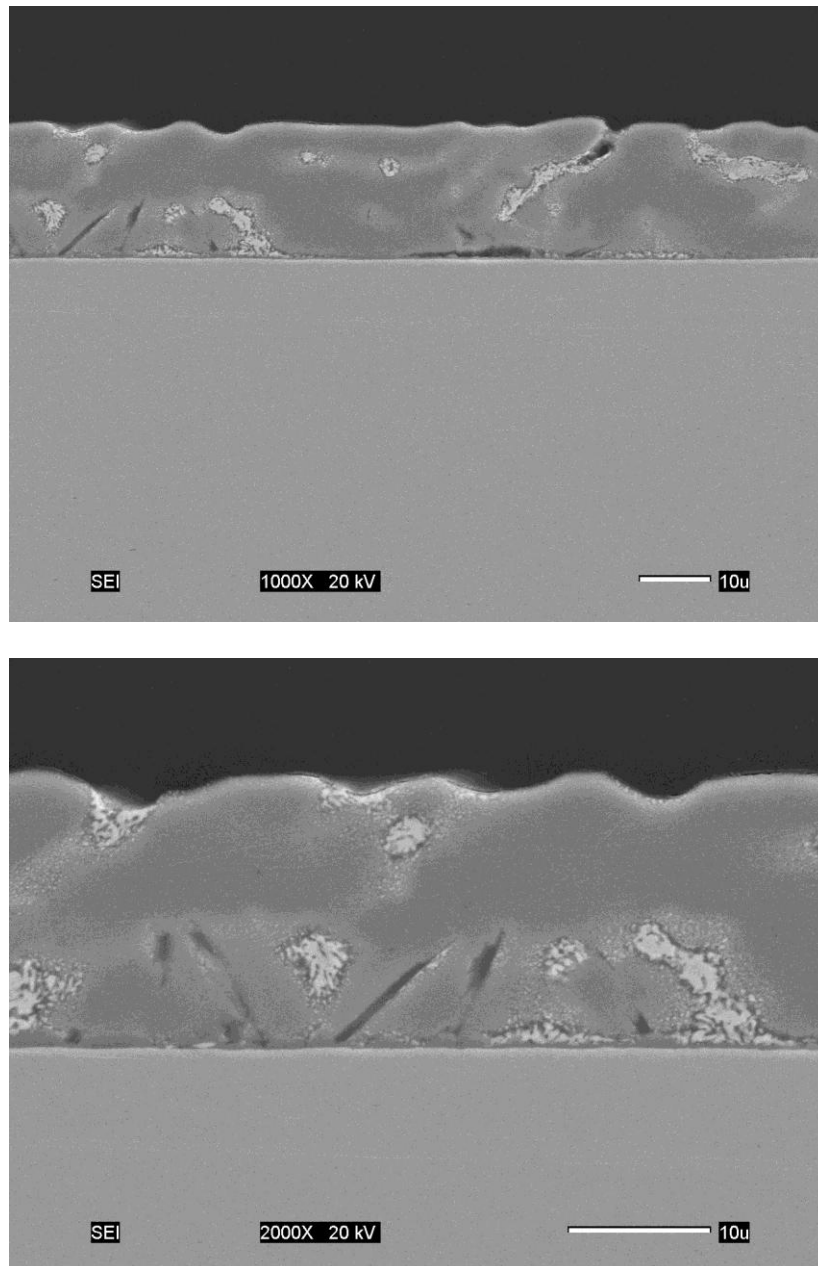
Figure 2.8   Unstrained Sample B at low and high magnification, BHP no strontium.
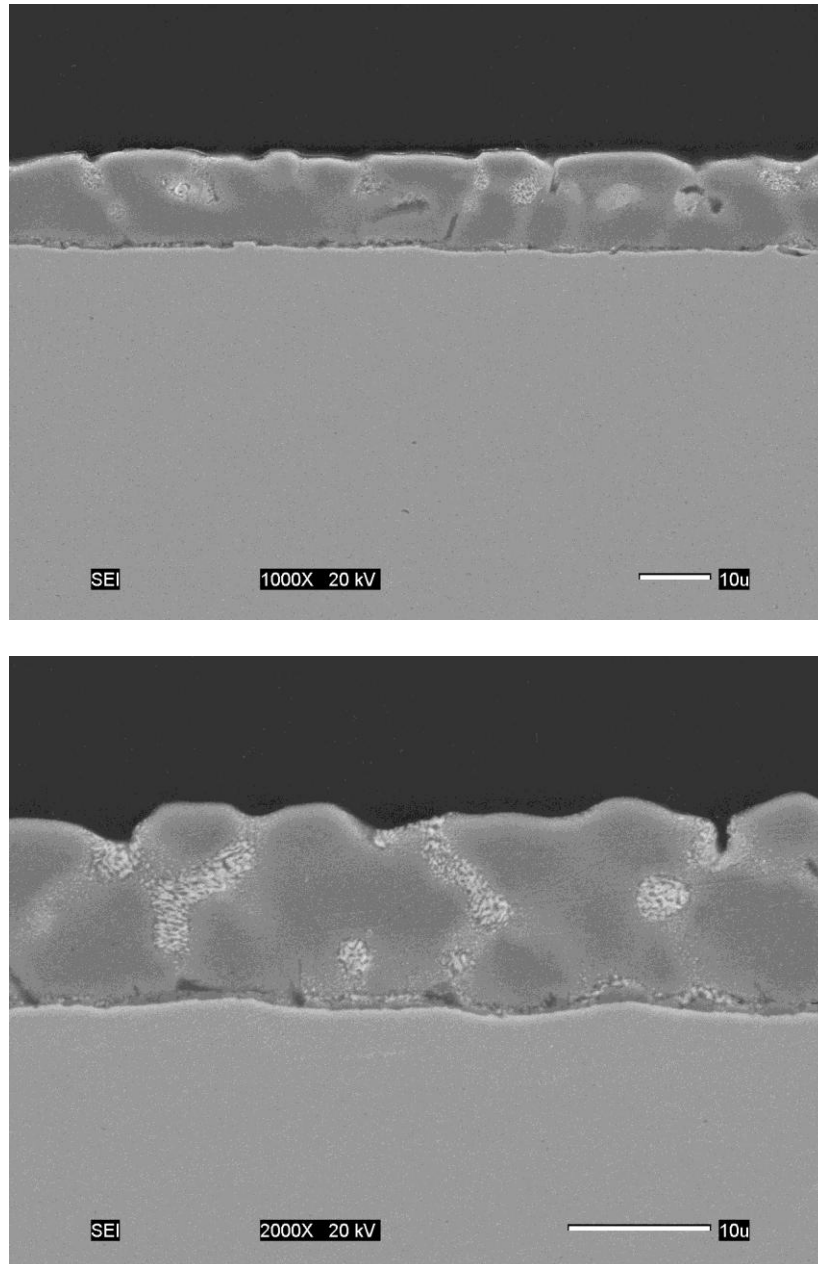
Figure 2.9   Unstrained Sample C at low and high magnification, BHP, low-level strontium addition, temper rolled.
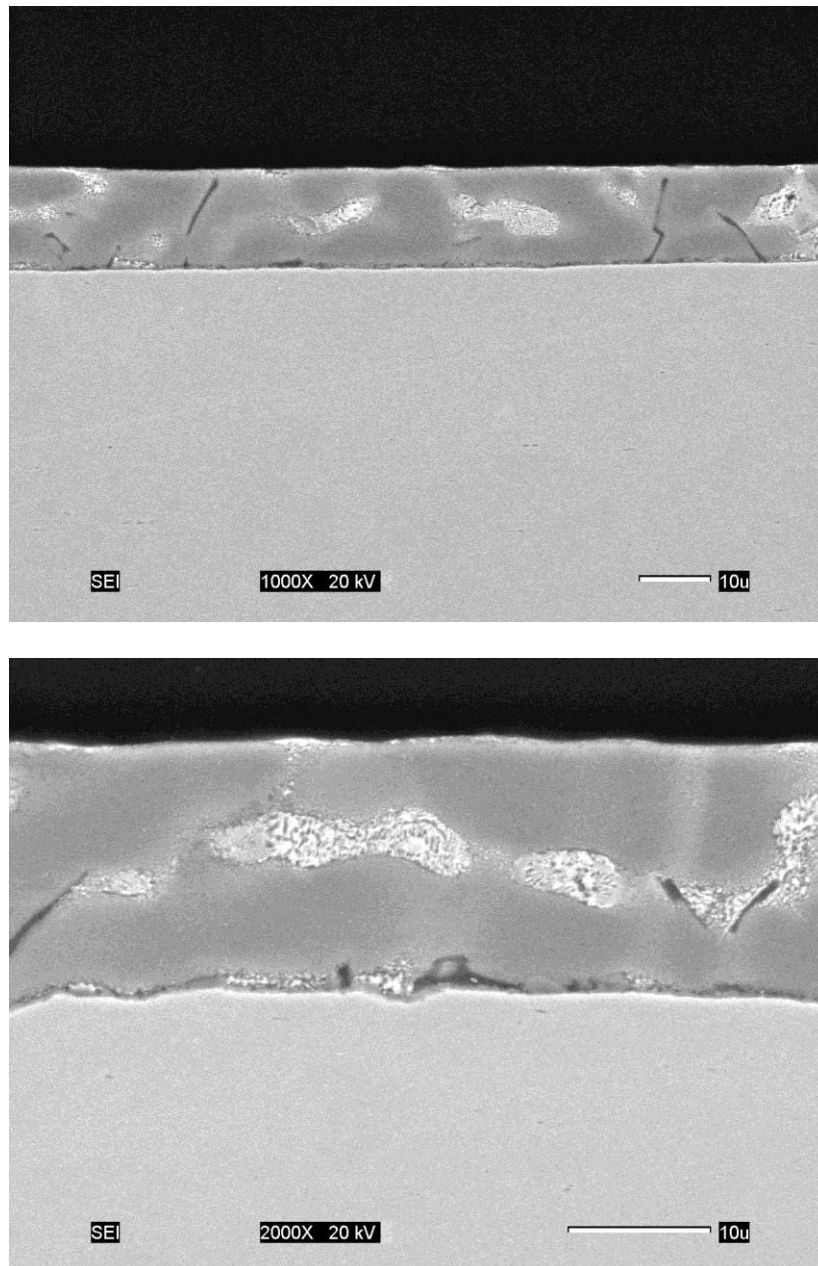
Figure 2.10   Unstrained Sample D at low and high magnification, BHP no strontium.
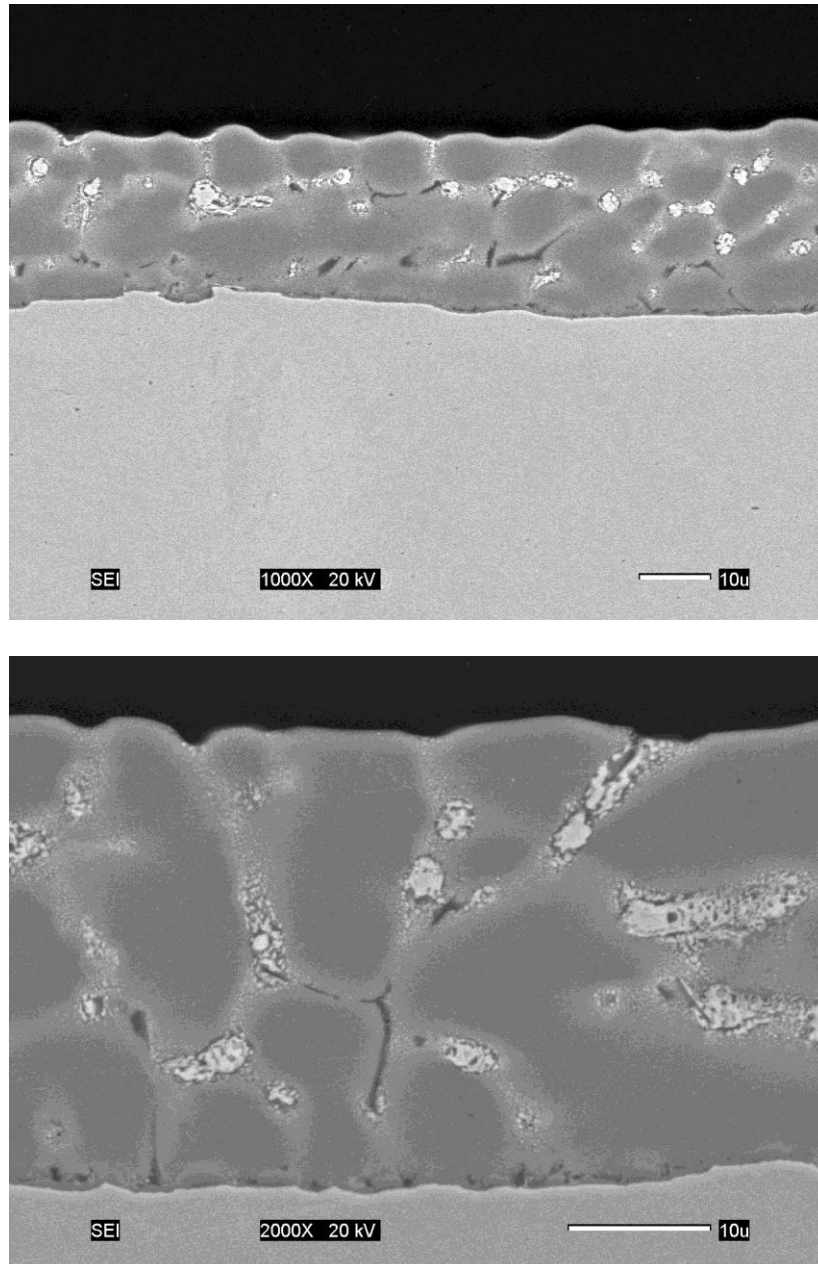
Figure 2.11   Unstrained Sample E at low and high magnification, USS low silicon.
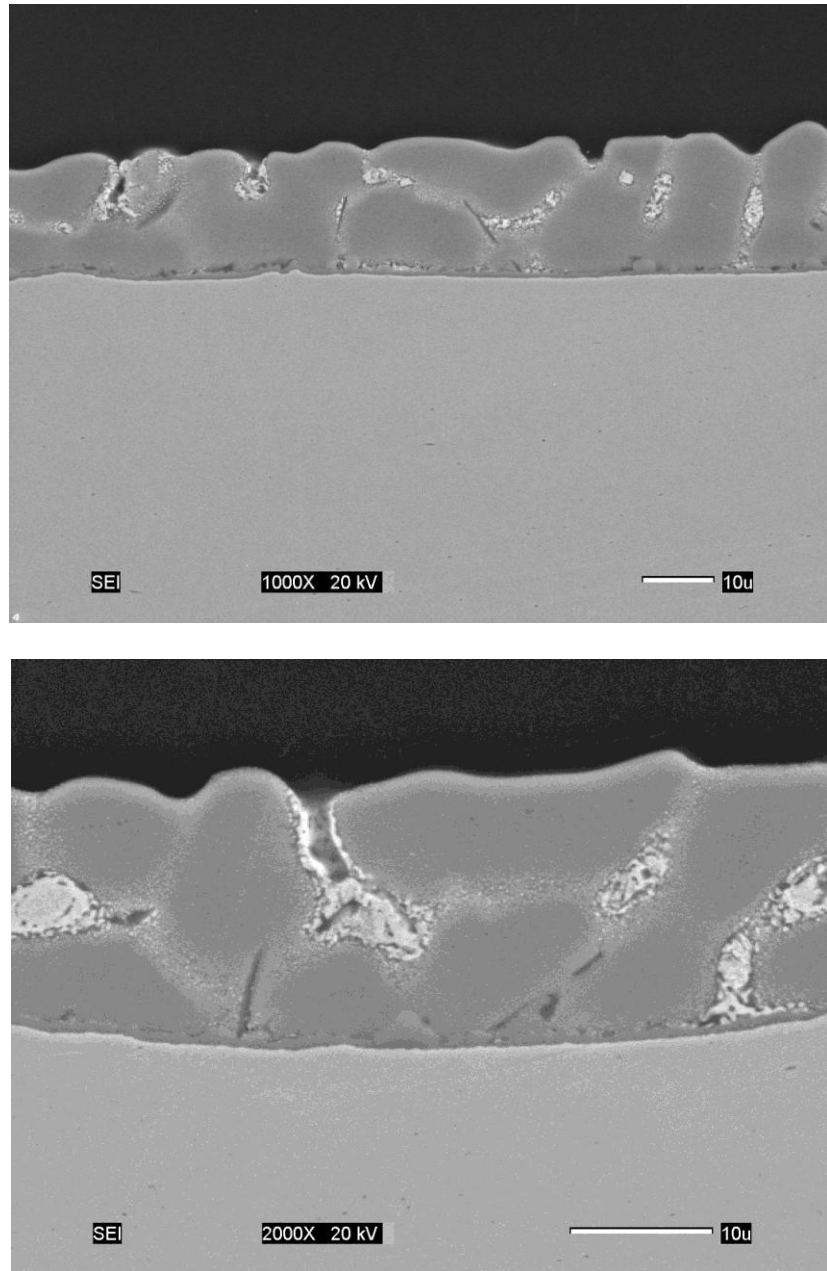
Figure 2.12   Unstrained Sample F at low and high magnification, USS low silicon, temper rolled.
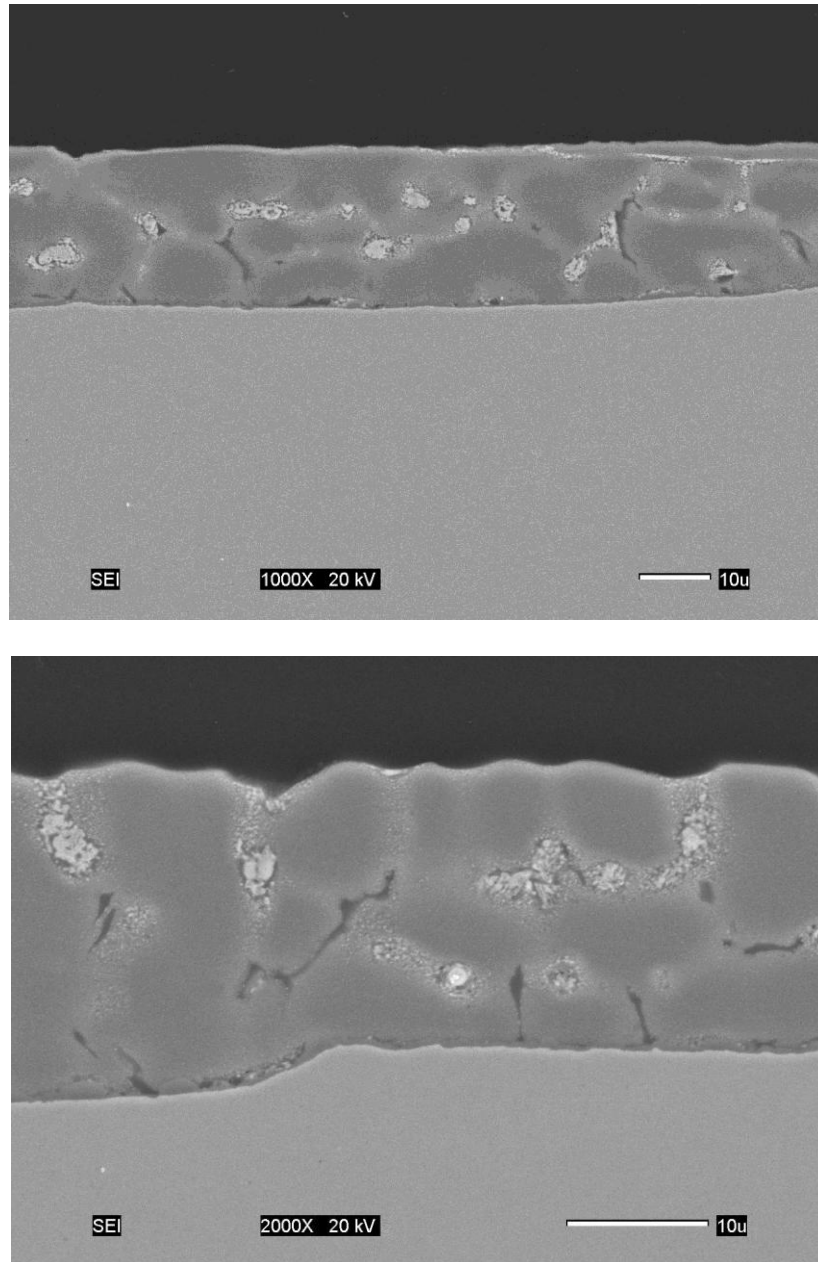
Figure 2.13   Unstrained Sample G at low and high magnification, USS, high silicon.
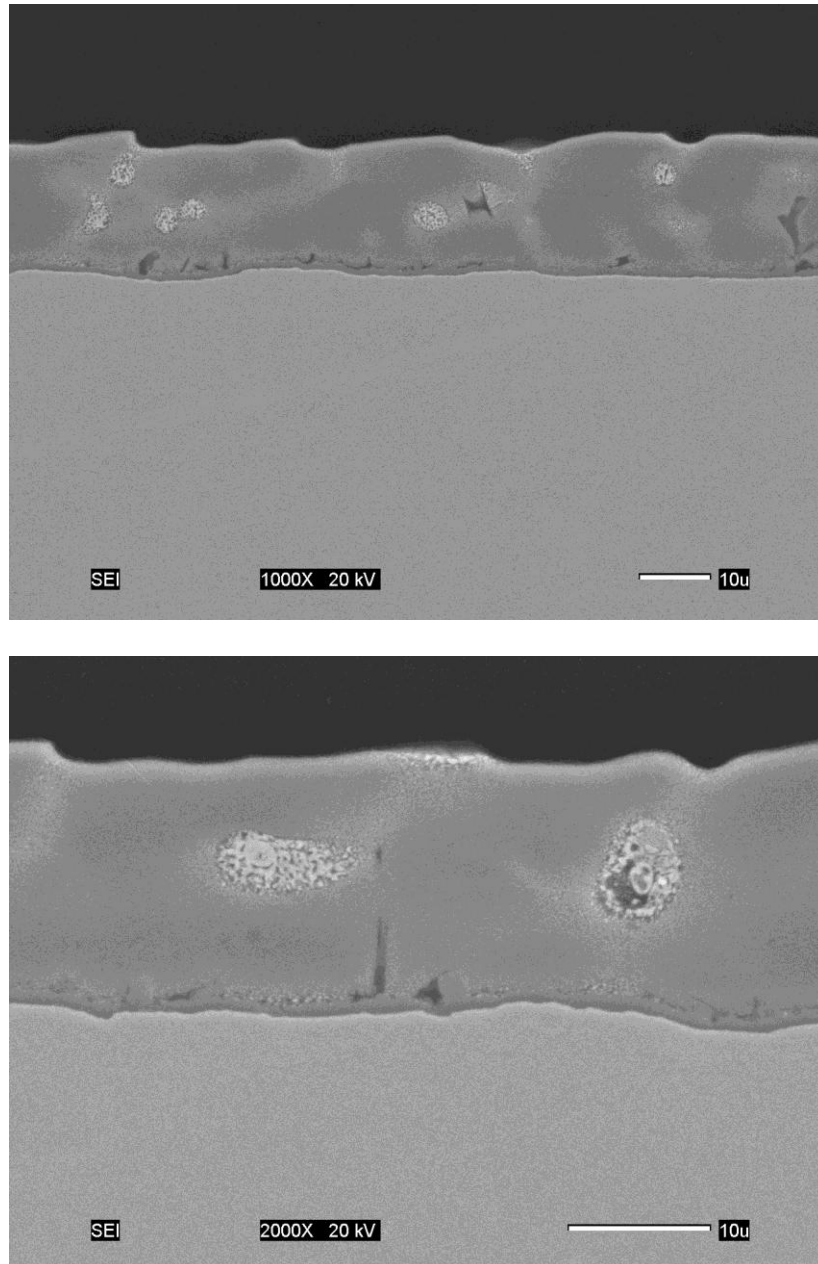
Figure 2.14   Unstrained Sample J at low and high magnification, USS, high silicon, temper rolled.

Chapter 3

Factors Controlling Particle Fracture

3.1 CHAPTER INTRODUCTION

Microstructural observation of GALVALUME^R coating fracture described in Chapter 2 indicated that silicon particle fracture was the primary event leading to the overall fracture of the coating system and the literature review described in Chapter 1 indicated that particle fracture is a primary contributor to failure of a general particulate reinforced composite system. As such, developing an understanding of factors which control particle fracture is important for understanding failure of the composite system and developing insight into potential means for improving the fracture resistance of both the particles and the composite system. Further, the observation that particle shape modifying additions of strontium and vanadium improved GALVALUME^R performance points to particle shape as an important factor. While references in the literature indicated that particle shape affects the resistance of a particle to fracture, no systematic studies describing this effect were found.

In the present chapter the effect of particle shape is evaluated with analytic solutions and finite element analysis. The GALVALUME^R system (silicon particles in an aluminum coating matrix) is used as a starting point for finite element model development. The models developed are then generalized to consider particle fracture for a broad range of mismatch in Young's modulus between the particle and the matrix.

The goal of this study was to investigate the fracture of brittle particles contained within a ductile matrix and to evaluate the effect of the matrix and the influence of

27

particle shape on particle fracture. Figure 3.1 shows a schematic representing the initial problem considered in this study: the fracture of a single particle located at the mid-thickness ($\frac{h}{2}$) of a coating of thickness h on a steel substrate subject to tensile strain, the direction indicated by arrows in the figure. The starting point for the analysis of Chapter 3 is the classical Eshelby Inclusion Problem [31]. In his analysis, Eshelby showed that, for an ellipsoidal inclusion of one material contained in matrix of a homogeneous second material, the stress-strain fields inside the inclusion are uniform. The goal of Chapter 3 was to consider how the Eshelby Problem could be extended to particle fracture and to identify the effects of particle shape and the mismatch in material properties between the particle and the matrix on particle fracture.

A range of ellipsoidal particle shapes, consisting of prolate spheroids and a spherical particle, were chosen to model second phase particles. Prolate spheroids approximate needle-like particles and spheres provide good approximations of equiaxed particles. Although not considered in the present analysis, plate-like inclusions could be considered with oblate spheroids, using the same approach used for spheres and prolate spheroids.

Particle fracture was considered with two analyses. Initially three-dimensional finite element models were used to determine the strain energy released by through-particle fracture of a range of ellipsoidal particles. These models allowed particle fracture to be considered without detailed simulations of crack tip behavior. The total strain energy released by particle fracture was used to consider the effects of particle size, relative to the coating thickness, scaling of particle size, and to confirm the trends in stress intensity factor predicted by analyses of cracks within particles. In the second analysis, detailed

axi-symmetric finite element models were used to calculate stress intensity factors for cracks of various sizes at different locations within particles.

3.2 THREE DIMENSIONAL MODELS OF THE GALVALUME^R COATING SYSTEM

The three-phase coating system was simulated with three-dimensional finite element models, using the commercial code ABAQUS. A typical finite element model, in this case for the determination of particle stress, is shown in Figure 3.2. The model represents one-eighth of the substrate-coating-particle system. Twenty-node bi-quadratic hexahedral elements were used for all simulations. The steel substrate is shown in red and is a cube with x-, y-, and z- dimensions equal to 1-inch, the half-thickness of the substrate in the model. The coating is shown in blue and has a thickness of 0.1-inch. In a real coating system the substrate half-thickness and coating thickness would be on the order of 0.01- and 0.001-inch, respectively, the model dimensions are 100 times larger. The values of the model dimensions were chosen to overcome limitations of the preprocessing software, which could not create sufficiently small elements for a coating thickness of 0.001-inch. The magnitudes of the dimensions are not critical to the analysis. However, the relative proportions among the dimensions are. Therefore, the relationships between model dimensions for particle size, coating thickness and substrate thickness are representative of standard GALVALUME^R material. The finite element models were used to calculate the average energy release rate, $\overline{G}_I$, for through coating fracture; the total strain energy released by fracture of the particle, divided by the crack

29

face area. $\overline{G}_I$ was then scaled, or reduced, by a factor of 100 (because $\overline{G}_I$ scales with crack size) to be representative of an actual coating system.

The substrate, coating matrix and silicon particles were treated as being linear elastic and the particle is considered to be brittle, which is consistent with experimental observations. For the GALVALUME^R simulations, the constitutive properties of the coating matrix were assumed to be equivalent to those of aluminum, with Young's modulus, E_1, being 10 Msi. The substrate was steel with E_2=30 Msi and the particle is silicon with $E_{particle}$=16 Msi. Poisson's ratio was taken to be 0.3 for each of the constituents. Specific values of the constitutive properties of the GALVALUME^R coating matrix are not available. The properties of aluminum were chosen because aluminum is the primary constituent of the coating matrix.

The range of ellipsoidal shapes used to simulate the particles is shown in Figure 3.3. The particle half-length, in the model x-direction, is designated as "b". The half-height, in the model y-direction, is designated as "a". The particle half-depth, in the model z-direction, is designated as "c". The particle shapes range from a needle-like prolate spheroid with the long axis vertical (b = c < a), having an aspect ratio of b/a = 1/8, to a sphere (a = b = c), to a prolate spheroid with the long axis horizontal (a = c < b), with b/a = 8.

Two types of particle simulations were conducted in this study: constant particle height (CPH) and constant particle volume (CPV) simulations. The results of these simulations were compared to assess the effects of the steel substrate below the coating and the free surface at the top of the coating. In the CPH simulations the particle height, 2a, was maintained at one-half of the coating thickness (0.05-inch, model dimension). As

30

the particle aspect ratio increased from b/a = 1/8 to b/a = 1, the narrow elliptical particle cross-section widened to a circular cross-section, as shown in Figure 3.3. From b/a = 1 to b/a = 8, the particle cross-section was a constant circular shape and the particles progressively lengthened in the direction of applied strain and the cross section radius decreased.

In the CPV simulations, which are depicted in Figure 3.4, the particle height was reduced from a value of 2a = 0.05 for b/a = 1/8 to maintain a constant particle volume for each aspect ratio shown. In cases where the particle aspect ratios are reciprocals, for example, b/a = 1/8 and b/a = 8, the particles have the same dimensions but are rotated 90 degrees about the model z-axis. The CPV particle dimensions are shown in Table 3.1.

The calculation of strain energy released via particle fracture, for either the CPH or CPV cases, can be divided into two problems. The first is the solution for the stress build-up in the particle when the coating-substrate system is subject to a uniform far-field displacement, e. g. tensile loading, and the second is the fracture of the particle under the same conditions, as a result of the particle stress build-up. Each problem was solved with a finite element simulation, with the results of the particle stress simulation used as the input to the particle fracture simulation.

3.3 CALCULATION OF PARTICLE STRESS

The first problem considered is the transfer of stress from the coating matrix to an ellipsoidal silicon particle when the substrate-coating-particle system is subject to a uniform far-field displacement. The magnitude of the stress transferred to the silicon particle by the coating matrix depends on the shape of the particle. Particle size, relative

31

to the thickness of the coating can also be important. However, for this study, particle sizes were found to be small in relation to the coating thickness, meaning that particle behavior in the finite thickness coating was equivalent to particle behavior in a continuum.

For the particle stress simulations the model, (as shown in Figure 3.2) was loaded with a prescribed displacement in the x-direction on the face located at x = 1 to give a uniform far field strain of 0.001. Uniform stresses, away from the particle, of 10,000 psi in the coating matrix and 30,000 psi in the substrate resulted. Symmetry boundary conditions were applied on the faces located at x=0, y=0, and z=1. Simulations were performed for particle aspect ratios ranging from b/a = 1/8 to b/a = 8, for both the CPV and CPH cases. Figure 3.5 shows a contour plot for a typical particle stress result, in this case a CPV simulation for b/a = 4. The resulting particle stress is uniform, consistent with the Eshelby Problem.

The CPV and CPH results for particle stress were compared to the Eshelby solutions, for silicon particles in an aluminum continuum with a far field stress of 10,000 psi, in Figure 3.6 and good agreement between the finite element and analytic predictions was obtained. For small and large aspect ratios, the particle stress results approach limiting values given by the Eshelby solution. For the limiting case of b/a = 0, a vertical silicon cylinder oriented normal to the loading direction in an aluminum continuum, the Eshelby solution gives a particle stress of 11,400 psi. For the limiting case of b/a = ∞, a horizontal silicon cylinder oriented parallel to the loading direction, the Eshelby solution gives a particle stress of 16,000 psi.

The agreement between the CPV, CPH, and Eshelby solutions indicates that, for aspect ratios from b/a = 1/8 to 8 and particle heights of up to half of the coating thickness, the particle stress solutions are not being significantly affected by the steel substrate below the coating or the free surface at the top of the coating. The particles can be considered to be small relative to the coating thickness and stress results are equivalent to the case of particles in a continuum comprised of coating material, e. g. the Eshelby Problem.

3.4 SIMULATION OF STRAIN ENERGY RELEASED BY PARTICLE FRACTURE

In fracture mechanics, crack propagation is usually considered with either a stress-based or an energy-based approach. The stress-based approach uses a stress intensity factor, K, to describe the singular stresses at the tip of a sharp crack in terms of far-field stresses. An example of the form of K, from the problem of a crack of length 2a in an infinite plate subject to a far-field stress, σ, is:

$$K_I = \sigma\sqrt{\pi a} \, , \, (\, units = psi\sqrt{inch} \,). \tag{3.1}$$

The subscript, I, refers to mode I or normal loading, as opposed to modes II and III (shear and tearing modes). Brittle crack propagation will occur when K_I reaches a critical value, K_{Ic}, which depends on the material.

Alternately, fracture can be approached from an energetic standpoint. When fracture occurs, free surfaces (crack faces) are created. The creation of the crack faces is accompanied by a reduction of the total energy in the system, which consists of the work done by external loads and the stored strain energy. Because the coating-substrate-

particle system considered in this study is loaded with a prescribed displacement which is subsequently held constant, the external work component of the energy in the system is zero. The energy released by crack formation consists entirely of the change in stored strain energy.

The energy released per unit area of crack formation is defined as the energy release rate, G. The mode I stress intensity factor and energy release rate are related through the following expression:

$$G_I = \frac{K_I^2}{\bar{E}},$$ (3.2)

where:

$$\bar{E} = E \text{ (for plane stress) or } \frac{E}{(1-\nu^2)} \text{ (for plane strain)}$$

and E and ν are Young's Modulus and Poisson's Ratio, respectively.

In the energetic formulation, crack propagation occurs when the energy release rate, G_I, reaches a critical value, G_{Ic}.

The stress intensity and energy release rate terms described above are for the propagation of an existing crack or crack-like flaw and each of these terms depends on the initial length of the crack. The fracture problem considered in this study is cracking entirely through embedded particles. While particle fracture will initiate from flaws within the particle, the nature of these flaws is unknown. The final crack size, which is the particle cross-section, is known. For particle fracture, the total energy released can be determined through the integration of G_I with respect to crack face area from the limiting

case of an infinitesimal initial crack to a crack completely through the particle. For a particle with a circular cross-section this integral is:

$$\text{Strain Energy}_{released} = \int G_I dA = 2\pi \int_0^a G_I r dr \qquad (3.3)$$

where:

a = radius of the particle cross section

A = particle cross section area

Dividing the strain energy released by the final crack area (the particle cross-section area) gives the average energy release rate with the general, integral form:

$$\overline{G_I} = \frac{\int G_I dA}{A}. \qquad (3.4)$$

$\overline{G_I}$ is the average energy release rate for a crack propagating entirely through a particle.

Three-dimensional finite element simulations of uncracked and fully cracked particles were used to determine $\overline{G_I}$ for each particle. To calculate $\overline{G_I}$ it was necessary to determine the amount of strain energy released when a through-particle crack is introduced into a model subject to a uniform far-field displacement. This methodology is illustrated in Figure 3.7. Case 1 shows a schematic of one-half of a continuum containing a second-phase particle. The application of a displacement, δ, to the right edge of the continuum results in surface tractions, σ_1 and σ_2, on the left edge to maintain equilibrium. The left edge of the continuum in Case 1 corresponds to the face $x = 0$ in the finite

element model. The right edge of the continuum corresponds to the face x = 1. The surface traction, σ_1, corresponds to the stress that develops in the coating matrix in a particle stress simulation. The surface traction, σ_2, corresponds to the stress build-up in the particle. For an ellipsoidal particle, σ_2 will be uniform, σ_1, in the vicinity of the particle, will not be uniform.

The introduction of a crack entirely through the particle, Case 2, through the removal of the surface traction, σ_2, over the crack length, 2a, will result in a decrease in the total strain energy stored in the system. The difference in strain energy between Cases 1 and 2 is the strain energy released by the introduction of the crack. Ideally, the strain energy released could be determined by comparing the strain energies resulting from finite element simulations of Cases 1 and 2. However this approach was impractical because the strain energy released was seven orders of magnitude smaller than the total strain energy introduced by the applied displacement. This resulted in inadequate resolution when comparing the results of simulations of Cases 1 and 2.

The simulation of the pressurized crack problem depicted in Case 3 of Figure 3.7 provided an alternate method for determining the strain energy released through particle fracture. The strain energy released by the introduction of a crack is equal to the negative of the strain energy introduced to the continuum by the application of the surface traction, σ_2, to the crack face, Case 3. Finite element simulation of Case 3 overcomes the resolution problem that arises from taking the difference in strain energies between Cases 1 and 2. This is because the strain energy resulting from a finite element simulation of Case 3 is due entirely to particle fracture.

36

The approach used to determine $\overline{G}_I$ for the through-cracking of a silicon particle involved two steps. The first step, corresponding to Case 1, consisted of the determination of the stress, through a finite element simulation, that develops in an uncracked particle when the coating-substrate system is subject to a far-field displacement. The pressurized crack problem of Case 3 represents the second and final step. In a second finite element simulation, the particle stress was applied to the unconstrained face of the particle on the plane x=0 while the rest of that plane (the coating matrix and the substrate) is constrained with symmetry boundary conditions. The total strain energy introduced to the finite element model by the application of the particle stress is equal to the strain energy that would be released by the through-cracking of the particle with the model subject to the far-field displacement loading. Dividing this strain energy by the particle face (crack face) area on the finite element plane x=0 gave the average strain energy release rate, $\overline{G}_I$, for through-cracking of the particle.

3.4.1 Model Verification

To ensure the accuracy of the finite element models it was necessary to compare model predictions to known solutions. Analytic solutions for particle fracture are not available. Results for internal cracks in homogenous media are. Before the fracture modeling approach was applied to the substrate-coating-particle system it was tested against the analytic solution for circular or penny-shaped crack in a homogeneous continuum[32]. This solution gives expressions for crack opening displacement and stress intensity factor. The finite element mesh used for the simulation of a penny-shaped crack in a continuum was similar to that shown in Figure 3.2 except that another region

of material, equal in size to the material representing the substrate in the figure, was added above the region that represents the coating. A circular, or penny-shaped, crack of diameter 2a =0.010-inch (model dimension) was located at the coating mid-thickness at the intersection of the model planes x=0 and z=0. Constitutive properties of aluminum were used for all regions of the model, converting the three-phase mesh to a homogenous system. An applied far-field strain of 0.001 results in a uniform stress of 10,000 psi, for the homogenous aluminum system. This stress was applied to the crack face in the finite element model, utilizing the methodology outlined in Figure 3.7, and the results for crack opening displacement and $\overline{G}_I$ were compared to values predicted by the published solution.

The solution for the mode I stress intensity factor for a penny-shaped crack[32] is:

$$K_I = \frac{2}{\pi} \sigma \sqrt{\pi a} \quad (\text{units} = psi\sqrt{inch}) \tag{3.5}$$

where: σ = the applied far-field stress,

a =the radius of the crack,

From K_I, the strain energy release rate for plane strain, G_I, can be determined:

$$G_I = K_I^2 \frac{(1-v^2)}{E} = \frac{4}{\pi} \sigma^2 a \frac{(1-v^2)}{E} \quad (\text{units} = \frac{lb \cdot in}{in^2} = \frac{lb}{in}) \tag{3.6}$$

G_I is the amount of strain energy released per unit area of crack formation. From G_I, the average energy release rate, $\overline{G}_I$, can be determined by integrating G_I over the crack face area, A, and dividing by A:

38

$$\overline{G_I} = \frac{\int G_I dA}{A} = \frac{8}{3\pi} \frac{(1-v^2)}{E} \sigma^2 a \qquad (3.7)$$

for the verification case with:

$a = 5x10^{-5}$ inch

$\sigma = 10{,}000$ psi

E=10 Msi

$v = 0.3$

$$\overline{G_I} = 3.86x10^{-4} \frac{lb}{in}$$

A detail of the finite element mesh, showing stress contours on the deformed mesh, used to simulate the penny-shaped crack problem is shown in Figure 3.8. Through experimentation with element size in the vicinity of the crack, the element length in the radial direction for elements near the crack tip was found to be the most significant element size parameter for model accuracy. For a radial element length, at the crack tip, of $a/_{50} = 0.0001$-inch (model dimension) the model predicted a strain energy addition of $2.994x10^{-6} lb \cdot in$ to the system. Dividing this result by the crack face area $A = 7.854x10^{-5} in^2$ and scaling by a factor of $1/_{100}$ gives $\overline{G_I} = 3.81x10^{-4} lb/_{in}$, which is in good agreement, to within 1.3 percent, of the value predicted by the published solution.

A second accuracy check can be obtained by comparing the finite element prediction for crack opening displacement to the published solution. The solution for the crack opening displacements[32] is given by:

39

$$\upsilon(r) = \frac{4\sigma}{\pi} \frac{(1-v^2)}{E} \sqrt{a^2 - r^2} \; , \tag{3.8}$$

where: σ = the applied far-field stress,

a =the radius of the crack,

r =radial distance from the center of the crack

$\upsilon(r)$ =crack opening displacement as a function of r

The finite element and analytic predictions of crack opening displacement for the penny-shaped crack problem are shown, in terms of model dimensions, in Figure 3.9. The data points in the plot correspond to nodal positions in the finite element model. With the exception of the two nodes closest to the crack tip, which are from the element adjacent to the crack tip, the finite element results agree very well with the analytic predictions. The finite element predictions of the displacement of the first two nodes at the crack tip are significantly less than the analytic solution because, even with very small elements, the finite element model is unable to capture the near-tip behavior. However, because the model can accurately predict the behavior outside of the near-tip region the model is able to give accurate predictions of $\overline{G}_I$. The area under the displacement plot of Figure 3.9 represents the work imparted to the finite element model by the stress applied to the crack face. This work is equal to the strain energy imparted to the model.

Finite element model accuracy is dependent on element size. Small elements are necessary to accurately capture sharp gradients in displacement, such as those that occur at a crack tip. The element length normal to the crack front was found to the controlling

parameter for model accuracy. A local element length at the crack tip of 0.0001-inch

(model dimension) was used for all the finite element models of this study. The model

crack size of diameter a=0.01-inch, equal to $\frac{1}{10}$ of the coating thickness, was chosen for

the verification case (the penny-shaped crack problem) because it is at the smaller end of

the range of particle sizes used in the study. For larger particles, and larger crack sizes,

the local element length of 0.0001-inch will be a smaller percentage of the overall crack

size, resulting in an increase in accuracy as particle size increases. In one case, a model

particle height smaller than 0.01-inch was used, in a CPV simulation with an aspect ratio

of $\frac{b}{a}$ = 8. In this case the model particle half-height was 2a=0.00625-inch. A local

element length of 0.0001-inch at the crack tip was used for this case as well.

3.5 EVALUATION OF STRAIN ENERGY RELEASE SIMULATONS

The results of the three-dimensional simulations of strain energy released by through-

particle fracture are shown in Figures 3.10 to 3.12. The results are shown in terms of

average energy release rate that is normalized with respect to a penny-shaped crack in

aluminum, the matrix material, having a height, 2a, equal to the largest crack considered

in the study, a crack of height equal to half the model coating thickness. Figure 3.10

shows the results for the constant particle height simulations. The normalized average

energy release rate, $\overline{G}_{In}$, increases sharply as aspect ratio increases from 1/8 to 1. This

occurs because the narrow elliptical crack face widens with increasing aspect ratio,

reducing constraint on crack opening. As the aspect ratio increases from 1 to 8, the crack

41

face shape remains circular, and constant, and the only change in $\overline{G}_{In}$ is due to increasing particle stress from the lengthening of the particles in the loading direction.

The results for the CPV simulations are shown in Figure 3.11. In this case, as aspect ratio increases, the particle heights reduce to maintain constant particle volume. As a result, the maximum value of $\overline{G}_{In}$ occurs for a spherical particle. Minimum, and approximately equal, values occur for aspect ratios of 1 and 8, long, thin prolate spheroids.

The effect of the substrate on the bottom surface of the coating and the free surface at the top of the coating can be evaluated by considering the scaling ratio between the CPH and CPV results, because $\overline{G}_{In}$ scales with crack height. This scaling ratio is shown, along with the ratio in crack height between the CPH and CPV cases in Figure 3.12. The results show close agreement between the $\overline{G}_{In}$ ratio and crack height, which is equivalent to particle height, at all aspect ratios. This indicates that, for particle heights up to one half the coating thickness, the particle fracture problem is essentially unaffected by the substrate and coating free surface and that continuum conditions can be considered to apply for the matrix. This means that the strain energy release results presented are representative of second phase particles in a homogeneous continuum, as well as for the particular coating system modeled.

These results indicated that the range of ellipsoidal shapes considered for the coating problem could be modeled as particles in a continuum, a more general problem with broader applications beyond the initial coating problem considered.

3.6 SIMULATION OF CRACKS WITHIN PARTICLES

After the three-dimensional finite element simulations of strain energy released by particle fracture were completed, a detailed analysis of cracks within particles was conducted. This analysis used the Eshelby Problem as a starting point and considered this problem as a fracture problem: the fracture of constant stress ellipsoidal particles with flaws present in the particle cross sections. The Eshelby Equations were used to calculate particle stress for aspect ratios ranging from 1/8 to 8 and for ratios of the Young's modulus of the particle (Ep) to the that of the matrix Em ranging from Ep/Em = 0.1 to 10. These values are shown in Figure 3.13. When Ep/Em is less than one the maximum stress occurs for an aspect ratio of 1/8. When Ep/Em is greater than one the maximum stress occurs for aspect ratio of 8. For particle aspect ratios greater than 1, increasing Young's modulus ratio has a progressively stronger effect on particle stress as aspect ratio increases.

The fracture analysis was conducted with a combination of analytic solutions and two-dimensional, axi-symmetric finite element models. The use of axisymmetric models allowed the use of very detailed crack tip meshes, resulting in a high degree of accuracy for the prediction of stress intensity factors for cracks within particles. Cracks within particles having elliptical cross sections, aspect ratios less than 1, could not be simulated axisymmetric models. Complex three-dimensional models would be required and were not attempted due to meshing limitations and reduced potential for accuracy.

The simulation of cracks within constant volume particles with circular cross sections, particles with aspect ratios of 1, 2, 4, and 8, was conducted and used to illustrate the behavior of cracks at various locations within particles. Knowledge gained from

these analyses was then used to discuss the behavior expected for particles with elliptical cross sections.

An example of an axi-symmetric model used is shown in Figure 3.14. The models contained detailed crack tip meshes for the prediction of stress intensity factors at six locations within and six locations beyond the location of the particle matrix interface. Crack tip locations beyond the interface were included because the same models were used to predict the behavior of cracks extending into the matrix in the analysis of Chapter 4. The locations of the crack tip meshes were chosen to capture the behavior of cracks near the interface. These locations are shown in Figure 3.14. A typical fine mesh used at crack tip location is shown in Figure 3.15. Local element sizes at these locations were a/3125 or smaller, for all the simulations conduced.

Before the particle simulations were conducted, the accuracy of the finite element mesh was tested by simulating a homogeneous case, by setting the constitutive properties of the particle equal to those of the matrix, consisting of penny shaped cracks in an aluminum matrix. A comparison between finite element predictions and the analytic solution is shown in Figure 3.17 for a model of a particle with an aspect ratio of b/a = 8. Good agreement between the finite element predictions and analytic solutions was obtained. Similar agreement was obtained for models of particles with aspect ratios of 1, 2, and 4. The agreement between the finite element models and analytic solutions indicates that dimensions of the axi-symmetric models were large enough for the models to predict behavior of second phase particles in a continuum.

Two crack geometries were chosen to represent flaws within particles: penny shaped cracks and ring shaped cracks. Penny shaped cracks were used to model cracks located at

44

the centers of the particle cross sections. Ring shaped cracks were used to model cracks located near the particle/matrix interfaces. Solutions available for both crack geometries allowed for verification of finite element model accuracy.

3.6.1 Penny Shaped Cracks within Particles

When the cracks with particles are small, the stress intensity factor will be unaffected by the particle/matrix interface and will be given by the continuum solution for a penny shaped crack in the second phase particle material with the Eshelby Stress applied. For larger cracks the stress intensity factor will be affected by the particle matrix interface. The transition from the continuum to near-interface behavior was not known. To understand this transition, plots combining the continuum solution with near interface finite element calculations of stress intensity factor were constructed. The penny shaped crack continuum solution with the Eshelby Stress applied was plotted from a radius of r = 0 to r = 2a/3, where a is the radius of the particle cross section. Finite element calculations for stress intensity factor were plotted from r = 2a/3 toward the interface with the last point located at r = 59a/60.

Stress intensity factors for penny shaped cracks, located at the centers of the particle cross sections, are shown in Figure 3.18 for constant volume silicon particles in an aluminum matrix, the model GALVALUME^R system. As the crack fronts approach the particle/matrix interface the plots of the finite element predictions of stress intensity factor increase in slope and trend toward infinity. At two-thirds of the particle cross section, the plots of the analytic solutions and finite element predictions have similar slopes, but the finite element predictions are offset above the analytic solutions, because

45

the particle/matrix interface increases stress intensity factor beyond the values calculated for the homogeneous case.

To ensure the curves of Figure 3.18 were correctly representing the behavior of cracks within particles, the results were compared to the three-dimensional finite element predictions of strain energy released by through particle fracture conducted for Sections 3.2 though 3.5. The results of Figure 3.18 are shown, converted to strain energy release rates, in Figure 3.19. These curves were integrated numerically, using trapezoidal integration, to give estimates of strain energy released by cracks propagating through the particles. These values were compared to the three-dimensional finite element predictions of strain energy released by cracking entirely through the particles. The results of the two cases agreed to within 0.6 percent for aspect ratios of 1, 2, 4, and 8, indicating that curves obtained by combining analytic and finite element predictions of stress intensity factors accurately represent the behavior of cracks within the particles.

Plots were next constructed, again for penny shaped cracks located at the centers of the particle cross sections, for particle aspect ratios of 1, 2, 4, and 8, for ratios of particle Young's modulus (Ep) to matrix Young's modulus (Em) of Ep/Em =0.1, 0.5, 1.6, 3, 6, and 10. These plots are shown in Figures 3.20 to 3.25. The results in the plots are normalized with respect to a penny shaped crack in an aluminum continuum having the same radius as the constant volume spherical particle in the study.

Comparison of the plots leads to a number of important conclusions. The first observation is that stress intensity factors for cracks nearing the particle/matrix interface trend toward zero when the particle is more compliant than the matrix and to infinity when the particle is stiffer than the matrix. This behavior was expected and is consistent

46

with that shown by Beuth [33] for a crack in a coating approaching the interface with a substrate having different material properties.

In each case shown there is an offset between the results at the location $r = 2a/3$ where the plots switch from the homogenous penny shaped crack solution to the finite element solution for crack fronts near the bi-material interface. In every case the offset is greatest for the spherical particle and reduces as aspect ratio increases from 1 to 8. This behavior is shown in Figure 3.26, in which the relative differences between the analytic solutions for penny shaped cracks in a continuum of the second phase particle material and finite element predictions for penny shaped cracks within second phase particles with crack fronts at $r = 2a/3$ are plotted. This plot shows that the effect of the particle/matrix interface on stress intensity factor extends furthest into the spherical particle. The effect reduces progressively as aspect ratio increases from 1 to 8 and the particles lengthen in the loading direction. The implication is that cracks of similar relative size are less affected by the particle/matrix interface in particles that are longer in the direction of loading. The effect of the matrix on stress intensity factor begins to occur for smaller crack sizes in spherical particles than for longer particles.

The deviations of the stress intensity factors from the analytic, penny shaped crack solutions shown in Figures 3.20 to 3.25 result from the cracks becoming affected by the particle/matrix interface as crack size is increased. When the cracks are small enough, this effect is small, and cracks within particles behave as though they were cracks in a continuum having the same properties as the particle. As the cracks increase in size, they become affected by the matrix. When the matrix is stiffer than the particle, crack opening displacements are reduced in comparison to the homogenous, continuum

47

solutions. When the particles are stiffer than the matrix, the effect of the more compliant matrix is to allow greater crack opening, compared to the continuum solution, resulting in increased stress intensity factors. As cracks near the interface, the effect becomes progressively more pronounced, with stress intensity factors trending either toward zero or infinity, depending on whether the matrix is stiffer or more compliant than the particle.

As shown in Figures 3.20 to 3.25, the finite element curves for stress intensity factor approaching the interface show an affect of particle shape. A review of literature for cracks approaching bi-material interfaces was conducted [33-36]. With the exception of Erdogan and Gupta [36] which considered long axial cracks in two-dimensional circular inclusions (i.e. long circular fibers), the work reviewed dealt with linear interfaces. No research dealing with cracks approaching three-dimensional bi-material interfaces was found.

The effect of particle shape on stress intensity factors approaching the particle/matrix interfaces was further investigated by considering particles with different shapes loaded such that the stress in each particle was the same. This was done for the spherical particle and for the prolate spheroid particle with an aspect ratio of b/a = 8. For the prolate spheroid particle, the Eshelby Solution was used to calculate the reduced far field displacement required for the particle (Eshelby) stress to be equal to that of the spherical particle. This was done for two cases: Ep/Em = 1.6 and Ep/Em = 10. Plots of stress intensity factor for these cases are shown in Figures 3.27 and 3.28. As shown in the figures, when the prolate spheroid particle stress is equal to the spherical particle stress, the portions of the plots constructed from the homogenous continuum solutions match for each particle. However, the offset between the continuum solutions and finite element

solutions at r = 2a/3 (shown on the figures in terms of relative difference) are different for the two particles with the relative difference being significantly higher for the spherical particle.

The two problems, particles with aspect ratios of 1 and 8 with penny shaped cracks to r = 2a/3 and with remote loading resulting in identical Eshelby Stresses, can be recast as pressurized crack problems with the Eshelby Stress applied to the respective crack faces. The equivalence of the remote displacement loading and pressurized crack face loading was verified with finite element simulations for b/a = 8.

With the two particles recast as pressurized crack problems with identical applied stress, the offsets between the continuum penny shaped crack solutions and finite element calculations for stress intensity factor at r = 2a/3 remain the same. Although the particle sizes are different, as shown in Section 3.5, the particle heights can also be scaled to match and the relative differences between the continuum and finite element solutions will remain the same for each case. The differing behavior in stress intensity factor is analogous to differing behavior in crack opening displacement, with the spherical particle exhibiting greater crack opening than the b/a = 8 particle. For the two particles, the fracture problems and applied loadings are now the same, so the difference in crack opening, and thus fracture behavior, can only come from differing resistance to crack opening. This can only come from differences in stiffness resulting from the differing lengths of the particles, which is the only remaining difference between the two cases.

The stress intensity factors that result when the prolate spheroid particles are loaded with the same far field applied displacement as the spherical particles, resulting in higher particle stresses for the prolate spheroids, are also shown on the figures. The offset

49

between the continuum and finite element solutions for the prolate spheroid particles is the same for both prolate spheroid particle stress levels shown, meaning that the effect of shape is independent of loading.

Changing particle shape changes the effect of the particle/matrix interface on stress intensity factor for cracks large enough, or close enough, to be affected by the interface. For particles that are shorter in the direction of applied loading, the effect of the interface on stress intensity factor extends further into the particles. As particles lengthen in the loading direction, this affect decreases, meaning that cracks can be larger in proportion to the particle cross section before they become affected by the interface.

3.6.2 Ring Shaped Cracks near the Particle/Matrix Interface

To further investigate the behavior of cracks within second phase particles, cracks located near the particle/matrix interface were considered. A ring shaped crack was chosen as the basis for this analysis. This was done because finite element simulation of ring shaped cracks near the interface could be conducted with the same finite element models used for the simulation of penny shaped cracks in particles and because the solution to this crack geometry is available for comparison[32].

Finite element meshes for ring shaped cracks in particles having aspect ratios of 1 and 8 are shown in Figures 29 through 32. For each particle, two crack lengths were considered, $a/120$ and $11a/120$, where a was the radius of the particle cross section for each of the respective particles. For each crack, the outer crack front was located $a/60$ from the particle/matrix interface. In each case, stress intensity factors were calculated for ratios of the Young's modulus of the particle (E_p) to the Young's modulus of the

50

matrix (Em) of Ep/Em = 0.1, 0.5, 1.6, 3, 6 and 10, the same ratios used for the penny shaped crack simulations.

Results of the ring shaped crack simulations are shown in Figure 3.33 for b/a = 1 and Figure 3.34 for b/a = 8. The results are shown in terms of the relative difference between stress intensity factors predicted by finite element simulations for ring shaped cracks in second phase particles in an aluminum matrix and stress intensity factors calculated from the handbook solution for ring shaped cracks in a continuum having the same properties as the particle. Thus, the figures show the percent change in stress intensity factor due to the particle/matrix interface.

The results are plotted in Figure 3.33 and 3.34 and include and accuracy check of the finite element models. In each plot, the curves meet at an Ep/Em value of 1 (the homogeneous case) with relative differences between the finite element predictions and homogenous handbook solutions near zero, meaning that the finite element simulations of the homogenous case matched the handbook solution. For the cases shown in Figures 3.33 and 3.34 the maximum deviation between the finite element predictions and handbook solutions for the homogenous case was 0.2 percent.

The curves plotted in Figures 3.33 and 3.34 show that the smaller (a/120) ring shaped cracks were essentially unaffected by the matrix and the stress intensity factors for cracks in second phase particles matched the homogeneous solution to within less than two percent for identical cracks in a continuum of the second phase material. In contrast, the large ring shaped cracks were significantly affected by the matrix. As the Young's modulus ratio (Ep/Em) increased, or decreased, from 1, the difference between the finite element predictions for ring shaped cracks in second phase particles and the homogenous

solutions increased. For both particle shapes, the effect of the interface on stress intensity factor was much greater for the outer crack front, which was closer to the interface.

Comparing Figures 3.33 and 3.34 with 3.26 shows that a similar, but larger, relative difference resulted for the outer crack front of the larger ring shaped crack (crack length equal to 11a/120) in a spherical particle than for a penny shaped crack of radius 2a/3 even though the ring shaped crack was significantly smaller. For the 11a/120 ring shaped crack in the b/a = 8 particle, relative differences to the homogenous solution in Figure 3.34 were similar in magnitude but less than those of the spherical particle in Figure 3.33. These results show that the effect of the particle/matrix interface on stress intensity factor is greater for cracks closer to the interface and that this effect is greater for a spherical particle than for longer prolate spheroid particles aligned with the loading direction.

Unlike the spherical particle (b/a = 1) the relative differences for the outer crack front of the 11a/120 ring shaped crack in the b/a = 8 particle were significantly larger than those predicted for penny shaped cracks in this particle shape shown in Figure 3.26. This is consistent with the observation from the penny shaped crack analysis that the effect of the interface extends further into particles with lower aspect ratios.

Figures 3.33 and 3.34 also show that, consistent with Figures 3.20 to 3.25, when cracks are small enough, they are not affected by the interface and stress intensity factors can be obtained from homogenous solutions using the Eshelby particle stresses. However, for cracks to be unaffected by the interface, they must be smaller in size when closer to the interface.

Additional simulations were conducted to further examine the effect of crack proximity to the interface. This was done for ring shaped cracks in a b/a = 8 prolate

spheroid particle having lengths of a/60. Two cases were considered: a crack with the outer crack front at a distance a/60 from the particle/interface and a crack with the outer crack front touching the interface. Finite element meshes for these cases are shown in Figure 3.35. Stress intensity factors are shown for the inner crack fronts in Figure 3.36. The figure shows significant increases in the effect of the interface from moving the inner crack front closer to the interface, meaning that for cracks of similar size, a crack closer to the particle/matrix interface is more severe.

The ring shaped crack results presented in Figures 3.33, 3.34, and 3.36 show the relative effects of the interface on stress intensity factors for ring shaped cracks near the interface for particles with aspect ratios of 1 and 8 for cracks having the same relative sizes, in proportion to the dimensions of the respective particles. However, the cross section radius of the spherical particle is twice that of the $b/a = 8$ particle, meaning that the ring shaped cracks in the spherical particle were twice the sizes of those in the $b/a = 8$ particle. Figure 3.37 shows finite element meshes for ring shaped cracks having the same absolute size for particles with aspect ratios of 1 and 8. The crack of length a/120 in the spherical particle (Figure 3.37a) is identical in absolute size to the crack of length a/60 in the particle with an aspect ratio of $b/a = 8$ (Figure 3.37b). Stress intensity factors resulting for these cracks are shown in Figure 3.38 for Young's modulus ratios of 0.1, 0.5, 1, 1.6, 3, 6, and 10. As with the penny shaped crack analyses, the results are normalized with respect to a penny shaped crack in aluminum having a radius equal to that of the constant volume spherical particle.

The trend shown in Figure 3.38 is similar to those observed for the penny shaped crack analyses shown in Figures 3.20 to 3.25. When the particles are stiffer than the

matrix, higher stress intensity factors result in the b/a = 8 particle than in the spherical particle. When the particles are more compliant, higher stress intensity factors result in the spherical particle. The relative differences between the finite element predictions for the cracks shown in Figure 3.37 and 3.38 and homogenous handbook solutions for the cracks in a continuum of the second phase material are shown in Figure 3.39. The results show that the a/60 crack in the b/a = 8 particle is affected by the interface to a much greater extent than the a/120 crack in the spherical (b/a = 1) particle, which is essentially unaffected by the interface, because the crack is larger in proportion to the particle cross section for b/a = 8.

If the relative potential for fracture between the two particle shapes is considered, it must be considered on the basis of similar initial flaws. In this study the similar initial flaw condition is taken to mean that flaws have the same absolute size and same relative distance from the interface. Figures 3.38 and 3.39 show that, for flaws near the interface for aspect ratios greater that one and for particles stiffer than the matrix, particles with higher aspect ratios will be more prone to fracture because both particle stress and crack size in proportion to the particle cross section increase as aspect ratio increases from 1.

3.6.3 Implications of Simulations of Cracks within Particles

Consideration of the results of the simulations of penny shaped cracks at the centers of particles and ring shaped cracks near the particle/matrix interface in particles with aspect ratios of 1 and higher leads to a number of important conclusions which are consistent with published literature but not reported specifically in relation to a second-phase particle fracture problem.

- If cracks within second phase particles are small with respect to the particle matrix interface they are unaffected by the interface and stress intensity factors are given by the continuum solution with the Eshelby Stress applied. In cases where similar initial flaws are small for each particle shape considered, the relative potential for fracture can be ranked on the basis of particle stress alone, without considering the effect of the particle matrix interface on stress intensity factor.

- Larger cracks in second phase particles are affected by the interface. Stress intensity factors for large cracks are elevated when the particle is stiffer than the matrix and are reduced when the particle is more compliant than the matrix.

- The effect of the interface on cracks within particles changes with Young's modulus ratio and is more significant for E_p/E_m ratios further from (either higher or lower) 1.

- The affect of the interface on stress intensity factor is stronger for cracks closer to the interface. Cracks far from the interface can be larger, without stress intensity factor being affected by the interface, than cracks close to the interface.

- The effect of the interface on stress intensity factor increases with crack size.

The following implications from the modeling of cracks within particles have not been reported in the literature.

- The effect of the interface on stress intensity factors for cracks in second phase particles changes with particle shape as the result of changes in stiffness of the

55

material behind the crack faces. The effect of the particle/matrix interface extends further into the particles as aspect ratio is reduced from 8 to 1.

- Whether a crack is "small" and unaffected by the interface, or "large" and affected by the interface depends on particle shape, crack location within the particle and crack size in proportion to the particle size. When considering particles of constant volume, which necessarily have cross sections of differing sizes, the effect of similar sized cracks will be different in different particles. If particles with similar sized flaws are considered in terms of the absolute flaw dimensions, the same flaw will be larger in proportion to the cross section, and thus more significantly affected by the interface, in a particle with an aspect ratio greater than 1, a long, thin ellipsoidal particle, than in a spherical particle. Thus, the same flaw could potentially be small, and unaffected by the matrix, in one particle and large, and affected by the matrix in another particle. The affect of the interface also depends on crack proximity to the interface, so if a comparison is to be made on the basis of similar flaws, the flaws must also have similar proximity to the interface.

3.6.4 Relative Potential for Fracture for b/a ≥ 1

One of the goals of modeling cracks within second phase particles was to determine, if similar initial flaws were present, whether shapes more or less prone to fracture could be identified and if the potential for fracture of the particle shapes considered could be ranked. Such a comparison is most relevant for cases where the particles are stiffer than the matrix. As shown previously, when the matrix is stiffer than the particle, stress intensity factor approaches zero near the interface, making crack arrest

56

likely. As such, the potential for fracture among particle shapes is considered for cases where the particle is stiffer than the matrix. This is first done for particles having aspect ratios greater than or equal to one because these particles had circular cross sections normal to the loading direction which allowed the simulation of cracks within those cross sections.

The relative potential for fracture among particle shapes is considered on the basis of similar initial flaws within the respective particles. Flaws are considered to have the same absolute size and the same relative position with respect to the particle/matrix interface. As discussed previously, the particles are considered on the basis of constant particle volume. Because the particles have constant volume, the cross sections change in size as aspect ratio changes. The cross section radius of the spherical particle is twice that of a particle with an aspect ratio of 8. Because of this it is possible for the spherical particle to contain a crack that is larger than the cross section of the $b/a = 8$ particle. So, when comparing potential for fracture among particles, the crack or flaw sizes considered must be small enough to be contained within the particles being compared.

If flaws within particles are small enough to be unaffected by the particle/matrix interface for each particle shape in the range of $b/a \geq 1$, then the relative potential for fracture can be ranked on the basis of the Eshelby Stress alone. The particle shape with the highest stress ($b/a = 8$) will have the highest stress intensity factor, for similar initial flaws, and will be most prone to fracture. As aspect ratio reduces from 8 to 1, particle stress, and potential for fracture, will reduce, making the spherical particle ($b/a = 1$) least prone to fracture.

In cases where the flaws are larger and/or closer to the interface, the effect of the interface on stress intensity factor must be accounted for when considering relative potential for fracture. When aspect ratio is reduced from 8 to 1, cross section diameter increases to maintain the constant particle volume condition of the comparison. When considering similar initial flaws, relative flaw size with respect to the particle cross section also reduces as aspect ratio is reduced. Because of this, the effect of the interface on stress intensity factor will reduce. So, as aspect ratio is reduced from 8 to 1, particle stress and the effect of the interface on stress intensity factor will both decrease. The result is that the effect of the interface on stress intensity factor cannot change the relative ranking of potential for particle fracture predicted by the Eshelby Stress for small cracks. This means that, for similar initial flaws, the relative potential for fracture for aspect ratios ranging from 1 to 8 can be ranked solely on the basis of the Eshelby Stress, without considering the effect of the particle/matrix interface on stress intensity factor.

3.7 Relative Potential for Fracture for b/a = 1/8 to b/a =8

The foregoing analysis of cracks within particles was limited to particles with aspect ratios of 1(spheres) and higher (prolate spheroids with circular cross sections aligned with the loading direction). Particles with aspect ratios less than 1, prolate spheroids with elliptical cross sections normal to the loading direction, were not considered because the particle geometry precluded the use of axi-symmetric models. In principle, cracks within such particles could be simulated with three-dimensional models, however such models would necessarily be very complex and likely less accurate than the axi-symmetric models used for the other cases. However, the analysis of particles with aspect ratios of 1

58

and higher can be used to provide some insight into the behavior of particles with aspect ratios less than 1.

As aspect ratio reduces from 1, the particle shape changes from a sphere to a prolate spheroid with the long axis normal to the loading direction. Cross sections of such particles, normal to the direction of loading, will be elliptical. As aspect ratio reduces from 1, the particles progressively shorten in the loading direction. As with the preceding analysis, if cracks in particles with aspect ratios less than one are small enough to be unaffected by the particle/matrix interface then the potential for fracture can be ranked on the basis of the Eshelby Stress alone. When considering the effect of the particle/matrix interface the question which must be asked is whether the effect of the interface on stress intensity factor can change the ranking in potential for fracture predicted with the Eshelby Stress. Because cracks within particles having elliptical cross sections cannot be modeled, this question cannot be answered with certainty. However, several cases can be considered which provide insight into this question.

The first case considers penny shaped cracks located at the centers of particles having elliptical and circular cross sections, Figure 3.40. Plots of the homogenous, analytic solution for stress intensity factor for penny shaped cracks approaching the particle/matrix interface for these particles are shown in Figure 3.41 for aspect ratios ranging from 1/8to 8. As with the prior analysis, the curves extend from zero to 2a/3 for the particles with circular cross sections. For the particles with elliptical cross sections, cracks at the centers of the cross sections would first approach the particle/matrix interface on the minor axes of cross sections. So, in the figure, the curves extend to 2b/3, where b is the minor dimension of the ellipse. The case shown is for a Young's modulus

ratio of Ep/Em = 10. This case was chosen because it results in the greatest spread in Eshelby Stress among the particles. Even for this case, the stress intensity curves for b/a = 1/8, 1/4, and 1/2 are nearly coincident because difference in stress among these particle shapes is small. The stress, and thus stress intensity factor, is lowest for b/a = 1/8. Stress and stress intensity factor increase slightly as aspect ratio increases to 1/4 and then to 1/2. Figure 3.42 shows the penny shaped crack solutions again with curves extending toward the particle/matrix interface added. For aspect ratios of 1 and higher the curves extending from 2a/3 toward the interface are given by finite element solutions. The near interface curves for b/a = 1/8, 1/4, and 1/2 are not calculated. Instead they are sketched in as an approximation. Although the nature of the transition from the homogenous penny shaped crack solutions to near interface behavior is not known, it is known that the solutions must go to infinity at the interface. While the shapes of the curves are not known, it is clear that the curve for b/a = 1/8 must cross over the curves for b/a = 1/4, 1/2, 1, 2, and 4 as it approaches the interface. The curve for b/a = 1/4 must cross those for b/a = 1/2, 1, and 2. The curve for b/a = 1/2 must cross the curve for b/a = 1. The stress intensity factor curves for particles with aspect ratios less than one crossing those for particles with higher aspect ratios means the ranking in potential for fracture that would predicted with a comparison of Eshelby Stress is changed by the effect of the particle/matrix interface on stress intensity factor. As cracks in particles with lower aspect ratio increase in size and approach the interface, the effect of the interface causes the stress intensity factor to become greater than in more the highly stressed particles which would more prone to fracture with the presence of smaller cracks. For this behavior to occur, the cracks in the particles, particularly those with

lower aspect ratios, must be relatively large with respect to the particle cross sections. While this requirement may make the comparison somewhat unrealistic, because the lower aspect ratio particles must have cracks through most of their cross sections, it is a clear and real exception to the trend that would be predicted with the Eshelby Stress.

Another case considered involves smaller flaws located near the particle matrix interface in particles with elliptical and circular cross sections, Figure 3.43. Potential cracks or flaws could be located anywhere in the cross section but are assumed to have the same absolute size and same relative distance from the interface in the particles being compared. The particles are again considered to be stiffer than the matrix. If the cracks are small enough, even if they are near the interface, the interface will not affect stress intensity factor and the potential for fracture can be ranked on the basis of the magnitude of the Eshelby Stress. A particle with an aspect ratio of $b/a = 1/8$ will have the lowest potential for fracture and this will increase progressively with aspect ratio due to the increase in Eshelby Stress with aspect ratio for $Ep/Em > 1$.

As aspect ratio decreases from 1 to 1/8, particle stress decreases. Crack size, while remaining constant in size, will change in proportion to the particle cross section as aspect ratio is reduced. If the flaw is located on the minor axis it will become larger with respect to the minor dimension as aspect ratio is reduced. If the flaw is located on major axis it will become smaller with respect to this axis but more of the flaw will become close to the interface as the cross section narrows. Because of the increase in crack size, relative to the particle cross section, or the increase in the amount of the flaw near the interface, depending on flaw location within the elliptical cross sections, the effect of the interface on stress intensity factor may increase as aspect ratio is reduced from 1. A

potential result is that, if the flaws are large enough, the effect of the interface in increasing stress intensity factor as aspect reduces from 1 may outweigh the effect of reducing stress and change the ranking in potential for fracture that would be predicted by only considering the Eshelby Stress. Since cracks in particles with elliptical cross sections have not been simulated, changes in particle ranking from that predicted with the Eshelby Stress cannot be confirmed. However, trends in crack size in relation to particle size and the trend in particle stress suggest that such changes could occur if the initial cracks or flaws are large enough.

3.8 Consideration of Random Particle Orientation

The analyses conducted in Chapter 3 indicate that, for conditions of similar flaws at similar locations, prolate spheroid particles with higher aspect ratios will result in higher stress intensity factors while prolate spheroid particles with lower aspect ratios will result in lower stress intensity factors. If second phase particles are oriented randomly, as may occur in a particulate reinforced composite, then the behavior of prolate spheroid particles will range from that represented by a particle with a lower aspect ratio (1/8 for example) to that represented by a higher aspect ratio (8 for example). This is because reciprocals in aspect ratio represent a 90 degree rotation with respect to the loading direction. Particles with aspect ratios greater than 1 have the major axis aligned with the loading direction, while particles with aspect ratios less than 1 have the minor axis aligned with the loading direction. As a result, for random particle orientation, the same particle shape can yield higher or lower stress intensity factors for included flaws, depending on the orientation of the particle with respect to the applied

load. If stiffer particles are added to a more compliant matrix, the largest contribution to increased composite stiffness will come from particles aligned with the loading direction, as they will develop higher levels of stress. This may come with a penalty of increased potential for fracture. In the design of a composite system, the two effects must be balanced to achieve the properties desired while minimizing the potential for fracture. The response of spherical particles is independent of orientation. Spherical particles offer decreased potential for fracture compared to a long thin particle aligned with the load, if similar flaw size and location is considered, but with a lower potential increase in composite stiffness, due to reduced particles stress.

3.9 Consideration of Particle Size

If second phase particles are considered on the basis of constant particle volume, different particle shapes will have different cross section sizes normal to the direction of loading. For any given particle material and initial flaw configuration (flaw geometry and location within the particle) a critical flaw size will exist. Reducing particle size can potentially result in particles that are smaller than the critical flaw size and which could not fracture. Particles with aspect ratios greater than 1 have smaller cross sections normal to the loading direction. It is possible that such particles, in which similar flaws would have higher stress intensity factors, could be small enough that they could not fracture, while particles with lower aspect ratios (and larger cross sections) could be prone to fracture. Reducing particle size, for any shape, could potentially result in particles being smaller than the critical flaw size.

3.10 CONCLUSIONS

In Chapter 3, particle fracture was considered through the application of Fracture Mechanics, first with three-dimensional finite element models that simulated the strain energy released by cracking entirely through the particles and then with a combination of two dimensional axi-symmetric finite element models and homogenous solutions for cracks of varying sizes at differing locations in particles. The analyses showed that, if the cracks or flaws within particles are sufficiently small, they are unaffected by the matrix and the only difference between the particles is the Eshelby Stress and that when cracks are large enough or close enough to be affected by the interface, the particle fracture problem becomes very complex. The following are the primary contributions of the Chapter 3 fracture analyses:

- Conducting the first systematic Fracture Mechanics analysis for three-dimensional brittle particles.

- Mapping out particle fracture to show the transition from continuum to asymptotic behavior as a function of particle shape and of Young's modulus mismatch between the particle and the matrix to show how the classical Eshelby Problem can be analyzed as a fracture problem

- Identifying cases where the relative potential for fracture among a range of particle shapes can be ranked on the basis of the Eshelby Stress alone and identifying cases where exceptions to this ranking may exist.

- Identifying the effect of particle shape on the near interface asymptotic behavior of stress intensity factor and showing how this behavior changes

with particle shape and thus differs from the behavior established for linear interfaces in the literature.

Table 3.1

Particle dimensions for constant volume (CPV) particles.

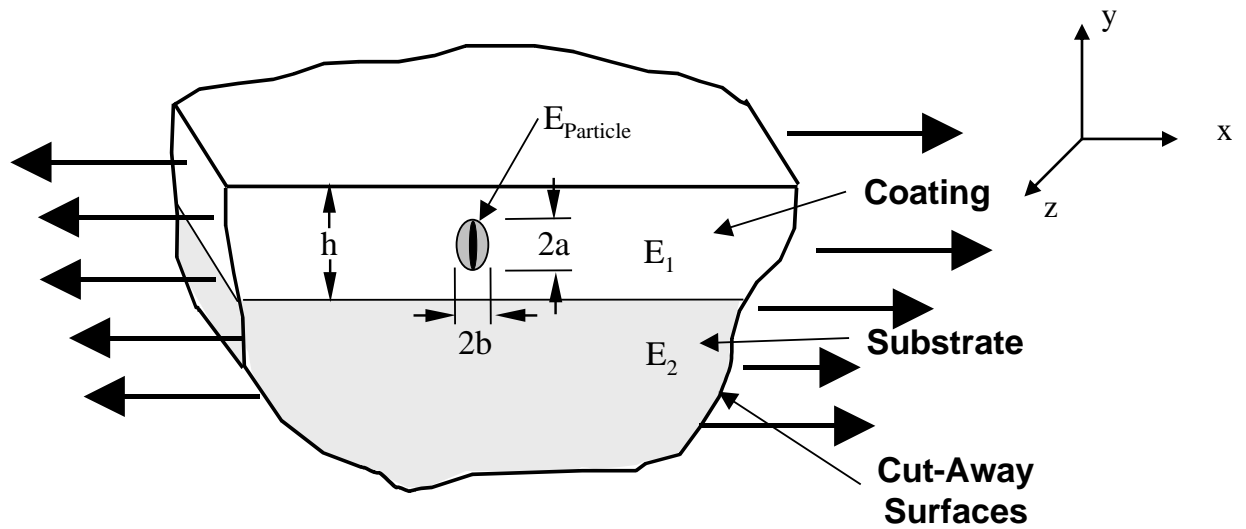| Aspect Ratio (b/a)	2a (micro-inch)	2b (micro-inch)
1/8	5.00×10^{-4}	6.25×10^{-5}
1/4	3.15×10^{-4}	7.87×10^{-5}
1/2	1.98×10^{-4}	9.92×10^{-5}
1	1.25×10^{-4}	1.25×10^{-4}
2	9.92×10^{-5}	1.98×10^{-4}
4	7.87×10^{-5}	3.15×10^{-4}
8	6.25×10^{-5}	5.00×10^{-4}

Figure 3.1   Schematic of substrate, overlying coating and cracked particle. Large
arrows indicate direction of tensile strain.

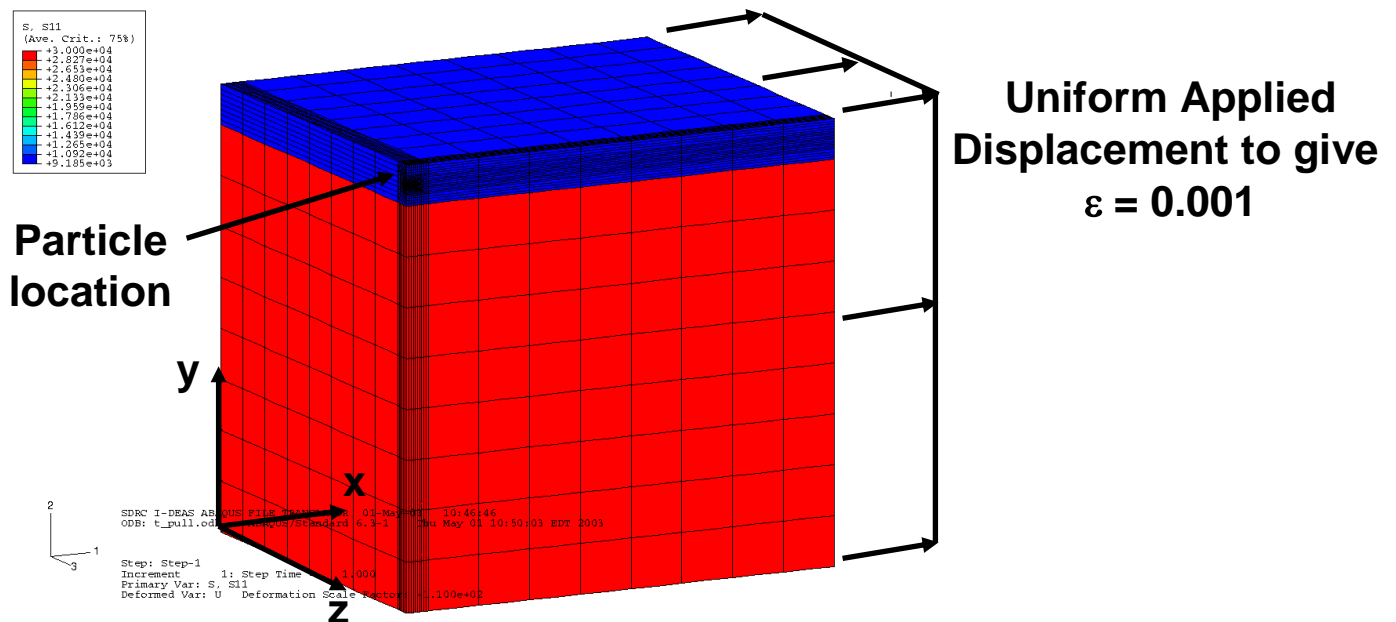Figure 3.2   Typical finite element mesh used for three-dimensional particle stress (as
shown here) and particle fracture simulations.   For particle stress
simulations a uniform displacement is applied to give a far-field strain of
0.001.

$b/a = 1/8$

$b/a = 1/4$

$b/a = 1/2$

$b/a = 1$

$b/a = 2$

$b/a = 4$

$2a = 0.05"$

c

b

$b/a = 8$
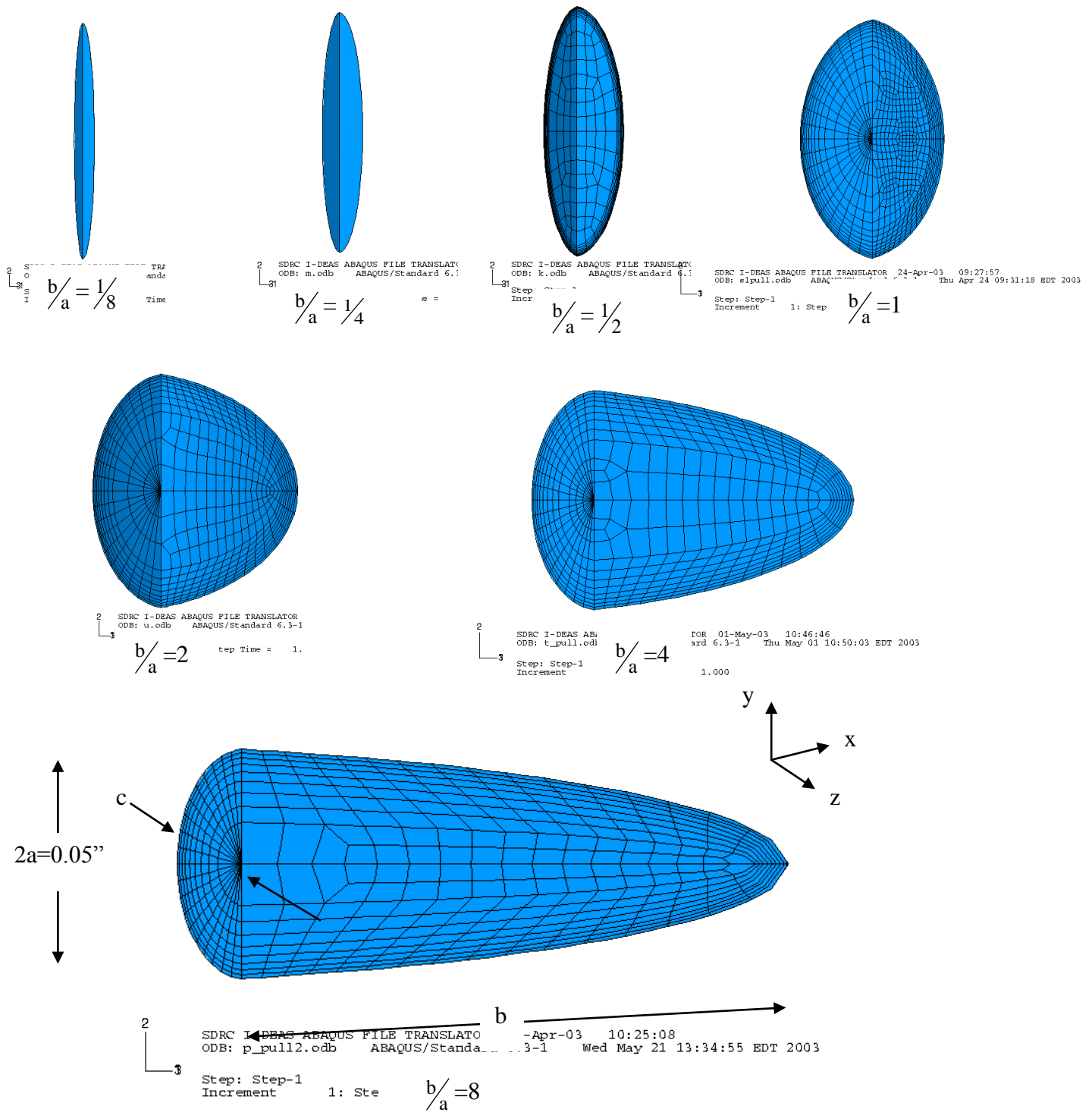
Figure 3.3   Schematic showing particle shapes for constant particle height simulations.

y

x

z

b

c

a

$$\frac{b}{a} = \frac{1}{8}$$

$$\frac{b}{a} = \frac{1}{4}$$

$$\frac{b}{a} = \frac{1}{2}$$

$$\frac{b}{a} = 1$$

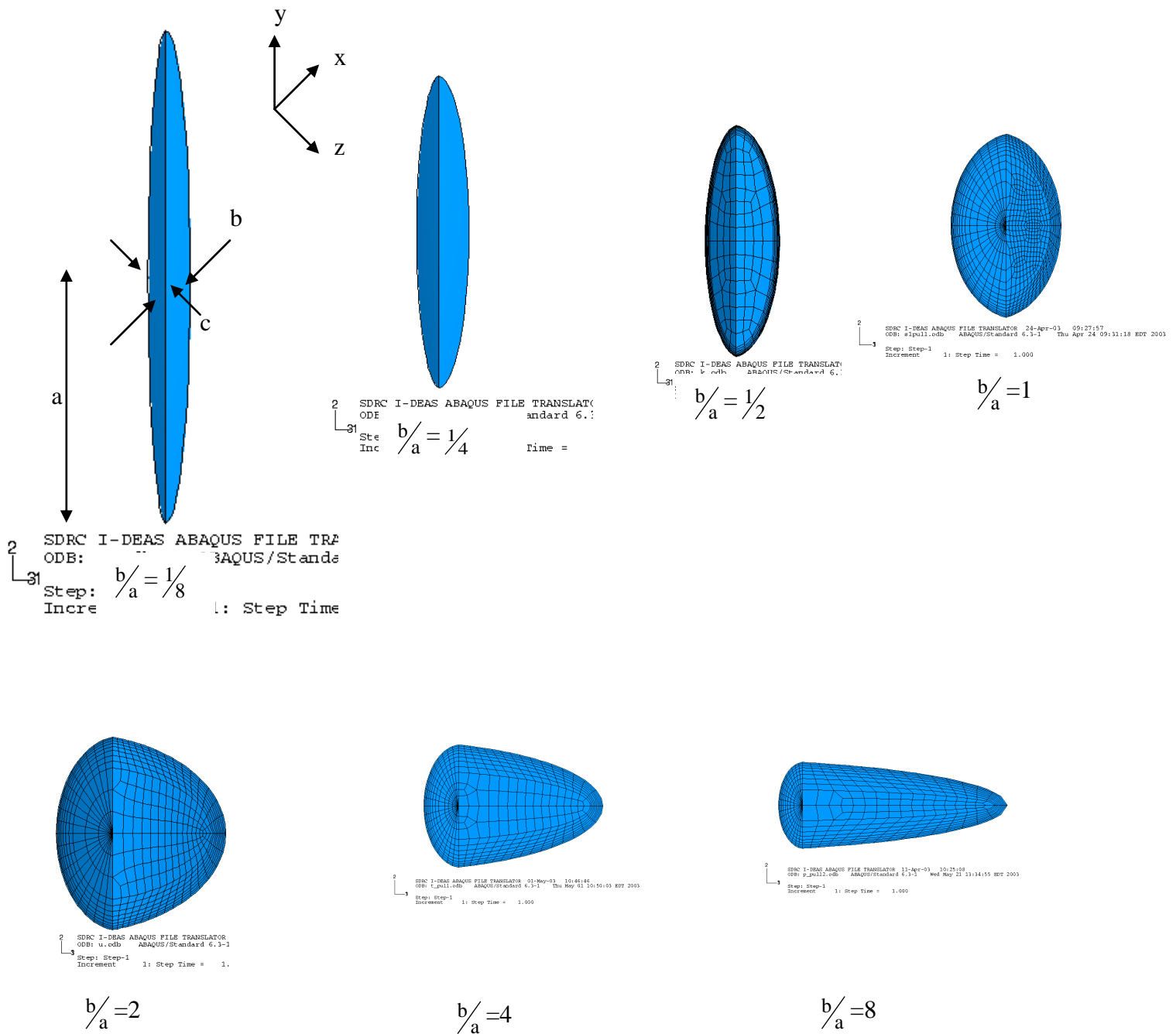$$\frac{b}{a} = 2$$

$$\frac{b}{a} = 4$$

$$\frac{b}{a} = 8$$

Figure 3.4   Schematic showing particle shapes for constant particle volume simulations. As b/a increases from 1/8 the particle height, 2a, decreases to maintain constant volume.
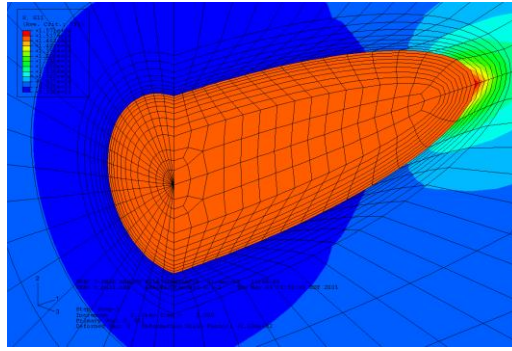
Figure 3.5   Detail of a silicon particle, in this case for a particle stress simulation with b/a = 4. A uniform far-field strain of 0.001 results in a constant stress (in the x-direction) of 14,706 psi in the particle.
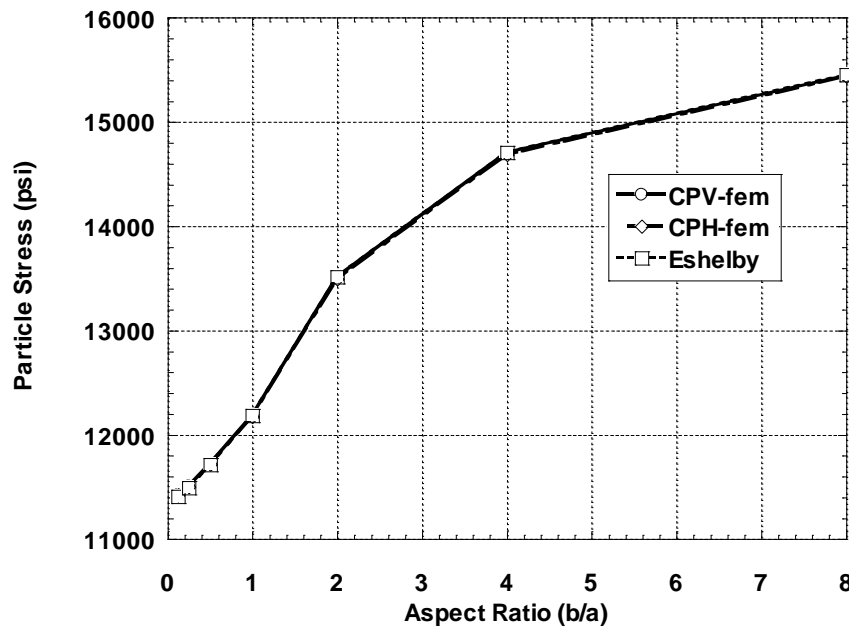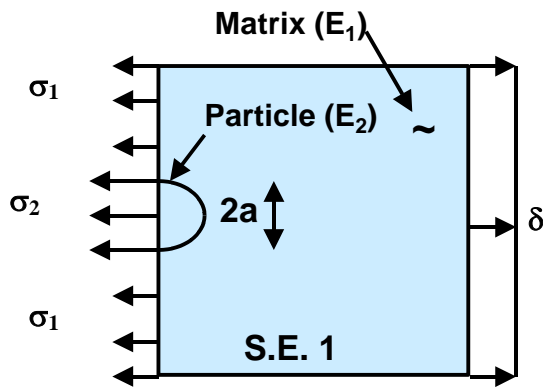

Figure 3.6   Comparison of predictions of particle stress from finite element simulations of the particle-coating-substrate system and from the Eshelby Solution for particles in a continuum comprised of the coating material.
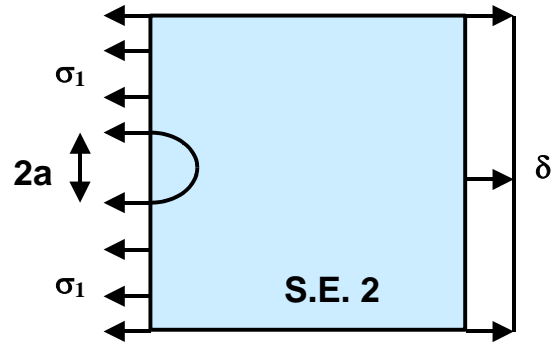
70

Case 1 (uncracked particle)

application of displacement, δ, requires surface tractions, σ_1 and σ_2, for equilibrium ($\sigma_2 > \sigma_1$ for $E_2 > E_1$),

strain energy S. E. 1 stored in body

Case 2 (fully cracked particle)

introduction of crack, by removal of surface traction over length 2a, results in reduction in strain energy:

S. E. 2 < S. E. 1,
S. E. released = S. E. 1 - S. E. 2
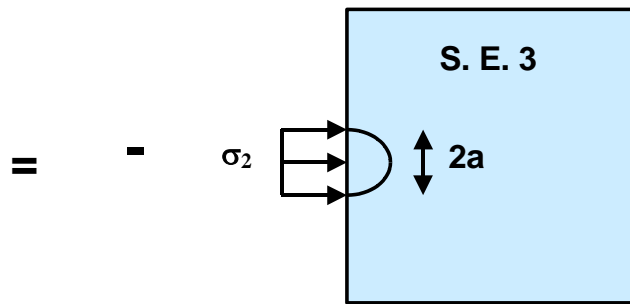
Case 3 (pressurized crack problem)

surface traction, σ_2, applied to crack face: resulting strain energy, S. E. 3, equals the negative of the strain energy difference between Cases 1 and 2

S. E. 1 + S. E. 2 = - S. E. 3 = - S. E. released

Figure 3.7 Schematic for determination of strain energy released through particle fracture. Pressurized crack face models (Case 3) with stress determined from particle stress simulations (Case 1) can be used to determine the strain energy released by the introduction of a through particle crack (Case 1 to Case 2).

71
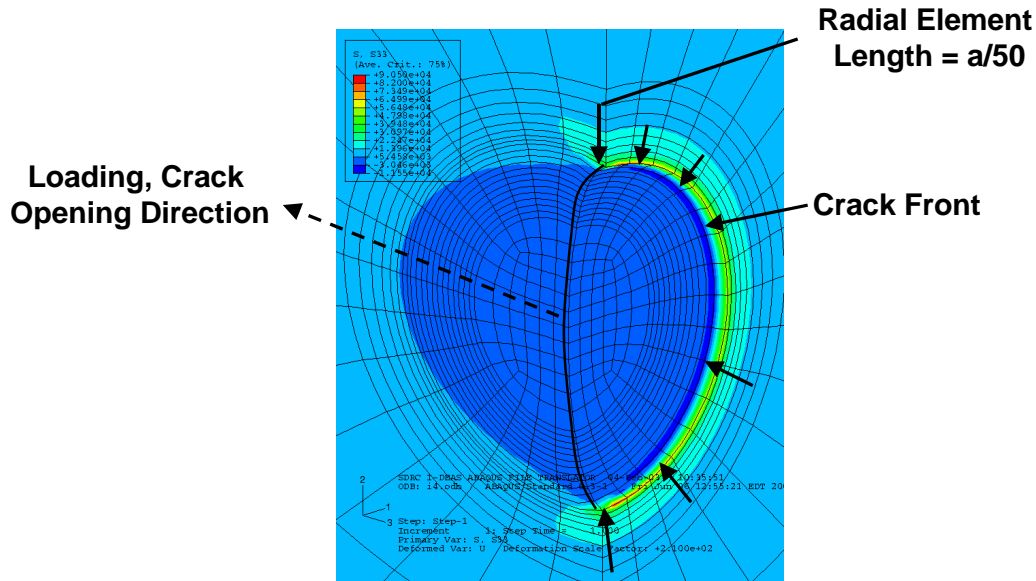
Figure 3.8   Detail of the finite element mesh used for model verification. A penny shaped crack in a continuum of coating material was simulated. The average energy release rate for the finite element model agreed with the analytic solution to within 1.3 percent.
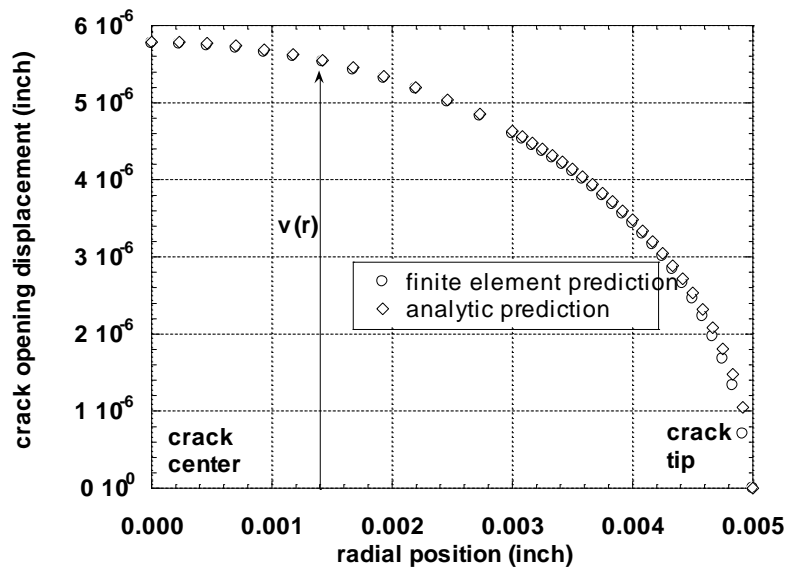
Figure 3.9   Comparison between finite element and analytic predictions of crack opening displacement for the verification (penny-shaped crack) problem.
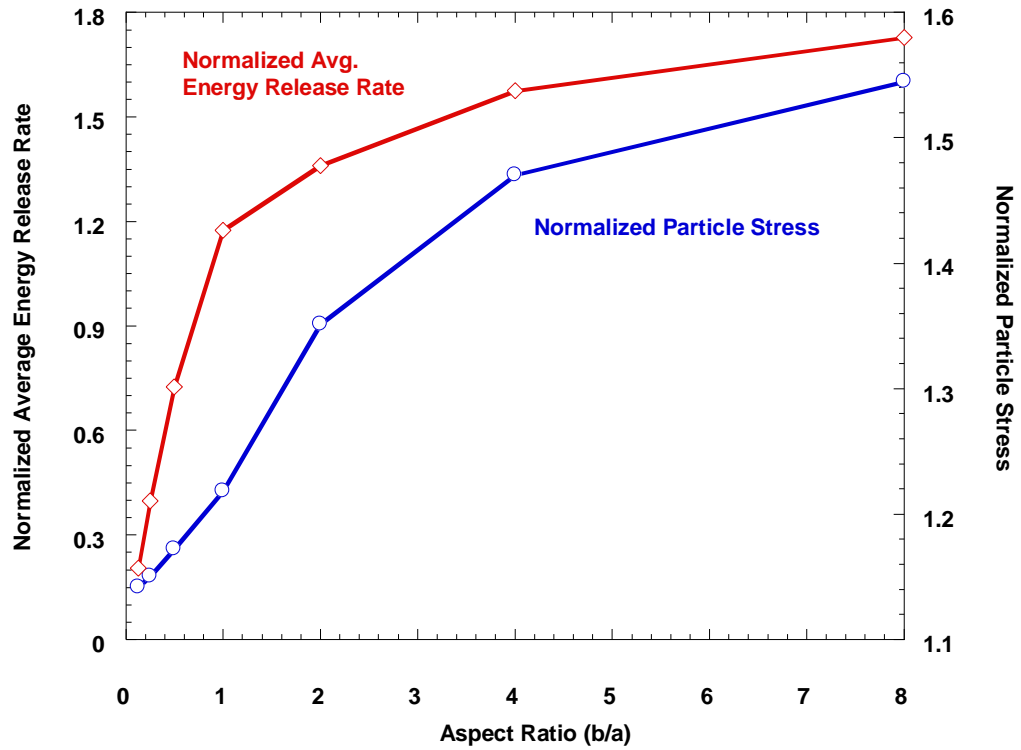
Figure 3.10   Results for constant particle height simulations.
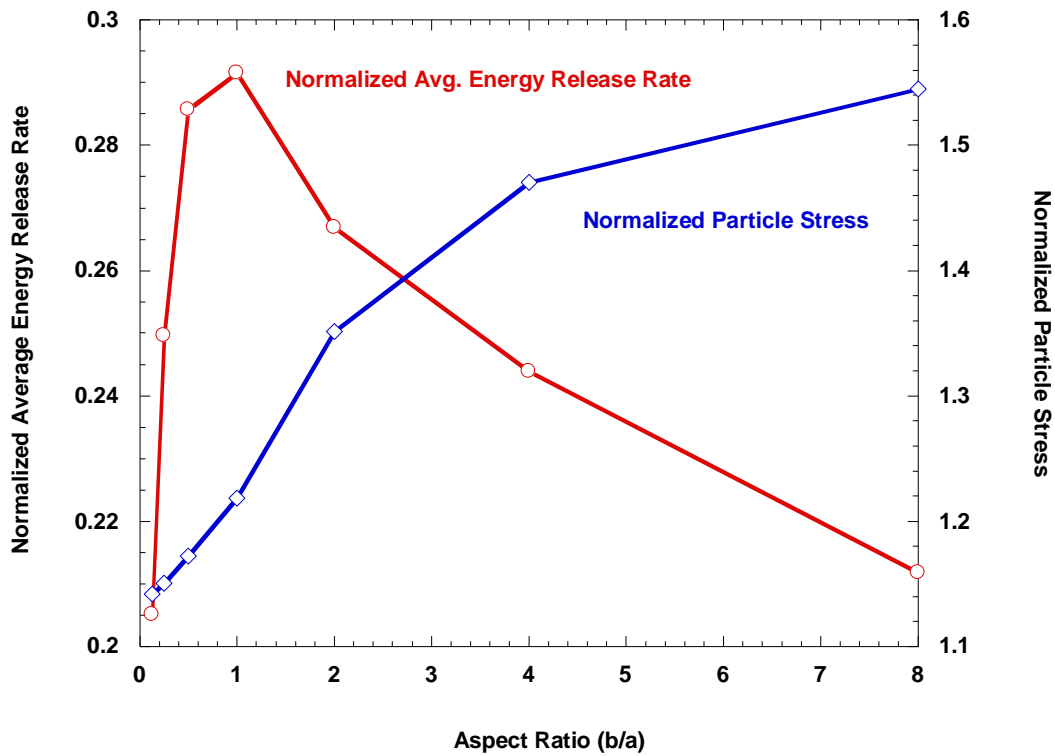
Figure 3.11   Results for constant particle volume simulations.
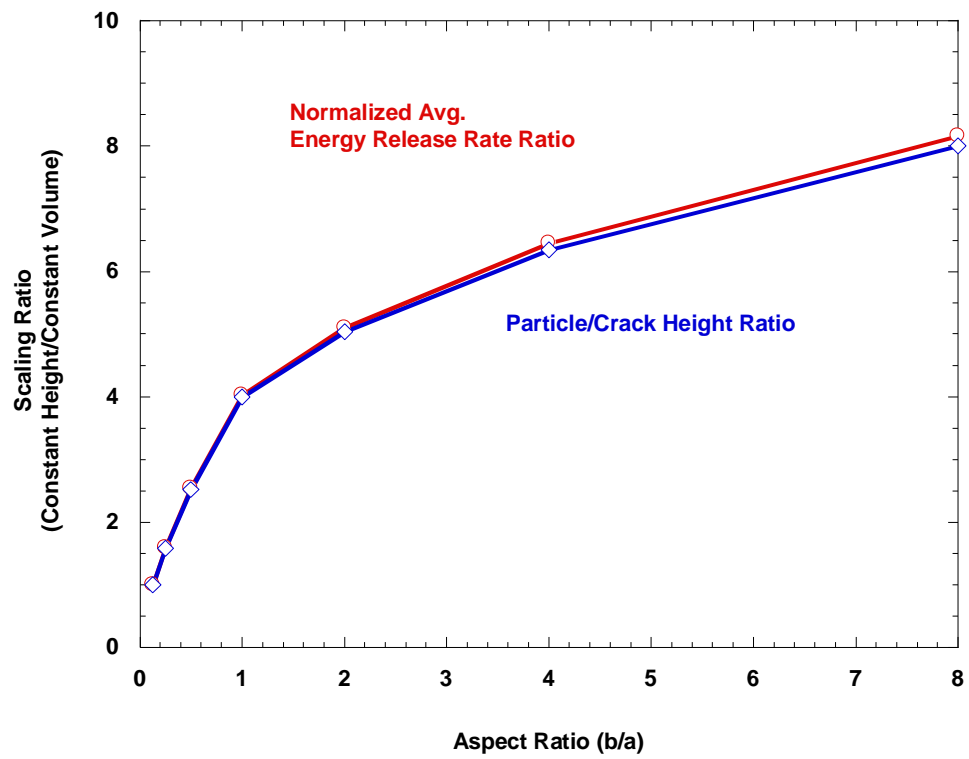
Figure 3.12   Comparison of scaling between particle/crack height and normalized average energy release rate for constant height and constant volume particles.
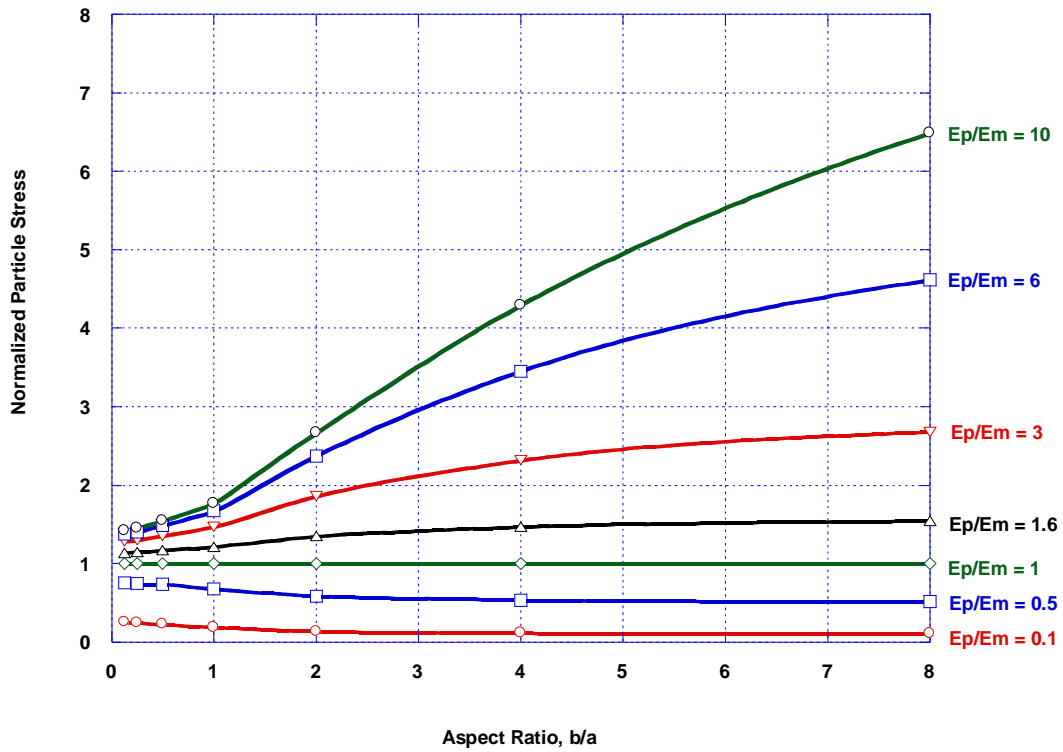
Figure 3.13   Eshelby particle stresses for ellipsoidal particles with aspect ratios ranging from b/a = 1/8 to b/a = 8. Results are shown for ratios of Young's modulus of the particle (Ep) to Young's modulus of the matrix (Em) ranging from Ep/Em = 0.1 to Ep/Em = 10. Particle stress is normalized with respect to the aluminum matrix stress (10,000 psi).

**Uniform Applied
Displacement to give
$\varepsilon = 0.001$**

Axi-symmetry axis

Matrix

Ellipsoidal
particle

b

a
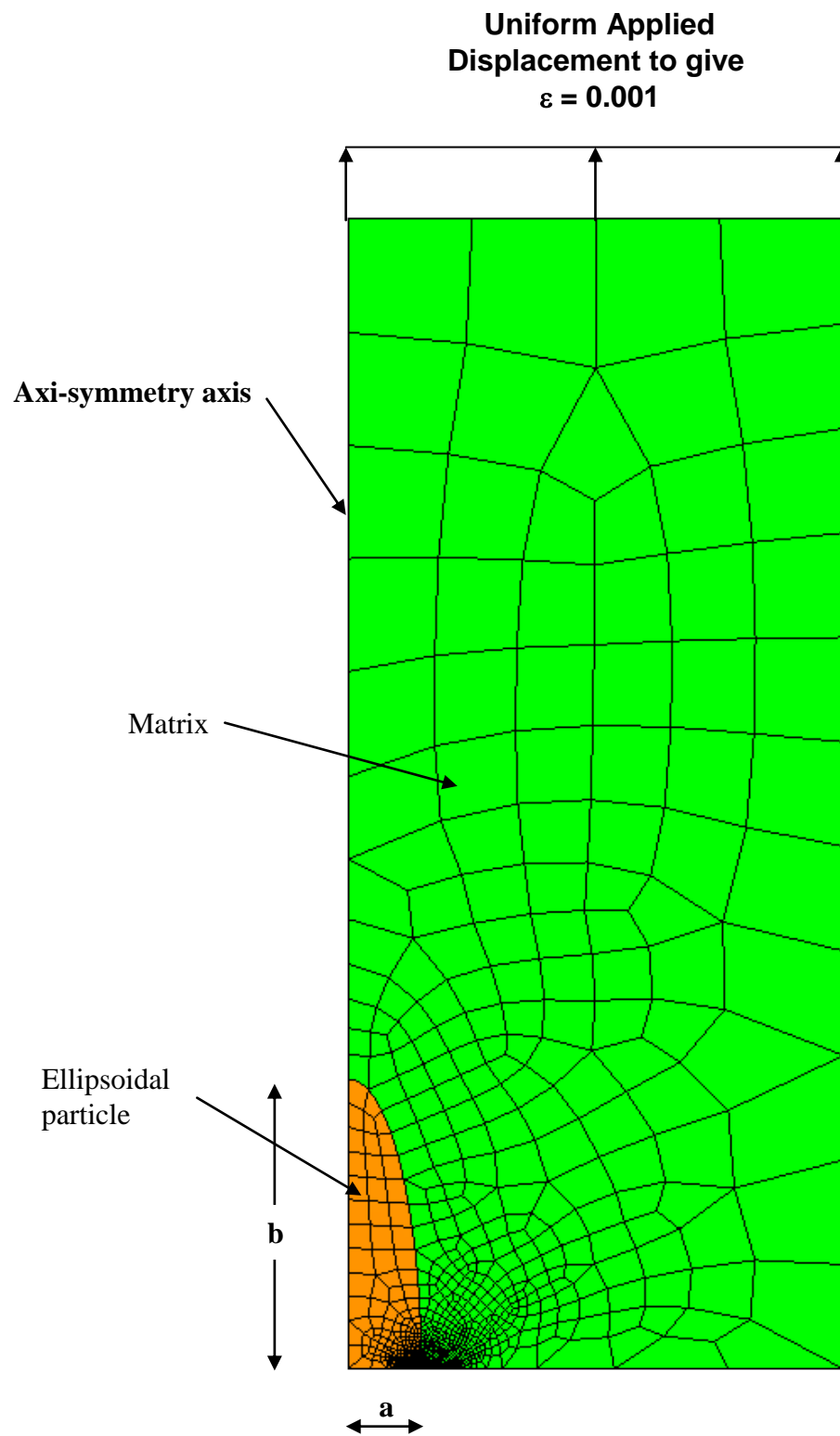
Figure 3.14 An example of an axi-symmetric finite element mesh used for the estimation of stress intensity factors for cracks in and beyond particles.

Particle   Matrix

$\dfrac{a}{3}$ $\dfrac{a}{5}$ $\dfrac{a}{10}$ $\dfrac{a}{20}$ $\dfrac{a}{30}$ $\dfrac{a}{60}$ **Typical crack tip location**
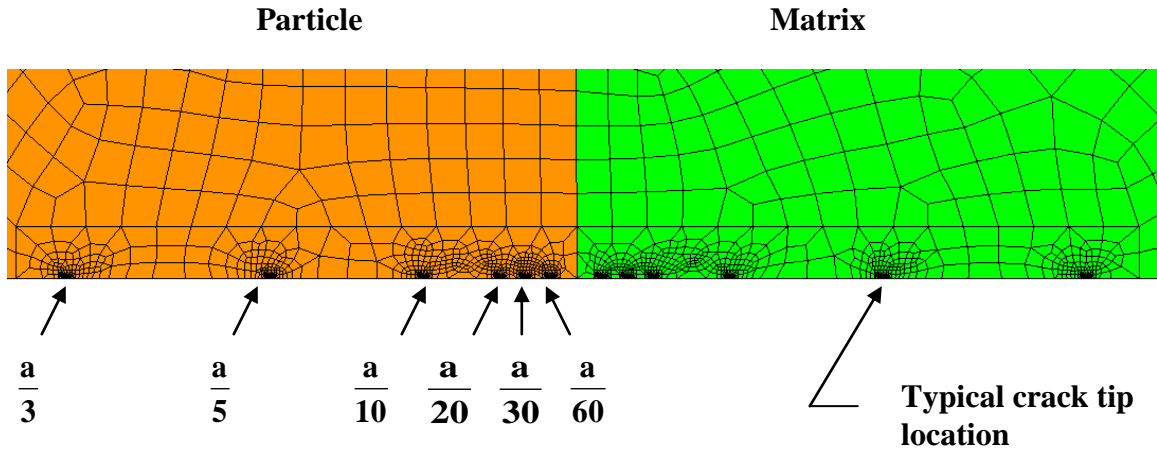
Figure 3.15   A detail of the mesh near the particle/matrix interface showing fine-mesh zones at each of the crack tip locations. Relative distances of the crack tip locations from the particle/matrix interface are indicated as fractional values of the particle cross section radius, a. Crack tip locations in the matrix are located at similar distances from the interface.

Typical crack tip location
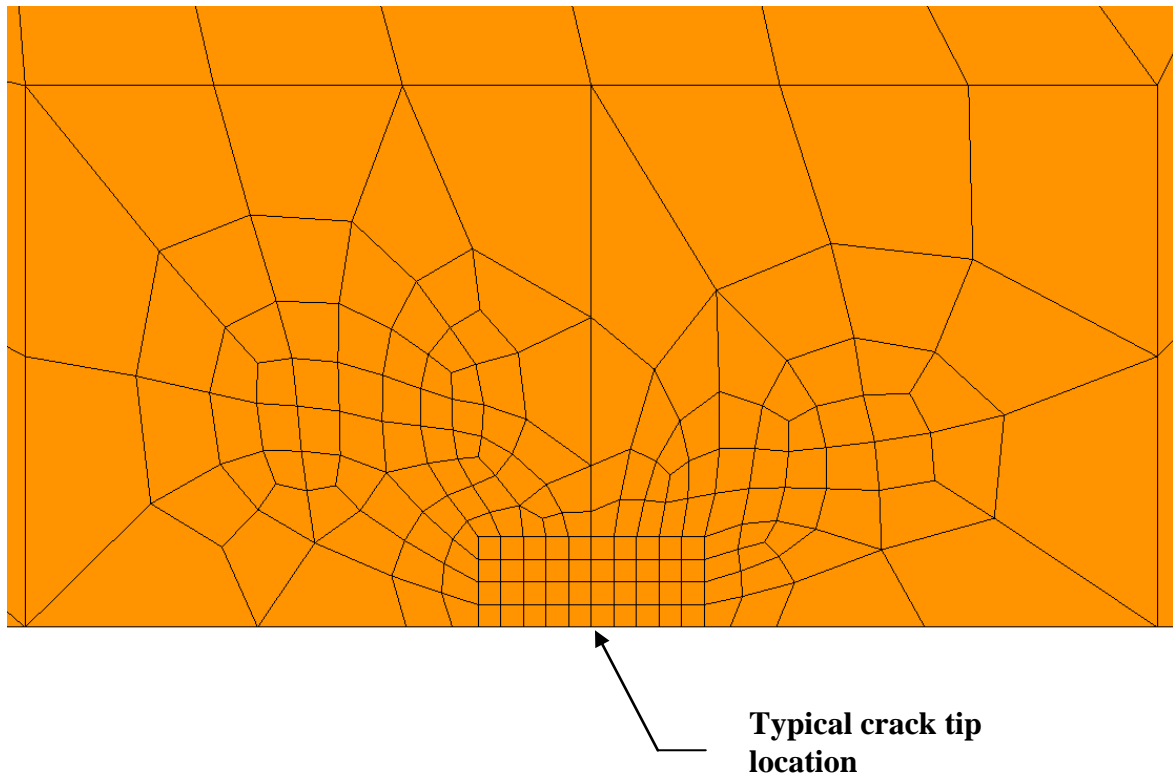
Figure 3.16   Detail of a fine mesh region at a crack tip location. Local element lengths were a/3125 or smaller, depending on particle aspect ratio.
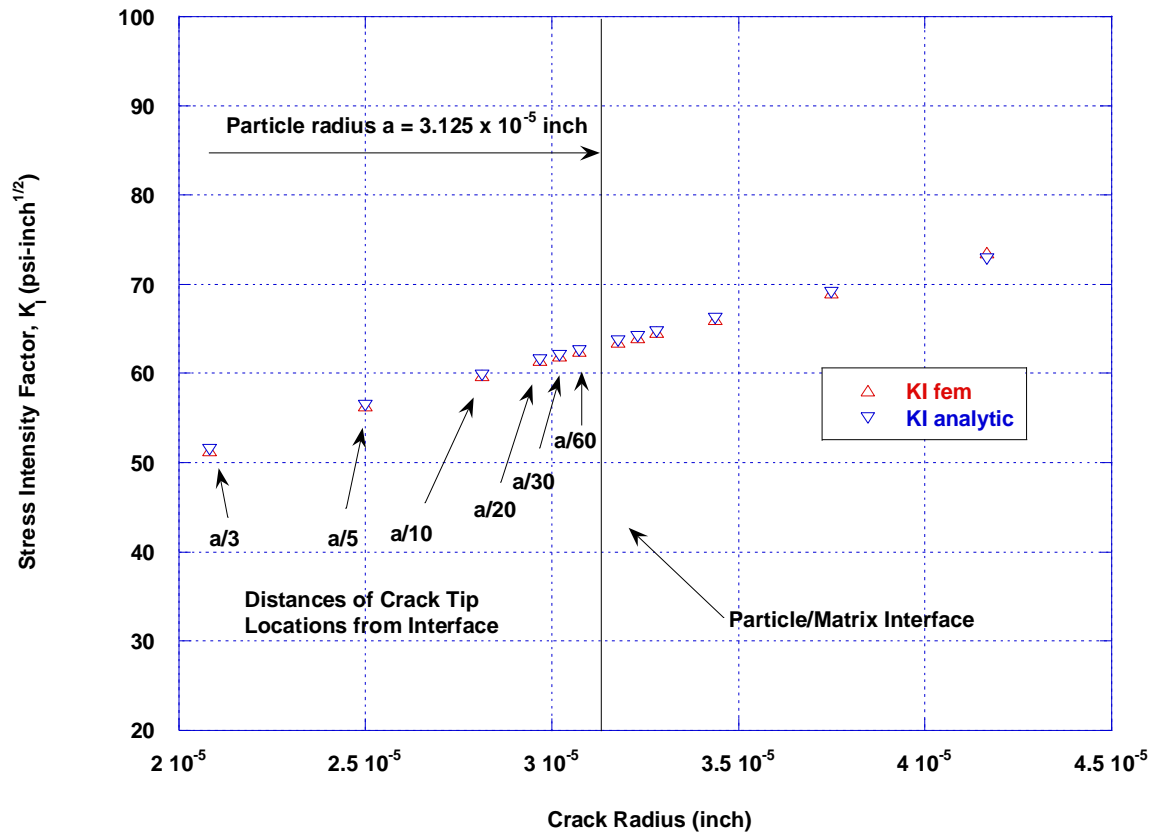
Figure 3.17 Comparison of finite element predictions of stress intensity factors with values calculated from the analytic solution for a penny shaped crack in a continuum using constitutive properties of aluminum for the particle and the matrix. The particle considered has an aspect ratio of 8 and dimensions of $2a = 6.25 \times 10^{-5}$ inch and $2b = 5.00 \times 10^{-4}$ inch.
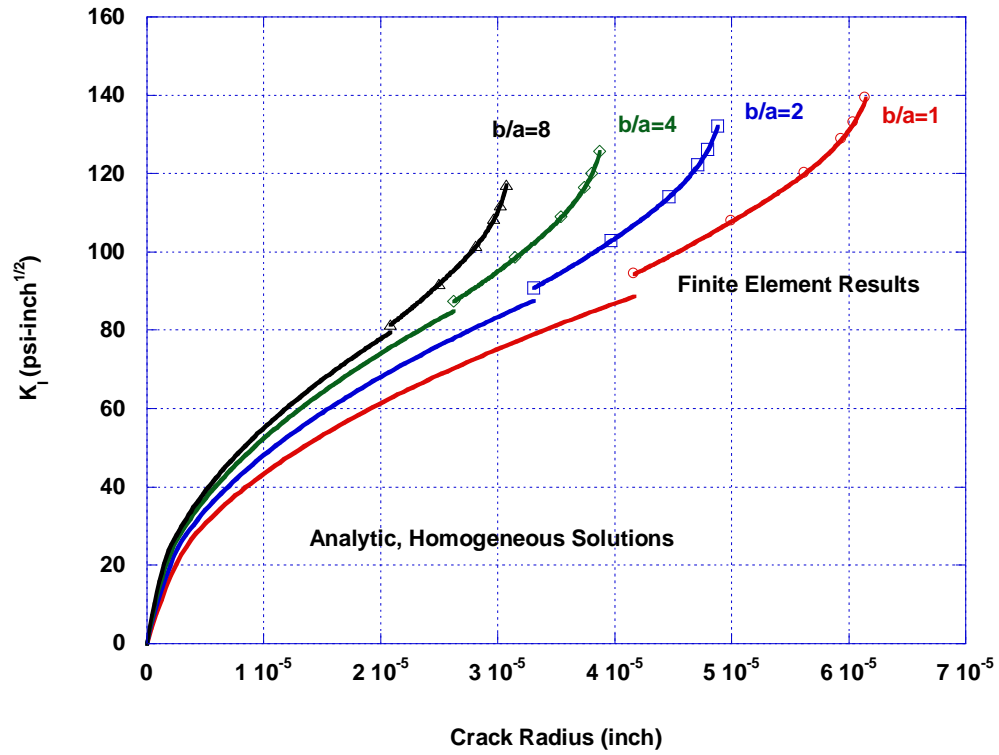
Figure 3.18   Stress intensity factors for penny shaped cracks located at the centers of the particle cross sections for silicon particles in aluminum (Ep/Em = 1.6) for aspect ratios of 1, 2, 4, and 8.
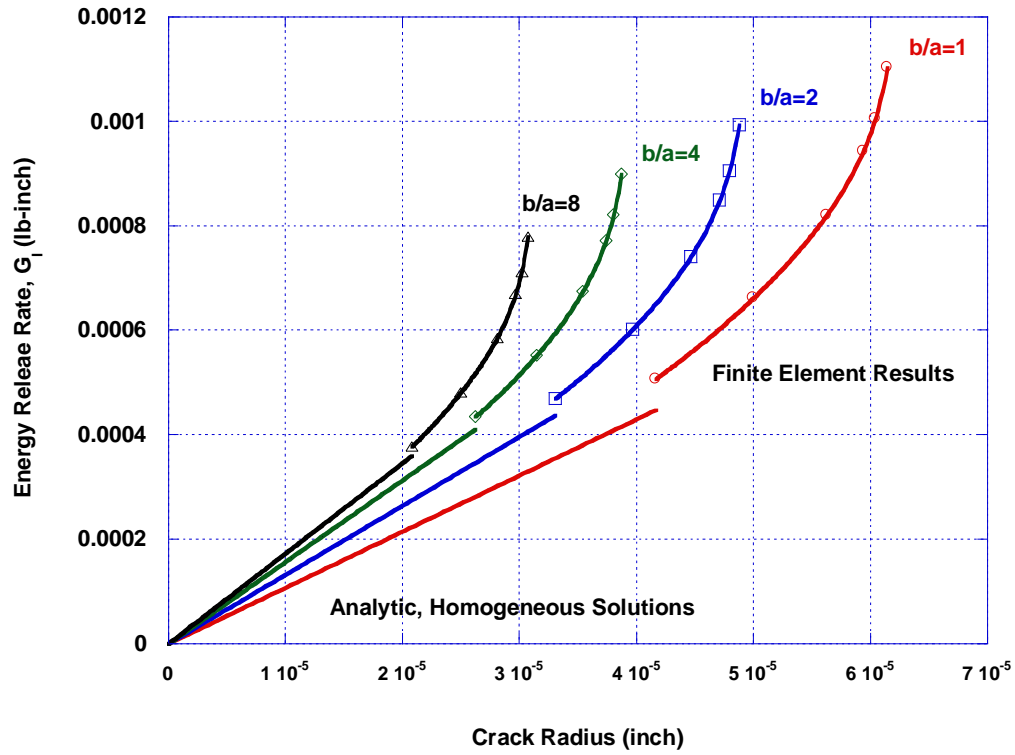
Figure 3.19   Energy release rates for penny shaped cracks located at the centers of the particle cross sections for silicon particles in aluminum (Ep/Em = 1.6) for aspect ratios of 1, 2, 4,and 8.
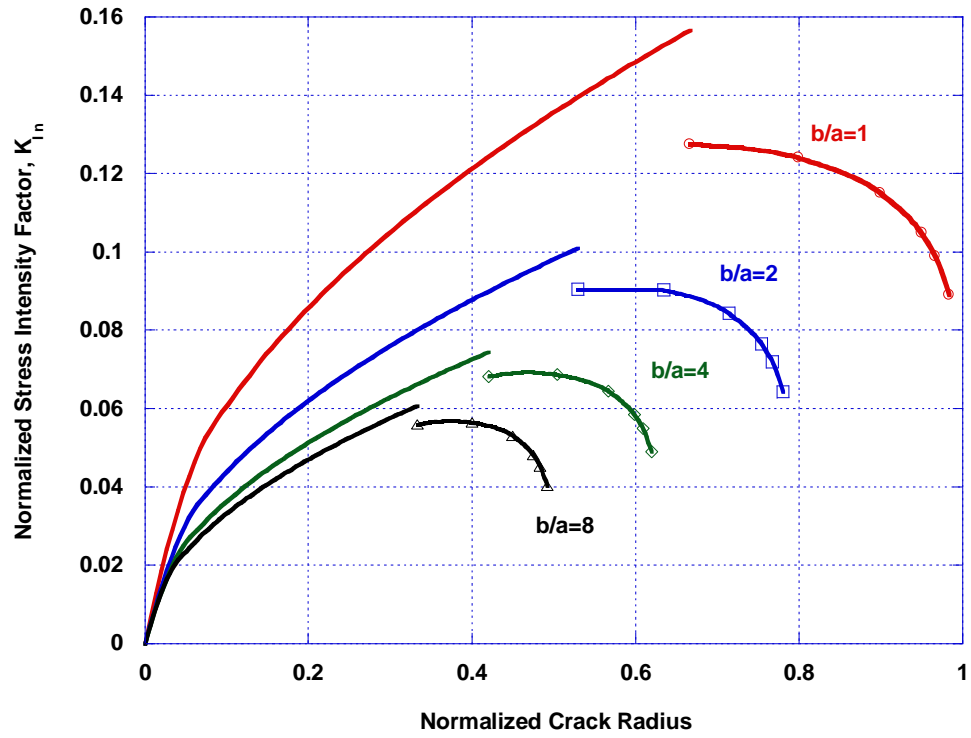
Figure 3.20   Normalized stress intensity factors for penny shaped cracks located at the centers of the particle cross sections for Ep/Em = 0.1 for aspect ratios of 1, 2, 4, and 8.
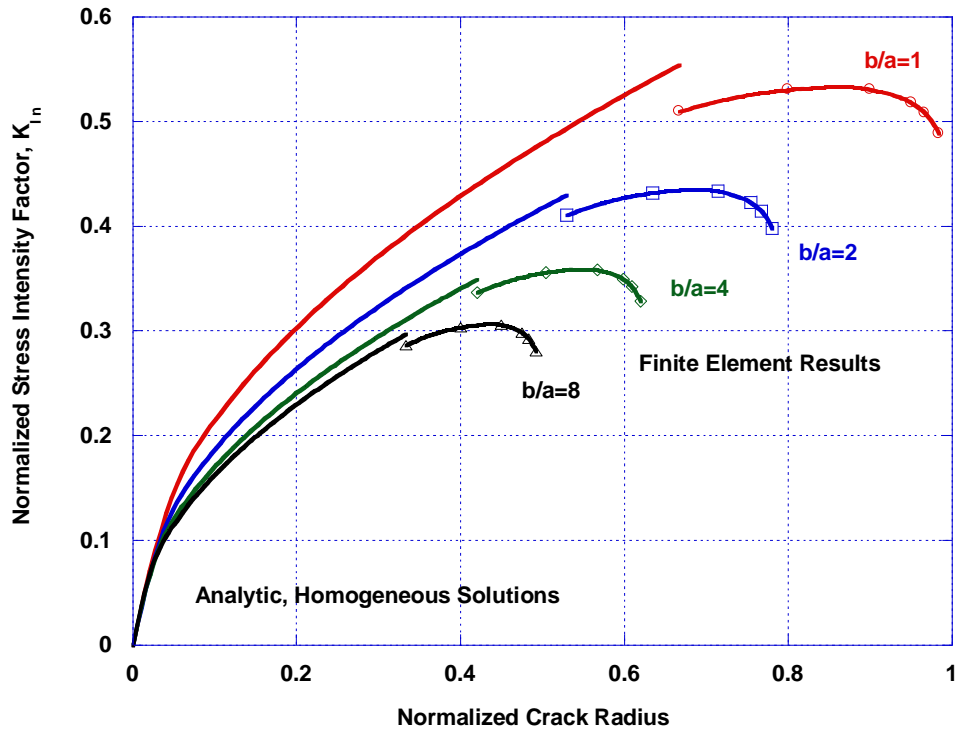
Figure 3.21   Normalized stress intensity factors for penny shaped cracks located at the centers of the particle cross sections for Ep/Em = 0.5 for aspect ratios of 1, 2, 4, and 8.
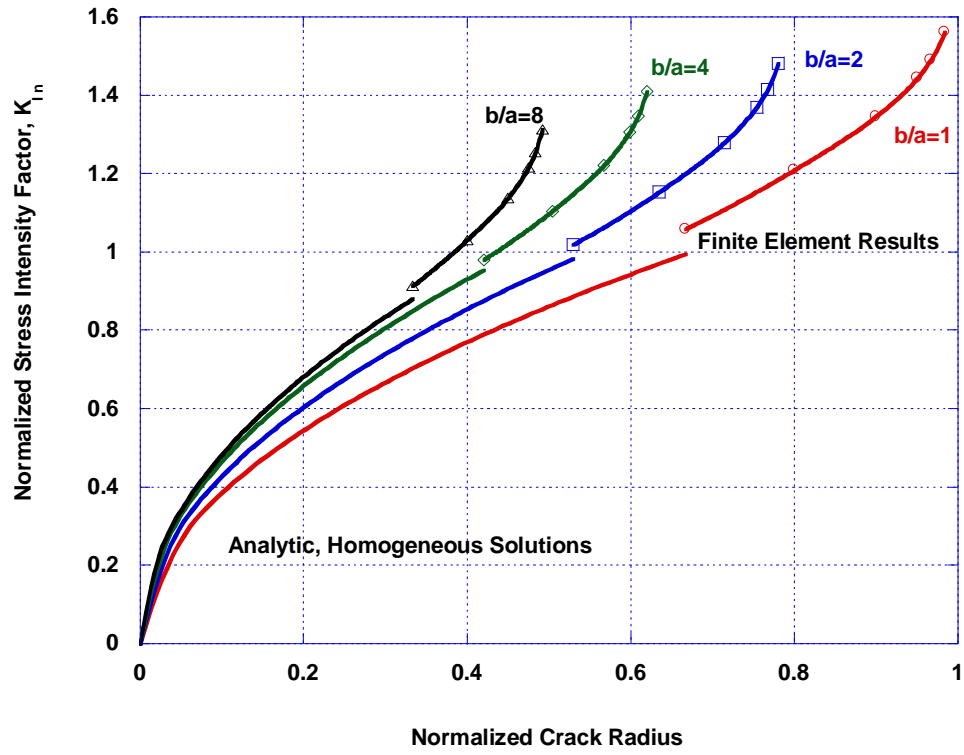
Figure 3.22   Normalized stress intensity factors for penny shaped cracks located at the centers of the particle cross sections for Ep/Em = 1.6 for aspect ratios of 1, 2, 4, and 8.
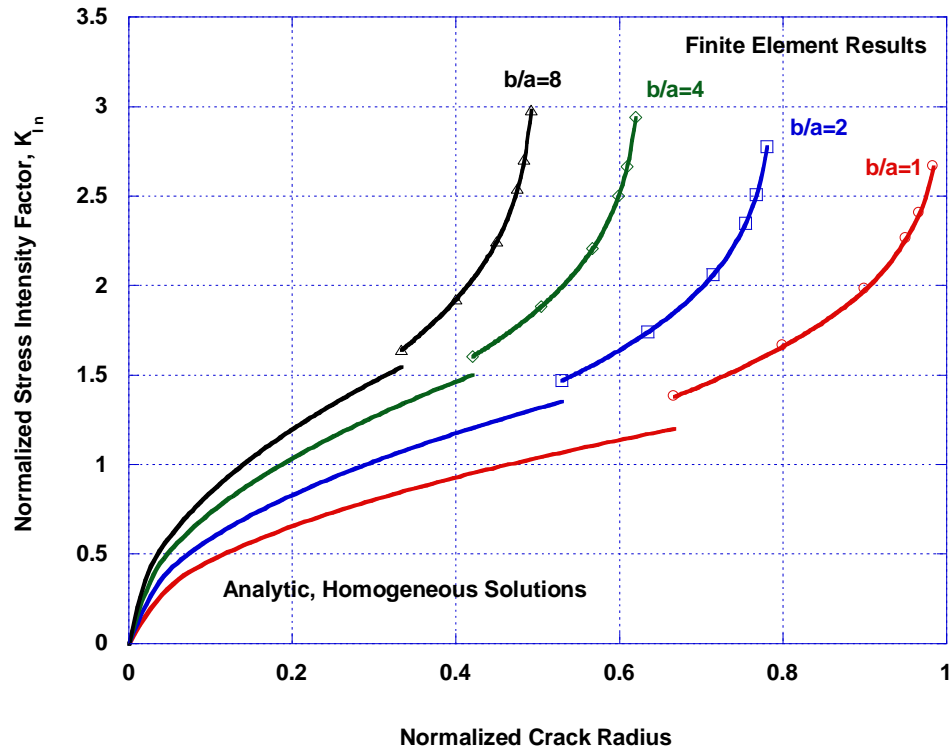
Figure 3.23   Normalized stress intensity factors for penny shaped cracks located at the centers of the particle cross sections for Ep/Em = 3 for aspect ratios of 1, 2, 4, and 8.
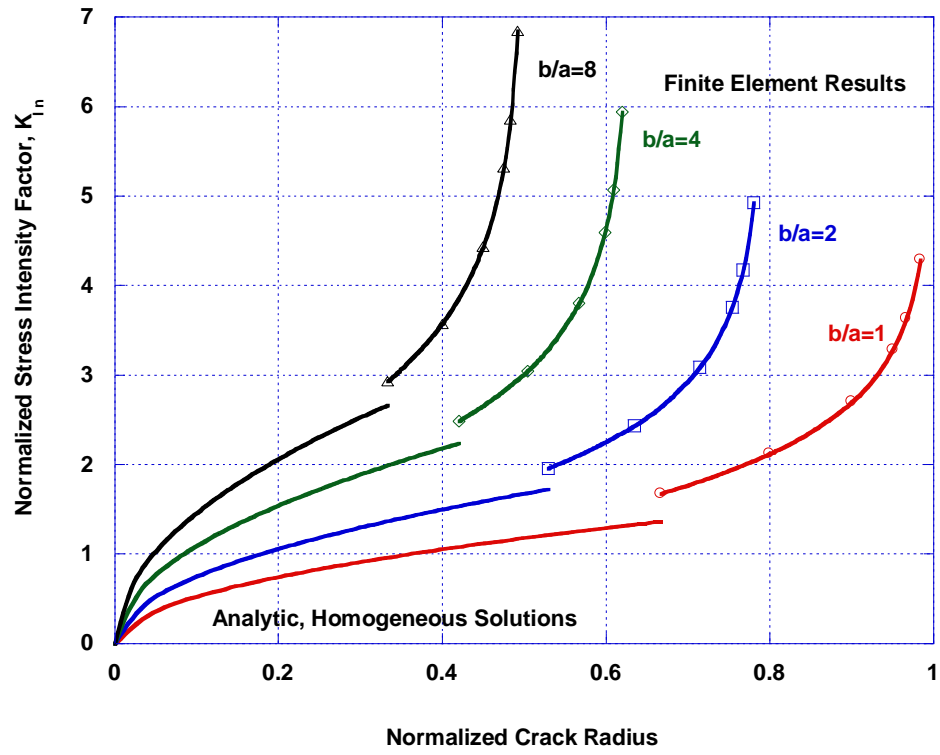
Figure 3.24   Normalized stress intensity factors for penny shaped cracks located at the centers of the particle cross sections for Ep/Em = 6 for aspect ratios of 1, 2, 4, and 8.
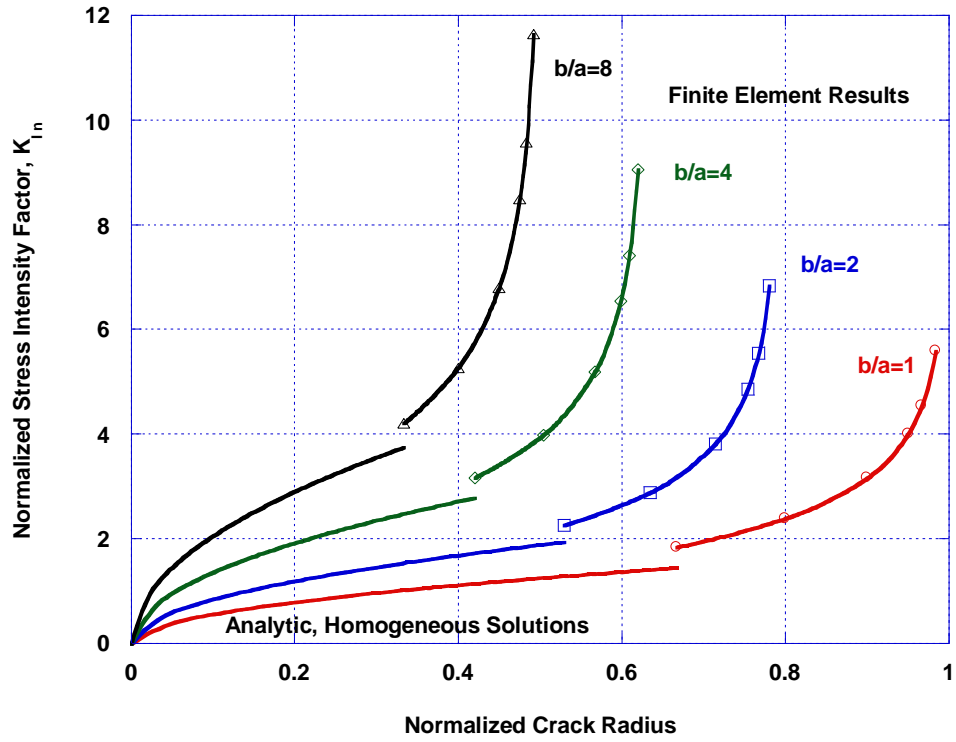
Figure 3.25   Normalized stress intensity factors for penny shaped cracks located at the centers of the particle cross sections for Ep/Em = 10 for aspect ratios of 1, 2, 4, and 8.
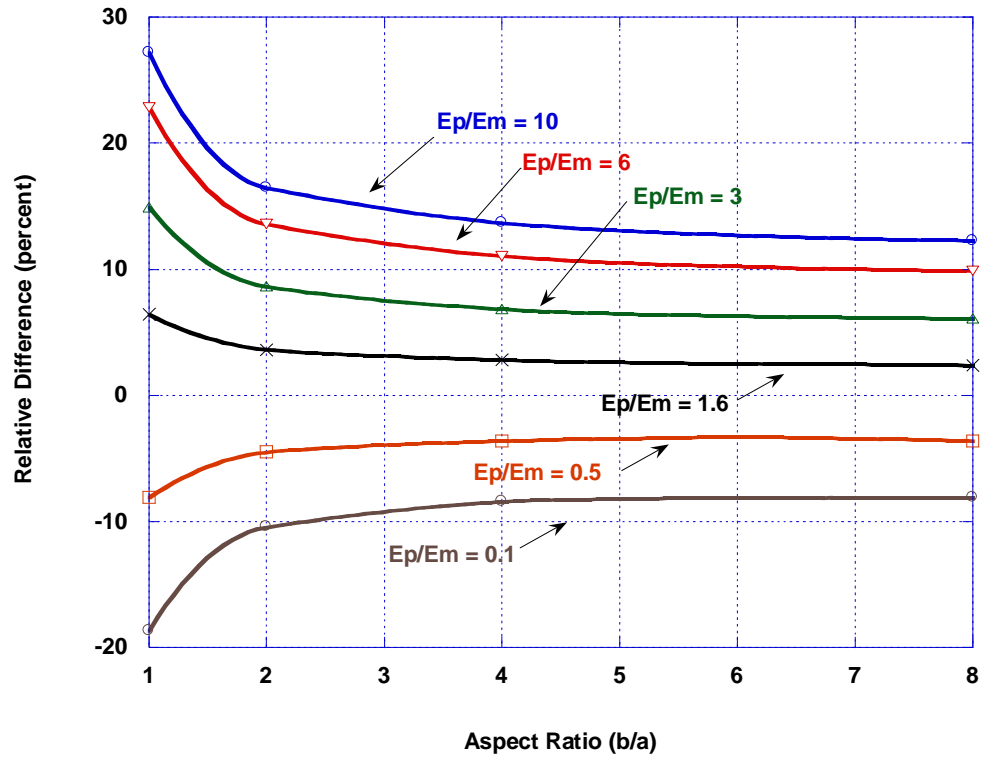
Figure 3.26   Relative difference between homogenous solutions and finite element predictions for penny shaped cracks located at the centers of particles for crack fronts located at r=2a/3, where a is the outer radius of the particle cross section.
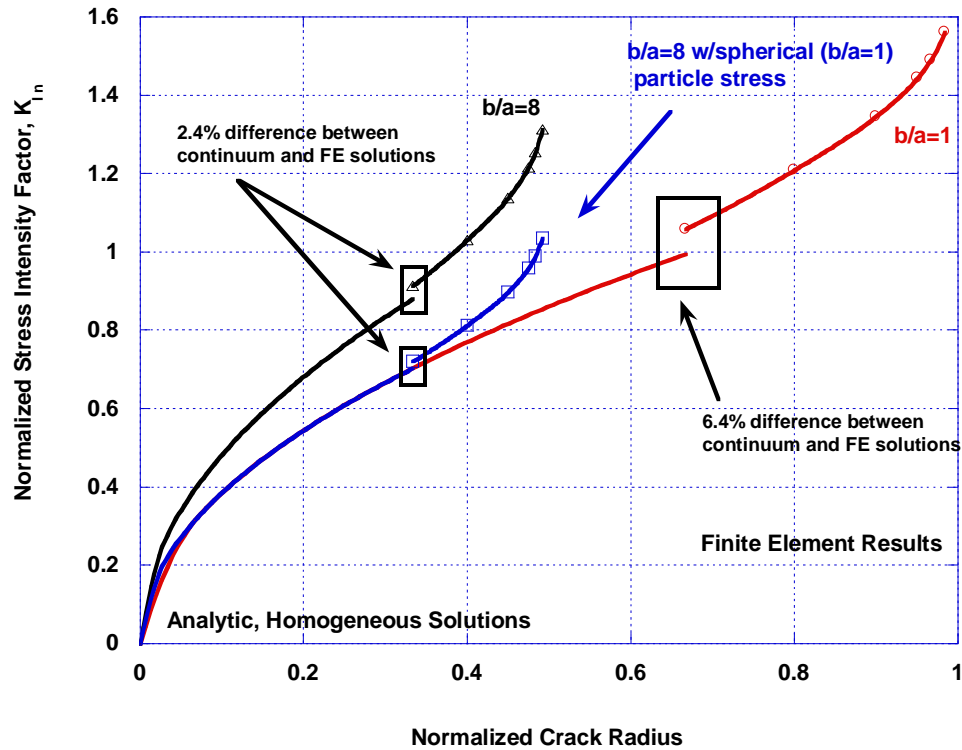
Figure 3.27   Normalized stress intensity factors for penny shaped cracks located at the centers of the particle cross sections for Ep/Em = 1.6 for aspect ratios of 1 and 8 with a curve added for the b/a = 8 particle subjected to the same stress as the spherical (b/a = 1) particle. The red and black curves for b/a = 1 and b/a = 8 are the same curves shown in Figure 3.22 and result from an applied far field strain of 0.001, which results in particle stresses of 12,185 psi for b/a = 1 and 15,452 for b/a = 8. The blue curve results from a reduced applied far field strain for the b/a = 8 prolate spheroid particle that resulted in a particle stress of 12,185 psi. Relative differences between the homogeneous and finite element solutions are indicated.
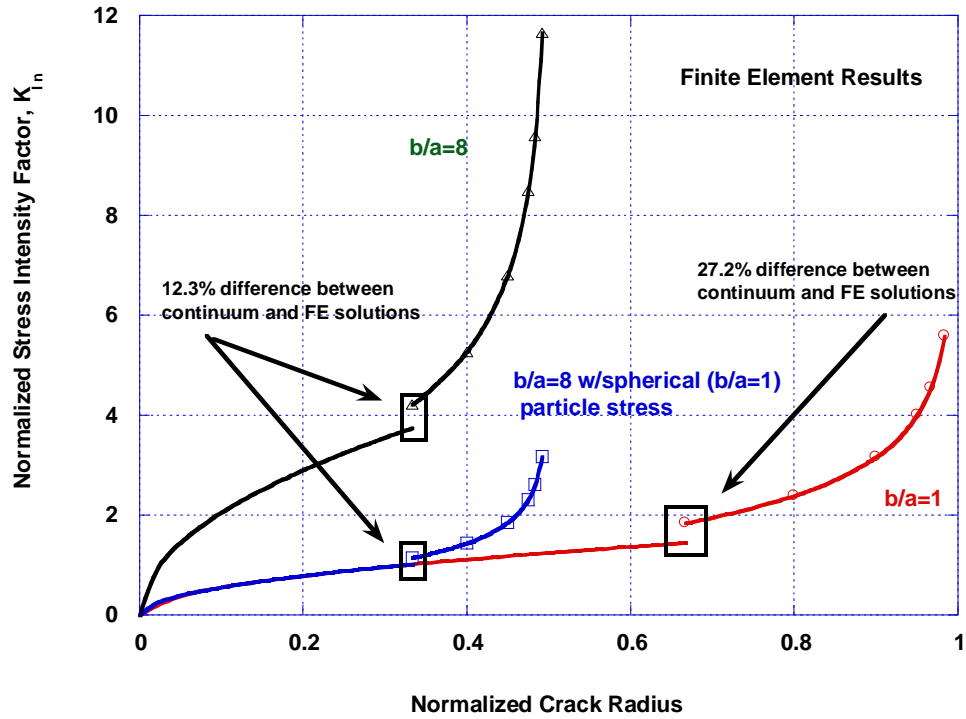
Figure 3.28   Normalized stress intensity factors for penny shaped cracks located at the centers of the particle cross sections for Ep/Em = 10 for aspect ratios of 1 and 8 with a curve added for the b/a = 8 particle subjected to the same stress as the spherical (b/a = 1) particle. The red and black curves for b/a = 1 and b/a = 8 are the same curves shown in Figure 3.25 and result from an applied far field strain of 0.001, which results in particle stresses of 17,685 psi for b/a = 1 and 64,922 psi for b/a = 8. The blue curve results from a reduced applied far field strain for the b/a = 8 prolate spheroid particle that resulted in a particle stress of 17,685 psi. Relative differences between the homogeneous and finite element solutions are indicated.

Ring shaped crack near interface
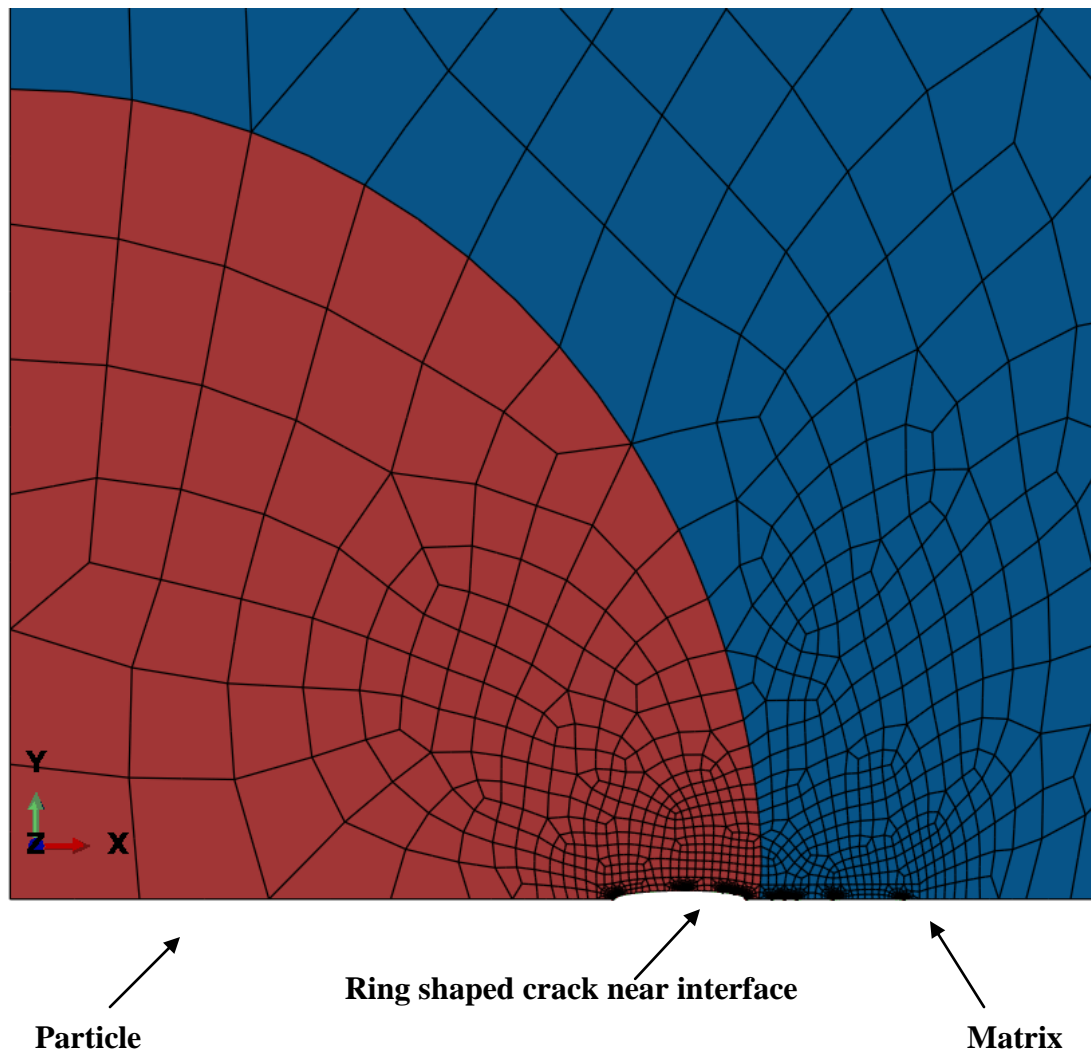
Particle

Matrix

Figure 3.29   A detail of an axi-symmetric finite element mesh for a model of a spherical particle with a ring shaped crack near the particle/matrix interface.   Deformed mesh with magnified displacements shown. Enlarged views showing the dimensions of the simulated cracks are shown in Figure 3.30.
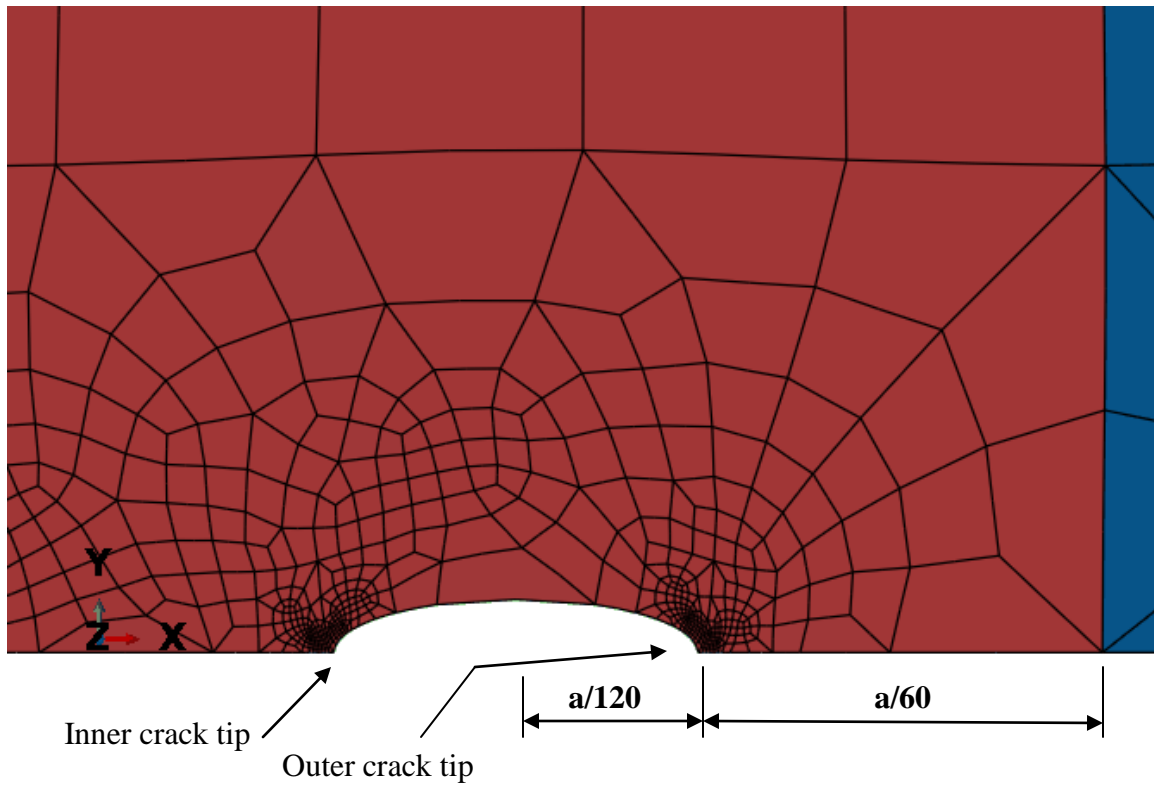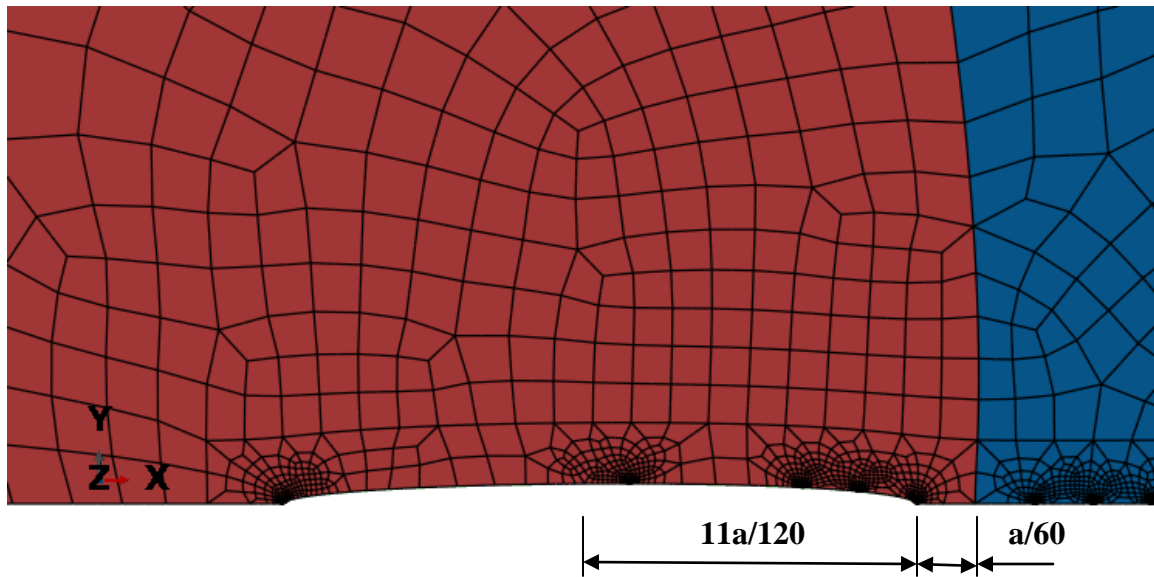
Figure 3.30   Details of small (a) and large (b) ring shaped cracks simulated near the interface of a spherical second phase particle.   Deformed mesh with magnified displacements shown.   Dimensions shown are in terms of the particle cross section radius, a.

Particle

Matrix

Ring shaped crack near interface
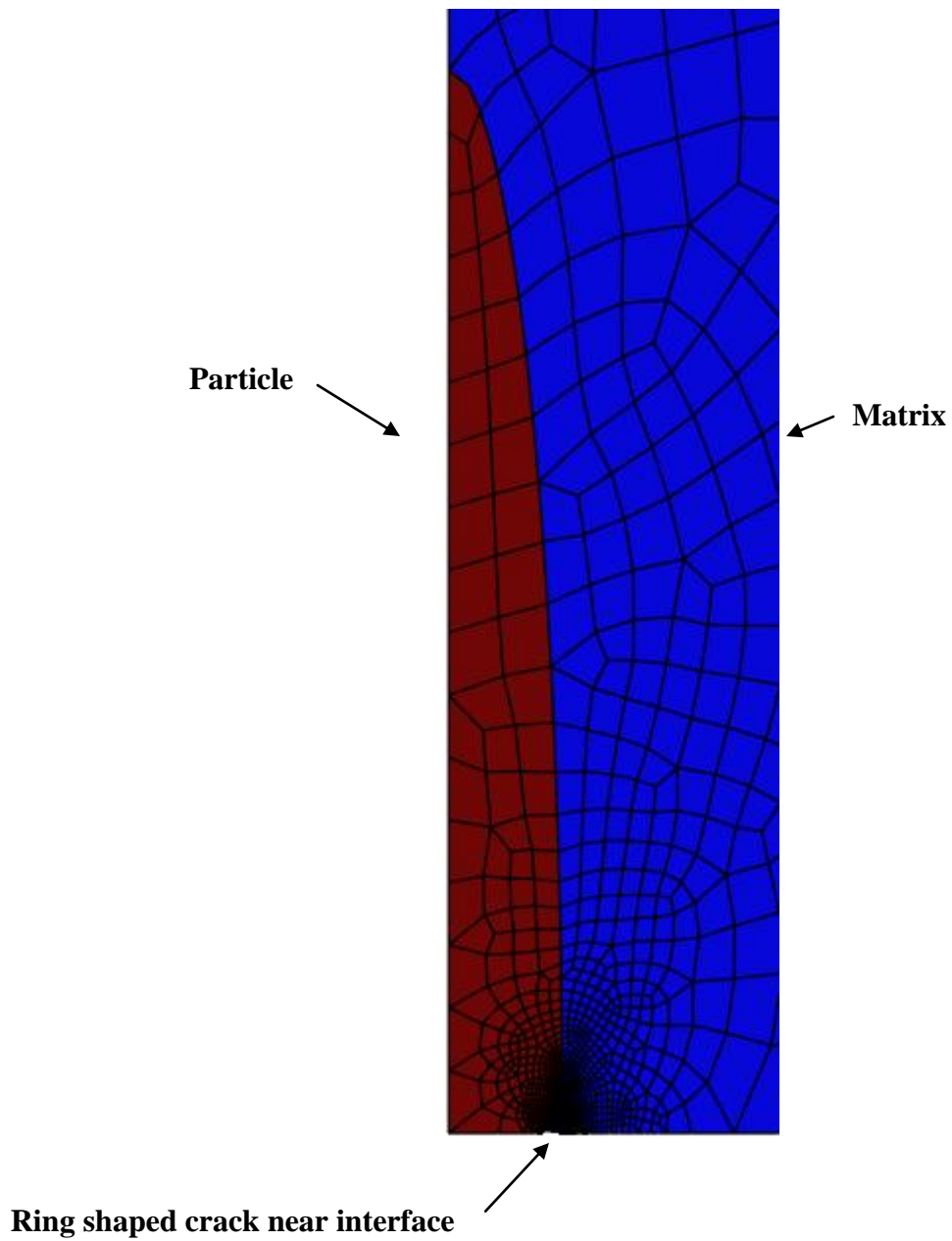
Figure 3.31   A detail of an axi-symmetric finite element mesh for a model of a prolate spheroid particle with an aspect ratio of b/a = 8 with a ring shaped crack near the particle/matrix interface.   Deformed mesh with magnified displacements shown.   Enlarged views showing the dimensions of the simulated cracks are shown in Figure 3.32.
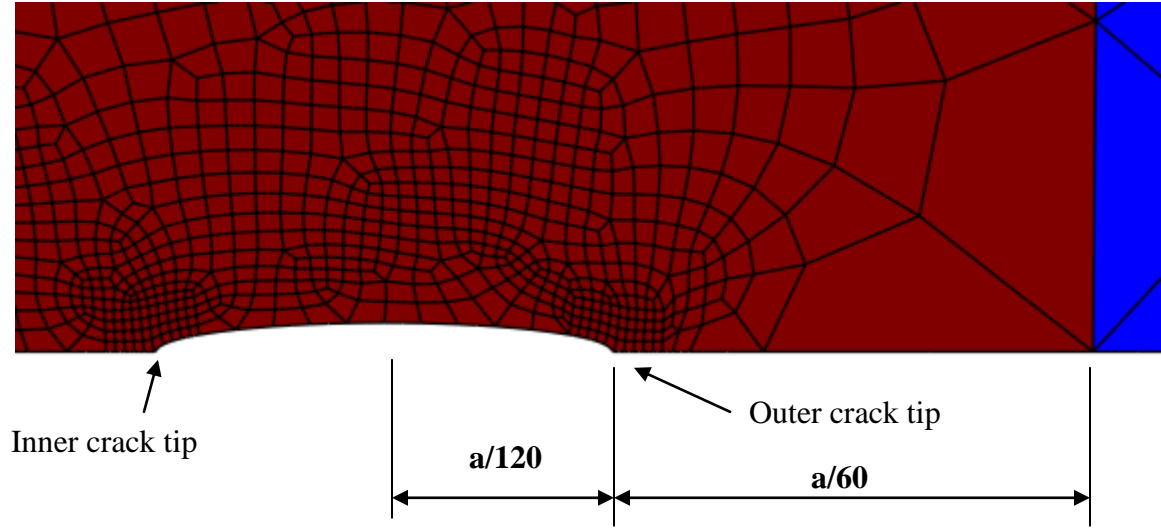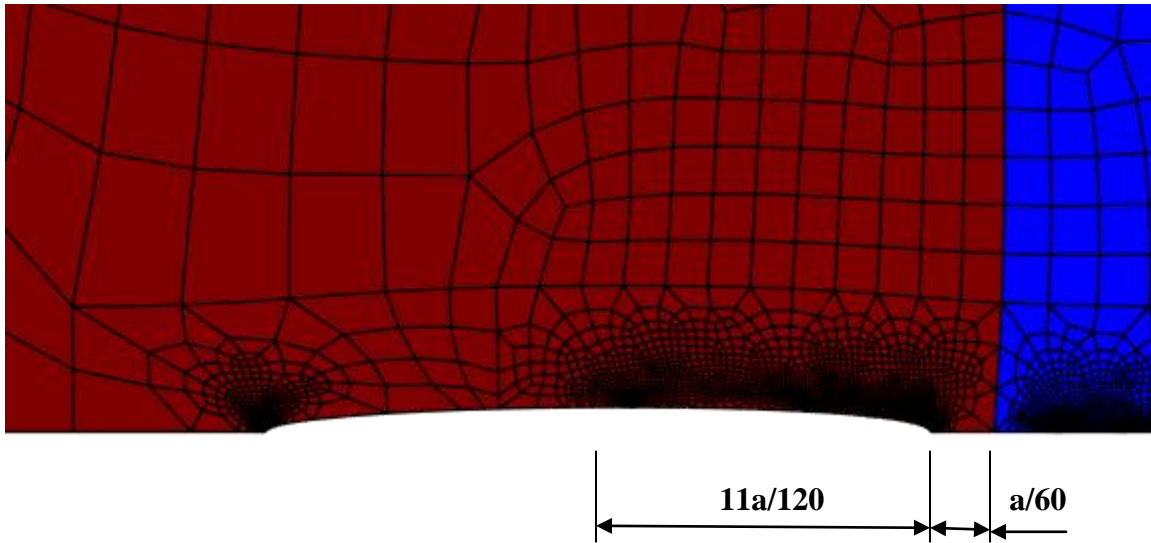
Figure 3.32   A details of the small ring crack (a) and large ring crack (b) simulated in a prolate spheroid second phase particle with an aspect ratio of b/a = 8. Deformed meshes with magnified displacements shown. Dimensions shown are in terms of the particle cross section radius, a.
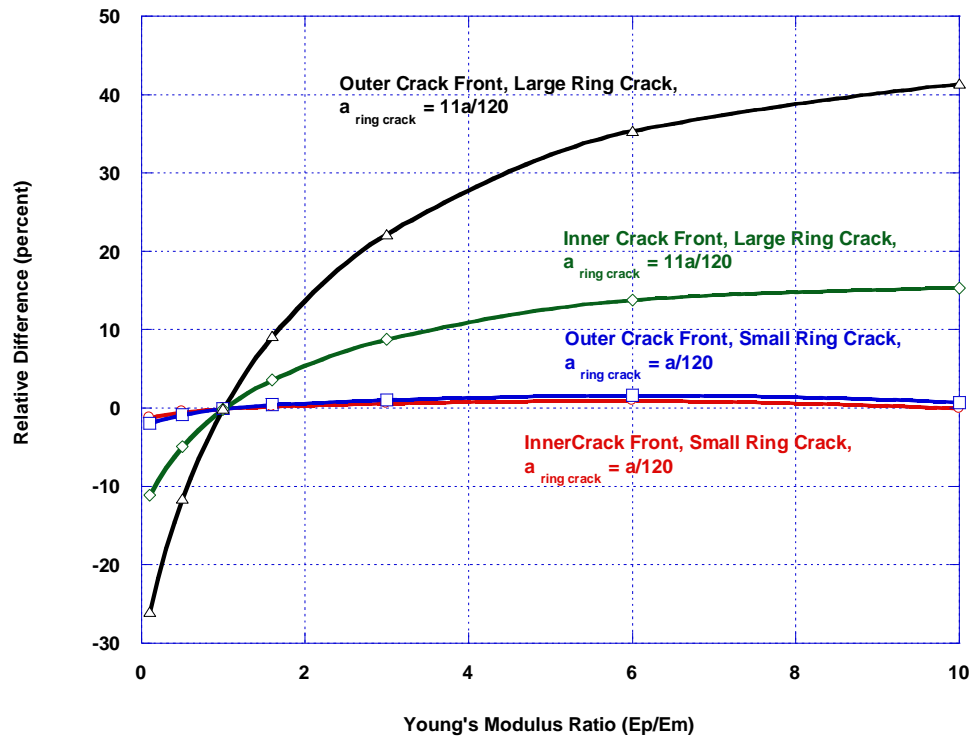
Figure 3.33   Relative differences between finite element predictions of stress intensity factors for ring cracks in second phase spherical particles in an aluminum matrix and analytic, homogenous solutions of stress intensity factors for ring cracks in a continuum having the same constitutive properties as the respective particles.
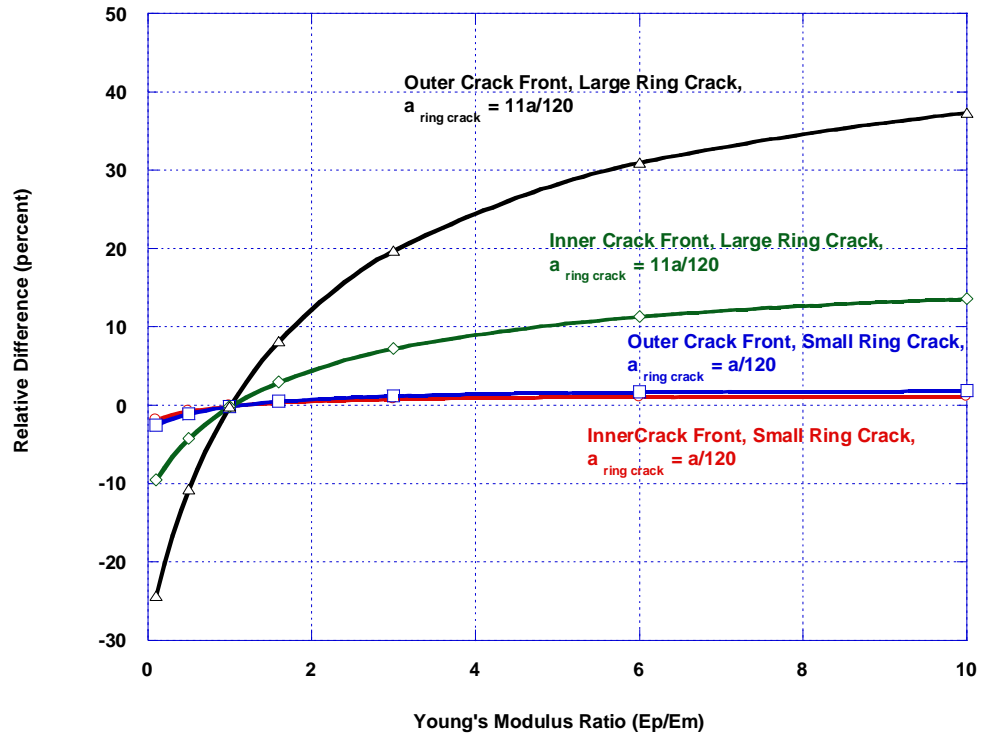
Figure 3.34   Relative differences between finite element predictions of stress intensity factors for ring cracks in second phase prolate spheroid particles with aspect ratios of b/a = 8 in an aluminum matrix and homogenous solutions of stress intensity factors for ring cracks in a continuum having the same constitutive properties as the respective particles.
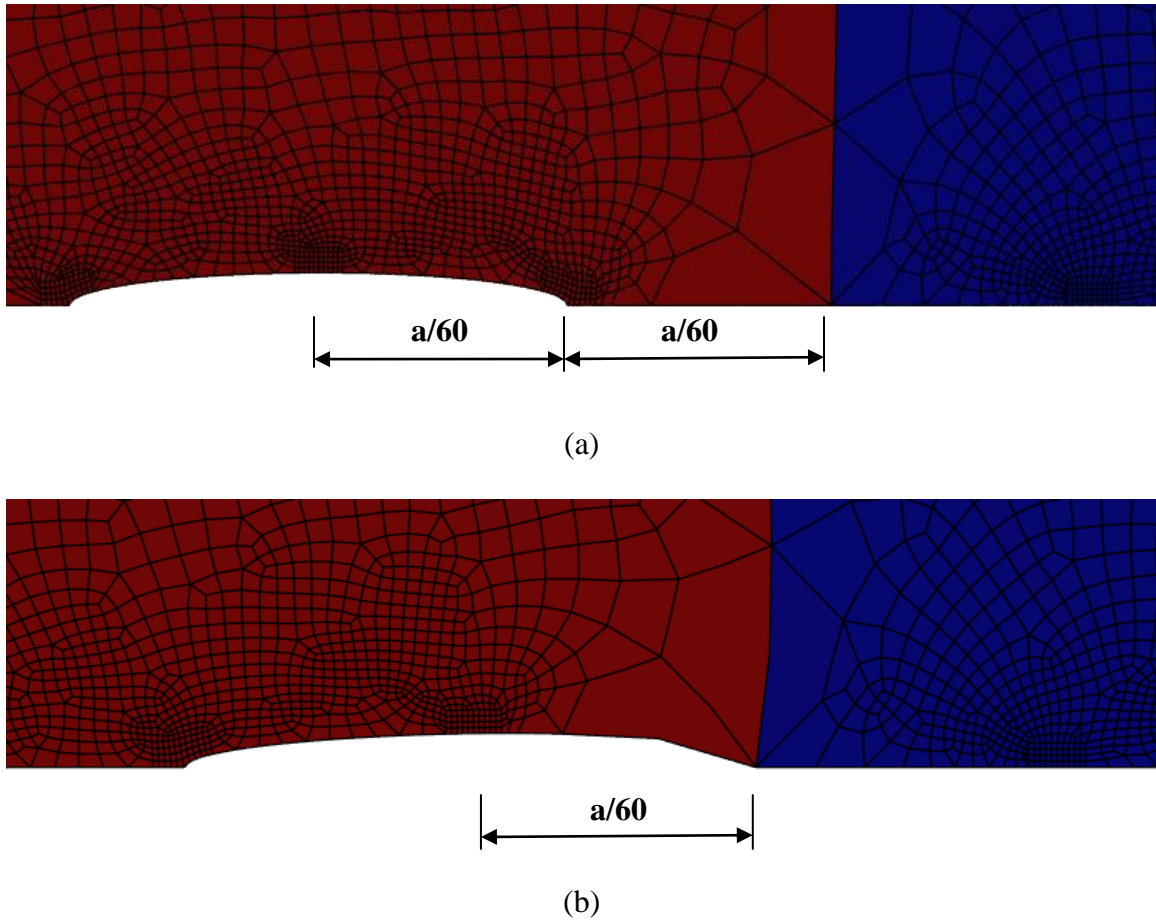
Figure 3.35   A details of ring cracks near (a) and touching the particle/matrix interface (b) simulated in a prolate spheroid second phase particle with an aspect ratio of b/a = 8. Deformed meshes with magnified displacements shown. Dimensions shown are in terms of the particle cross section radius, a.
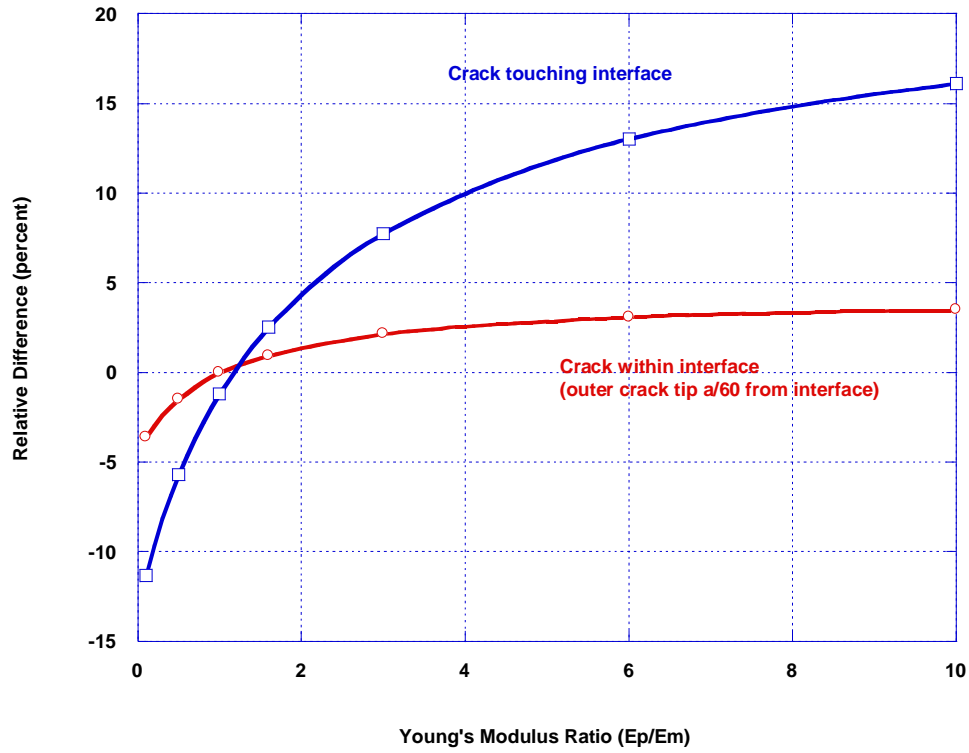
Figure 3.36   Relative differences between finite element predictions of stress intensity factors for the inner crack tips of ring cracks of length a/60 in second phase prolate spheroid particles with aspect ratios of b/a = 8 in an aluminum matrix and homogenous solutions of stress intensity factors for ring cracks in a continuum having the same constitutive properties as the respective particles. The curves shown correspond to a ring shaped crack inside the particle, a/60 from the interface (corresponding to Figure 3.35a) and a ring crack touching the particle/matrix interface (corresponding to Figure 3.35b).
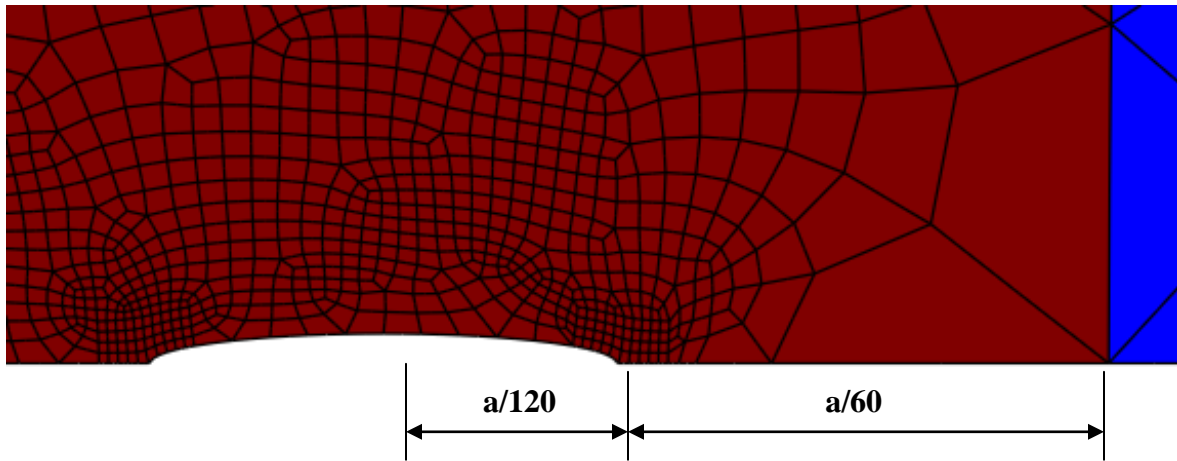
(a)
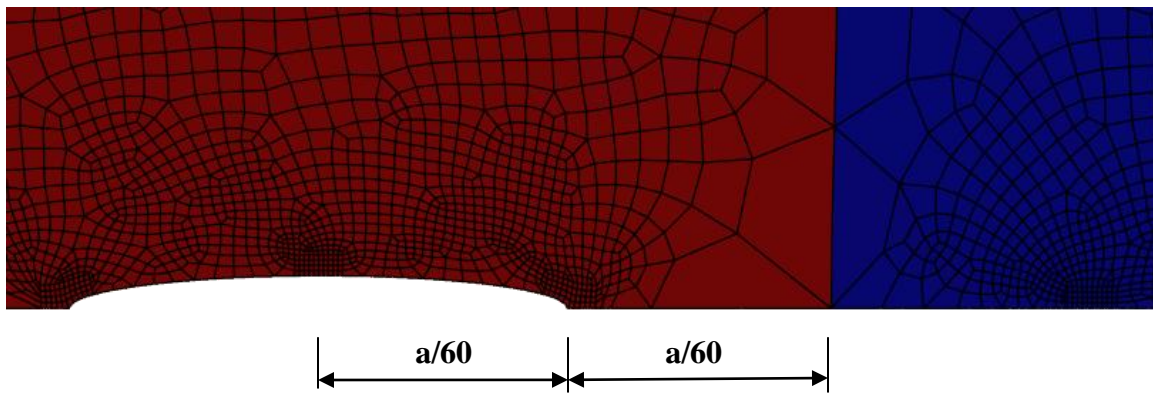
(b)

Figure 3.37   Details of the meshes for the ring shaped crack results shown in Figure 3.38. The mesh for a spherical particle is shown in (a) and the mesh for a prolate spheroid particle having aspect ratio of b/a = 8 is shown in (b). Because the radius of the particle cross section of the spherical particle is twice that of the prolate spheroid particle, the cracks shown are of the same length, in terms of absolute dimensions. The outer crack fronts of each are located at the same relative distance from the particle/matrix interface.
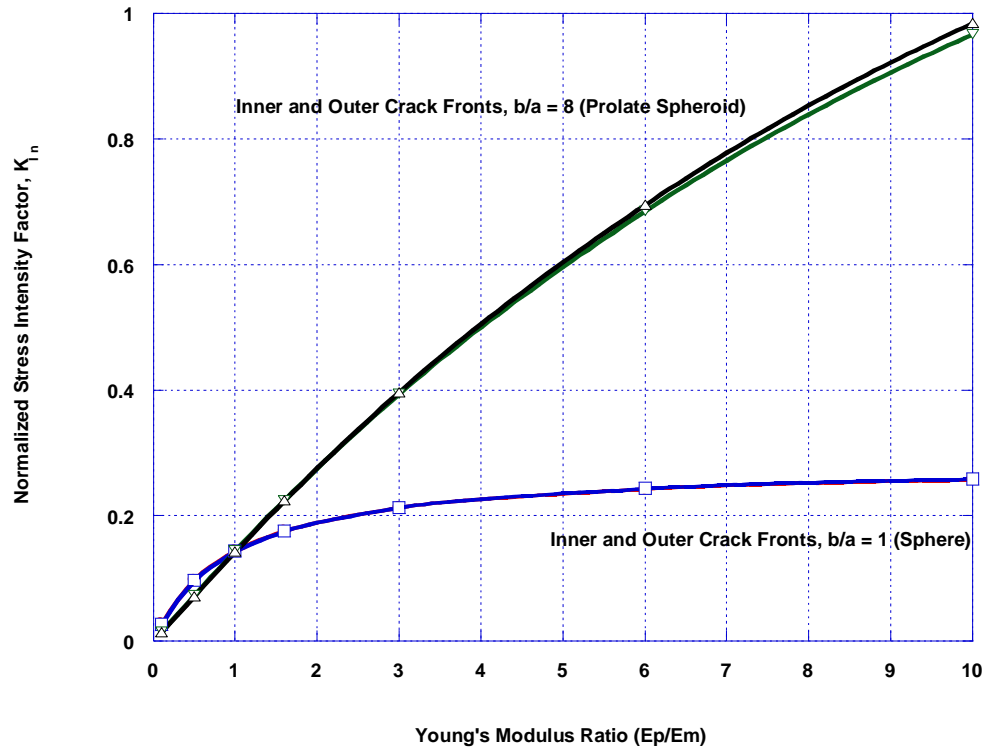
Figure 3.38   Comparison of normalized stress intensity factors for spherical (b/a = 1) and prolate spheroid (b/a = 8) second phase particles having the same absolute crack lengths with the outer crack fronts for both particles located a/60 from the particle matrix interface.
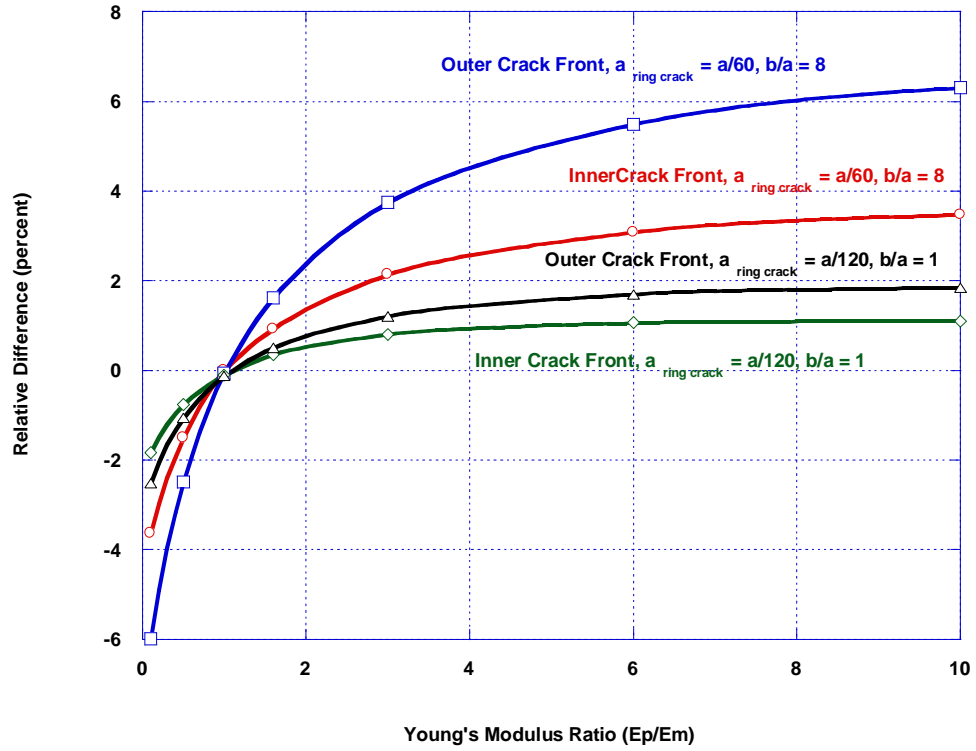
Figure 3.39   Relative differences between finite element predictions of stress intensity factors for ring cracks in second phase particles and homogeneous analytic solutions with the respective Eshelby Stresses applied for aspect ratios of 1 and 8 and with identical absolute crack lengths in each particle.
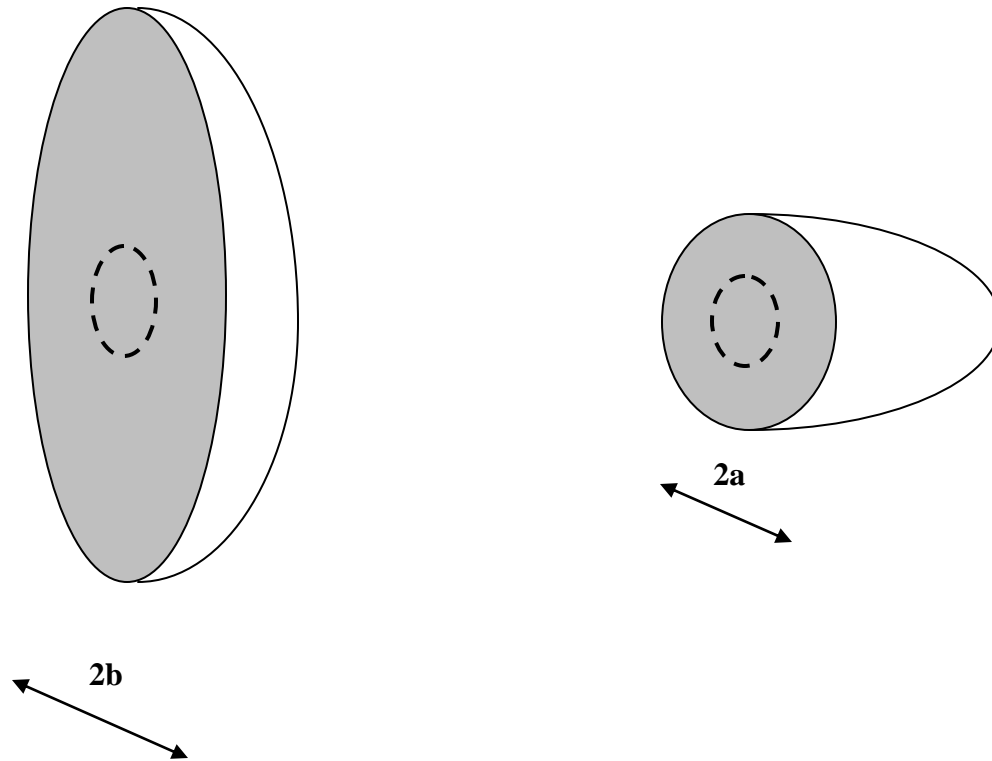
Figure 3.40   A diagram depicting a penny shaped crack at the center of the cross section of a particle with an elliptical cross section (left) and a penny shaped crack at the center of the cross section of a particle with a circular cross section (right).
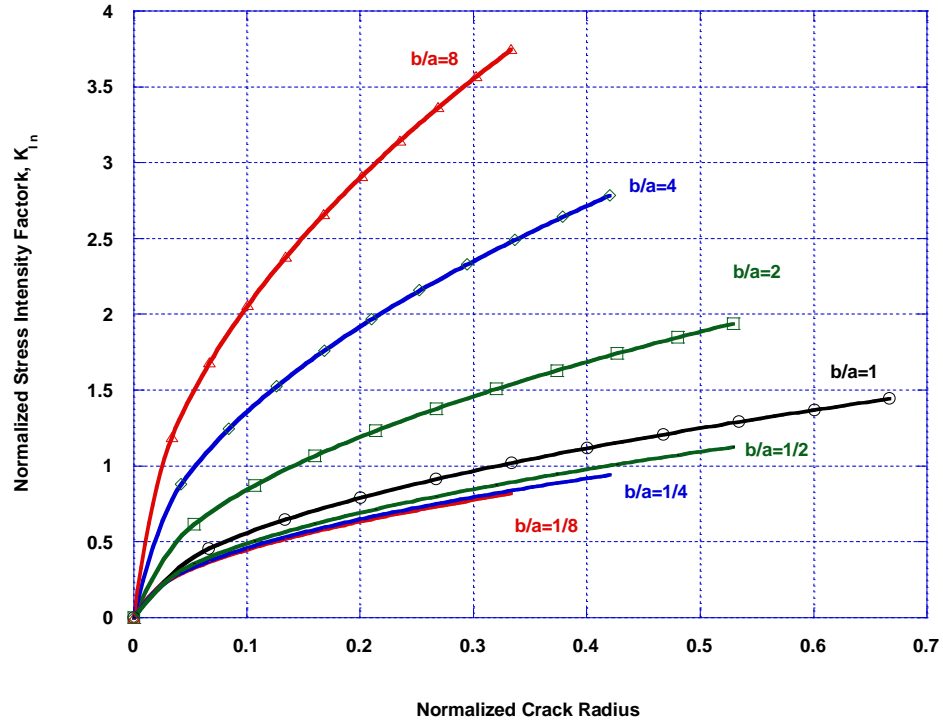
Figure 3.41   Stress intensity factors for penny shaped cracks located at the centers of particle cross sections for particle aspect ratios ranging from b/a = 1/8 to 8 with Ep/Em = 10. For particles with circular cross sections (b/a ≥ 1) the homogeneous penny shape crack solution is plotted to r = 2a/3 where a is the radius of the particle cross section. For particles with elliptical cross sections (b/a < 1) the homogeneous penny shape crack solution is plotted to r = 2b/3 where b is the minor dimension of the elliptical cross section.
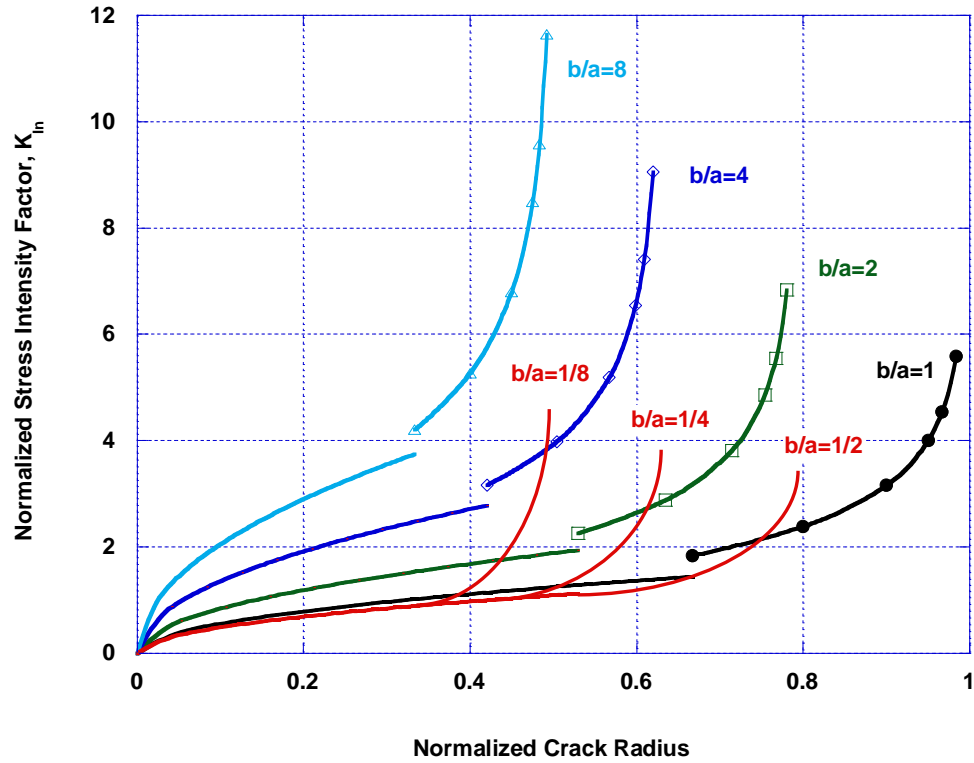
Figure 3.42   The penny shaped crack solutions of Figure 3.41 shown again with curves added to show near interface behavior of the cracks. For aspect ratios of 1 through 8, finite element solutions for stress intensity factor near the interface are plotted. For aspect ratios less than 1, curves depicting the asymptotic behavior of stress intensity factor near the interface are sketched in red.
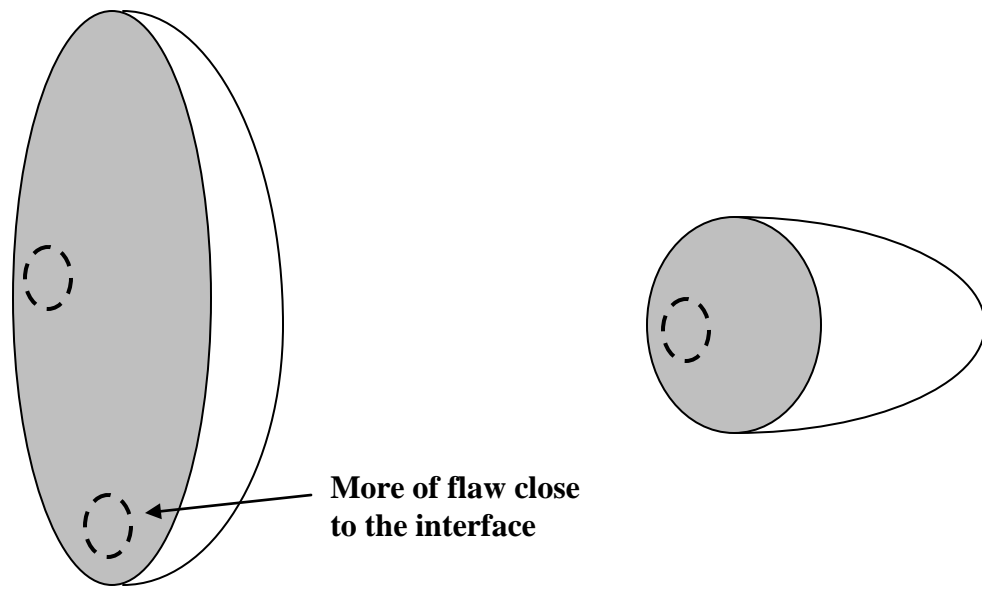
Figure 3.43   A diagram depicting flaws near the interface for a particle with an elliptical cross section (left) and with a circular cross section (right).

Chapter 4

Factors Controlling the Onset of Matrix Crack Propagation

4.1 CHAPTER INTRODUCTION

In Chapter 4, the onset of crack propagation into the matrix, following the particle fracture event, is considered as a function of particle shape and Young's modulus mismatch. Once a particle has fractured, it will act as a pre-existing crack in the matrix which, with additional applied strain, will serve as the initiation site for further crack propagation into the matrix. Unlike the Chapter 3 analysis, where the details of the initial flaws were not known, the initial flaw geometry is known for the problem of crack propagation from a fractured particle and corresponds to the cross section of the fractured particle. This allows for a more direct comparison of the crack propagation problem among a range of particle shapes. While crack propagation through the ductile matrix is an elastic-plastic problem, the onset of propagation can be considered with an elastic approach because crack propagation will first occur at the point along the crack front with the largest stress intensity factor. In Chapter 4, the likelihood of crack propagation into the matrix is considered for a series of ellipsoidal particles having constant volume by comparison of stress intensity factors along the crack fronts that would result from the fracture of those particles. For this analysis the particle cross sections are assumed to be fully cracked. In Chapter 4, the particle shapes used in Chapter 3 for the constant particle volume (CPV) cases are used for the evaluation of the onset of matrix crack propagation. The GALVALUME^R system (silicon particles in an aluminum coating matrix) is again

used as a model system. The analysis is then extended to consider a wide range of Young's modulus mismatch between the particles and matrix.

4.2 BEHAVIOR OF A CRACK IN A STIFF MATERIAL APPROACHING AN INTERFACE WITH A COMPLIANT MATERIAL

Through cracking of a particle in a ductile matrix creates a pre-existing crack that then serves as the initiation site for further crack propagation into the matrix and the onset of crack propagation depends on the magnitude of the stress intensity factor on the crack front that results from particle fracture. The results of Chapter 3 showed that, for a crack in a stiff material approaching an interface with a compliant material the stress intensity factor will become infinite at the interface. As a result, the crack is likely to pop through the interface into the more compliant material of the matrix. For cases where a particle is more compliant than the matrix, the results of Chapter 3 showed that the stress intensity factor will go to zero at the interface. This suggests that, for such cases, cracks in particles will arrest before reaching the interface. However, further crack propagation may occur with the application of additional strain. As such, cases where particles are more compliant than the matrix were included in the Chapter 4 analysis.

4.3 ESTIMATION OF STRESS INTENSITY FACTORS FOR $b/a \geq 1$

For aspect ratios greater than or equal to one, particle fracture will result in a circular crack front. This geometry allows for the simulation of stress intensity factors with two-dimensional axi-symmetric finite element models. For a particle stiffer than the coating matrix the problem must be considered for a crack front extending some finite distance

beyond the particle/matrix interface, due to the singular behavior of the stress intensity factor near the interface. Since the choice of the distance to extend the crack was not clear, finite element simulations were conducted for a series of crack fronts extending beyond the interface at the following increments: a/60, a/30, a/20, a/10, a/5, and a/3, where a is the particle half-height or crack radius. This was done using the same finite element models used for the Chapter 3 analysis. Simulations were conducted for the same ratios of Young's modulus mismatch between the particle and matrix used in Chapter 3 to show the effect of the mismatch on the onset of matrix crack propagation. Cases where particles were more compliant matrix were also considered for comparison, using the same approach.

Finite element results for cracks extending beyond the particle/matrix interface are shown in Figures 4.1 through 4.6. The Chapter 3 results for penny shaped cracks within the particle/matrix interface are also included in the plots. As in the Chapter 3 analysis, the results are normalized with respect to the homogeneous solution for a penny shaped crack in an aluminum continuum having a crack size equal to the cross section of the spherical particle from the range of constant volume particles considered.

For the first case, a particle/matrix Young's modulus ratio of 0.1, shown in Figure 4.1 the lowest stress intensity factors past the interface result for the particle with an aspect ratio of 8, a long, thin particle aligned with the loading direction. This particle has both the lowest stress and results in the smallest crack in the matrix. These effects combine to result in the lowest potential for crack propagation for the aspect ratios shown. As aspect ratio reduces, the particle stresses increase and the sizes of the cracks in the matrix increase. As a result, the potential for crack propagation into the matrix increases as

aspect ratio decreases from 8 to 1. For the four aspect ratios shown, the spherical particle is most prone to crack propagation into the matrix. As the crack fronts for the respective particles extend further from the interface, the stress intensity factors approach the homogenous solutions for penny shaped cracks in the matrix.

For the case of a Young's modulus ratio of 0.5, shown in Figure 4.2, the trends are similar to those shown in 4.1 but the stress intensity factors for crack fronts in the matrix are higher near the particle/matrix interface because the particle stresses are higher.

For a Young's modulus ratio of 1.6, Figure 4.3, the particles are stiffer than the matrix and the particle stresses are higher than the matrix stress. For particles stiffer than the matrix, particle stress increases as aspect ratio increases from 1 to 8. Stress intensity factors for cracks in the matrix remain lowest for an aspect ratio of 8 because the effect of the smaller crack size is more significant than the effect of the higher particle stress. For this case, the potential for propagation into the matrix, among the four particle shapes, is also highest for the spherical particle, due to the larger crack sizes for this particle.

For a Young's modulus ratio of 3, Figure 4.4, stress intensity factors in the matrix are similar near the interface but are highest for an aspect ratio of 8 and lowest for an aspect ratio of 1. This is because the effect of increased particle stress with increased Young's modulus ratio is beginning to dominate over the effect of smaller crack sizes that result for longer, thinner prolate spheroid shaped particles.

This effect continues and becomes more pronounced for Young's modulus ratios of 6 and 10, Figures 4.5 and 4.6, because of the increasing particle stress for particles having higher aspect ratios. Despite having smaller crack sizes, longer, thinner prolate spheroids

become most prone to matrix crack propagation for higher ratios of Young's modulus mismatch, due to increasing particle stresses with increasing Young's modulus ratio.

4.4 ESTIMATION OF STRESS INTENSITY FACTORS FOR $\frac{b}{a} < 1$

For aspect ratios less than one, particle fracture results in an elliptical crack front. Because the particle lacks axi-symmetry about the loading axis, two-dimensional axi-symmetric finite elements could not be used to simulate stress intensity factors. In principle, three-dimensional models could be used. However, the solution routines for the prediction of stress intensity factors available in the ABAQUS software require the use of six-sided brick elements on the crack front. The meshing of an ellipsoidal particle requires a rotation about the major axis of the elliptical cross-section. This will result in five-sided wedge elements at the tips of the major axis. For aspect ratios less than one the crack front coincides with the elliptical cross-section of the particle and, as a result, wedge elements at the tips of the major axis would be on the crack front. As a consequence, the ABAQUS routines for the prediction of stress intensity factors could not be used for particle aspect ratios less than one.

Because finite element simulations could not be used, an analytic solution to estimate stress intensity factors resulting from fractured particles was considered. Tada, et al. [32] give the maximum value of stress intensity factor along elliptical crack front as:

$$K_I = \frac{\sigma\sqrt{\pi b}}{E(k)} \ , \qquad \text{on the minor axis of the ellipse} \tag{4.1}$$

where, $E(k)$ is an elliptic integral: $E(k) = \int\limits_{0}^{\pi/2} \sqrt{1 - k^2 \sin^2 \varphi}\, d\varphi$

and b is the minor dimension of the ellipse.

Equation 4.1 was used to estimate stress intensity factors for elliptical crack fronts that would result from the fracture of ellipsoidal particles with aspect ratios less than one. The matrix stress was used in the calculation, meaning that the stress intensity factors calculated were simply for the homogeneous case of elliptical cracks in an aluminum continuum and that the effect of the particle was neglected. It was suspected that use of the homogenous solution for such particles would be reasonable because it was thought the effect of the particle on matrix crack propagation would become less significant for such particles due to reductions in particle stress for these shapes.

4.5 ONSET OF MATRIX CRACK PROPATAGATION FOR b/a = 1/8 TO b/a = 8

The onset of crack propagation into the coating matrix from cracks resulting from fractured particles was considered with a combination of the analytic solution for an elliptical crack in an aluminum continuum for aspect ratios less than one and finite element results for crack fronts extending beyond fractured particles for aspect ratios of one and higher. Because of the singular behavior of stress intensity factors for cracks near the interface for particles more stiff than the matrix, comparisons were made for crack fronts extending a finite distance into the matrix. For each particle aspect ratio case the crack front considered extended one tenth of the particle cross section dimension (b/10 for elliptical cross sections and a/10 for circular cross sections) beyond the location

of the particle matrix interface, as shown in Figure 4.7. This increment in crack length was chosen because, as shown in Figures 4.1 through 4.6, the singular behavior near the interface had largely dissipated but the effect of the particle on stress intensity factor was still evident.

Results were first considered for the homogeneous case of elliptical (b/a < 1) and penny-shaped (b/a = 1 to 8) cracks in aluminum. Results for fractured silicon particles, corresponding to the model GALVALUME^R system, were then added. Next, the analysis was expanded to consider a wide range in Young's modulus mismatch between the particle and coating matrix.

Figure 4.8 shows stress intensity factors for the homogenous case of cracks in aluminum with crack fronts extended a/10 (for b/a ≥ 1) and b/10 (for b/a < 1) beyond the location of the particle/matrix interface. The maximum value of occurs for the crack front corresponding to an ellipsoidal particle with b/a = 1/4, with the value for b/a = 1/2 being nearly as high. Figure 4.9 shows the homogeneous results of Figure 4.8 along with finite element results for cracks extended beyond the particle/matrix interface for silicon particles in aluminum (Ep/Em = 1.6) for aspect ratios ranging from b/a =1 to b/a = 8. As the aspect ratio reduces from 8 to 1 the results for the silicon particle case approach the homogeneous results, suggesting the homogeneous elliptical crack solution provides a good estimate for the consideration of crack propagation from fractured ellipsoidal silicon particles having aspect ratios less than 1.

Considering the homogeneous results for b/a = 1/8 to 1/2 along with the finite element results for fractured silicon particles for b/a = 1 to 8, the same maximum values from Figure 4.8 remain. Because solutions for elliptical cracks in aluminum are used for

111

aspect ratios less than one, these results provide lower bound estimates of the stress intensity factors. The stress intensity factors resulting from fractured silicon particles with these aspect ratios will be somewhat higher, due to higher stresses in the particles, while the finite element results for aspect ratios of 1 and greater are all less than the homogeneous elliptical crack estimates. Thus, Figure 4.9 clearly indicates that crack propagation into the coating matrix from fractured silicon particles will first occur for b/a = 1/4, with the potential for matrix crack propagation for b/a = 1/2 being similar. The predicted stress intensity factor was lowest for b/a = 8, making this shape the most favorable for limiting crack propagation from fractured silicon particles, generally indicating that long, thin silicon particles aligned with the loading direction offer the best resistance to crack propagation into matrix from fractured particles for the silicon particle/aluminum matrix system.

The Chapter 3 results for the crack initiation problem showed that, for similar initial flaws that are small with respect to the particle cross section, Figures 3.13 and 3.22, a particle with an aspect ratio of 8 is most prone to fracture, for the silicon particle/aluminum matrix system, although this ranking could change with increasing initial flaw size. For this same material combination, Figure 4.9 shows that the particle with the aspect ratio of 8, once fractured, will be the least prone to result in crack propagation into the matrix. So, in this case the worst particle shape for particle fracture (the crack initiation problem) is also the best particle shape for avoiding crack propagation. This specific case illustrates the complex behavior occurring with particle fracture and with crack propagation from fractured particles.

112

The results of Figures 4.8 and 4.9 are shown again in Figure 4.10 with additional curves for Young's modulus ratios ranging from 0.1 to 10. Figure 4.10 shows a progressively stronger effect of Young's modulus mismatch on stress intensity factor as aspect ratio increases from 1 to 8, with minimum and maximum values occurring for b/a = 8 for Ep/Em values of 0.1 and 10 respectively. The curves for the respective Young's modulus ratios become closer together as aspect ratio reduces from 8 to 1, further suggesting that the homogenous cases of elliptical cracks in aluminum provide reasonable estimates for cracks resulting from fractured particles for aspect ratios less than 1.

The relationship between the stress intensity factor curves in Figure 4.10 is primarily the result of the change in particle stress with Young's modulus mismatch, shown in Figure 3.13 for aspect ratios ranging from 1/8 to 8. The lengthening of the particles, as aspect ratio increases, results in higher levels of stress transfer to the particles for higher Young's modulus ratios, leading to higher values of stress intensity factor and increased potential for crack propagation into the coating matrix from fractured particles.

The analysis was considered on the basis of particles having constant volume. Meaning the spherical particles would result in the largest cracks in the matrix. And, when the homogenous case is considered, elliptical crack faces corresponding to the constant volume particle sizes for aspect ratios less than one result in the highest stress intensity factors. The effect of Young's modulus mismatch is very significant and can result in crack face shapes least prone to crack propagation in a homogeneous system, corresponding long thin prolate spheroids aligned with the loading direction, becoming most prone to propagation as Young's modulus mismatch increases.

For the case of a Young's modulus ratio of 3 in Figure 4.10 the stress intensity factors are nearly uniform for aspect ratios ranging from 1 to 8. The estimated value for an aspect ratio of 1/8 is about the same and the estimated values for aspect ratios of 1/2 and 1/4 are not significantly higher. If this case is considered from the standpoint of a particle reinforced composite material, an aspect ratio of 8 results in the highest stress transfer to the particle, and highest composite stiffness, but without a penalty of increased potential for matrix crack propagation in the event of particle fracture. If random particle orientation is considered, a particle aspect ratio of 1/8 corresponds to a 90 degree rotation with respect to the loading direction and the corresponding potential for matrix crack propagation remains roughly the same. Higher values of Young's modulus ratio offer the potential for higher composite stiffness, but with a potential penalty of increased likelihood of matrix crack propagation in event of particle fracture.

4.6 CONCLUSIONS

In Chapter 3, the fracture of ellipsoidal particles was investigated. In Chapter 4, this study was extended to consider the onset of crack propagation into the surrounding matrix from fully fractured particles. This was done by comparing stress intensity factors for cracks extending beyond the particle/matrix interface and into the matrix. The contribution of this work is to map out the relationship between particle shape, Young's modulus mismatch, and the onset of crack propagation and to specifically show that the onset of crack propagation is strongly dependent on the combined effects of the sizes of cracks that resulting from particle fracture and the Young's modulus mismatch between the particles and matrix. As the Young's modulus mismatch between the particles and

matrix increases, long, thin particles become most prone to crack propagation into the matrix. Such particles were also determined to be most prone to fracture for particles stiffer than the matrix, meaning that they represent the greatest potential for failure of the composite particle/matrix system when particles are much stiffer than the matrix.

Figure 4.1   Normalized stress intensity factors for cracks within and beyond the particle/matrix interface for ellipsoidal particles with aspect ratios of 1, 2, 4, and 8 for a Young's modulus ratio of Ep/Em = 0.1.

116
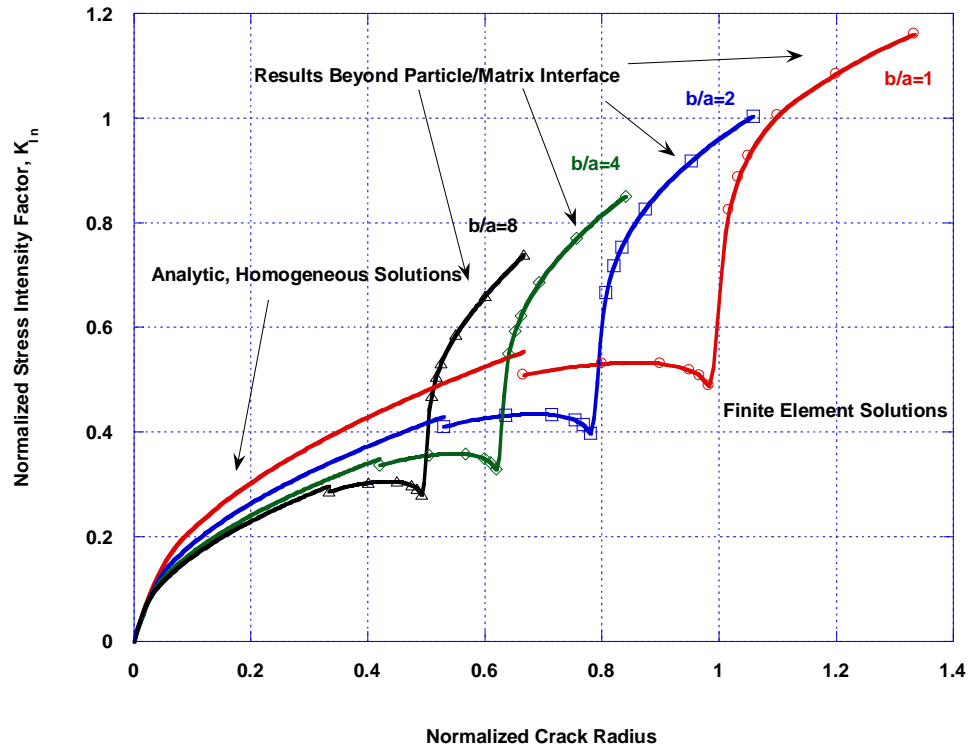
Figure 4.2   Normalized stress intensity factors for cracks within and beyond the particle/matrix interface for ellipsoidal particles with aspect ratios of 1, 2, 4, and 8 for a Young's modulus ratio of Ep/Em = 0.5.
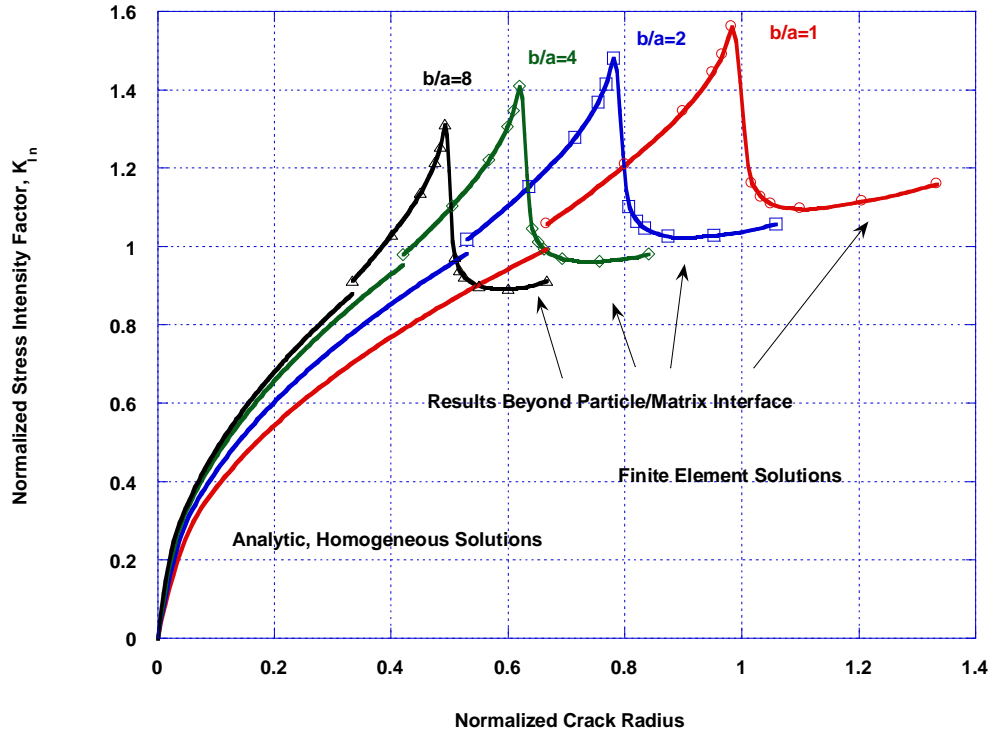
Figure 4.3   Normalized stress intensity factors for cracks within and beyond the particle/matrix interface for ellipsoidal particles with aspect ratios of 1, 2, 4, and 8 for a Young's modulus ratio of Ep/Em = 1.6.
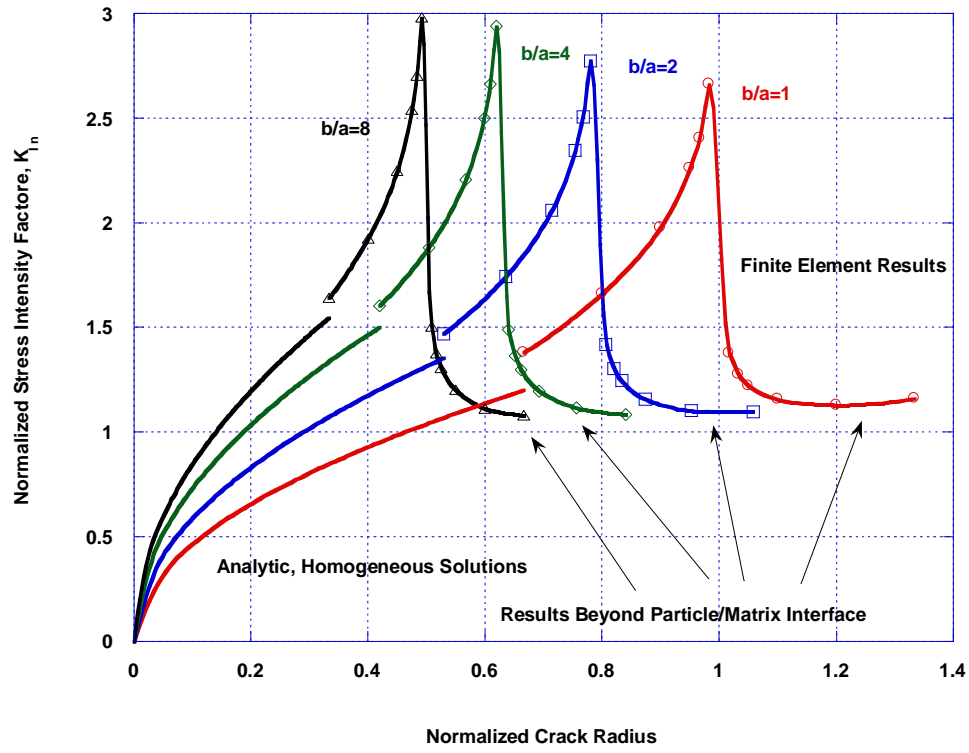
Figure 4.4 Normalized stress intensity factors for cracks within and beyond the particle/matrix interface for ellipsoidal particles with aspect ratios of 1, 2, 4, and 8 for a Young's modulus ratio of Ep/Em = 3.
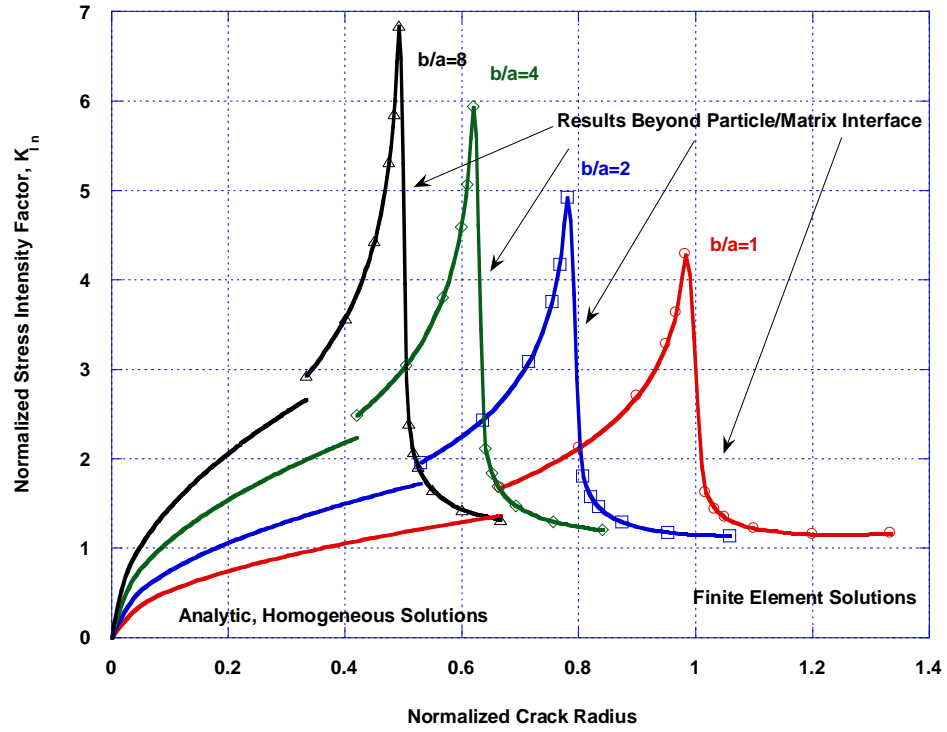
Figure 4.5   Normalized stress intensity factors for cracks within and beyond the particle/matrix interface for ellipsoidal particles with aspect ratios of 1, 2, 4, and 8 for a Young's modulus ratio of Ep/Em = 6.
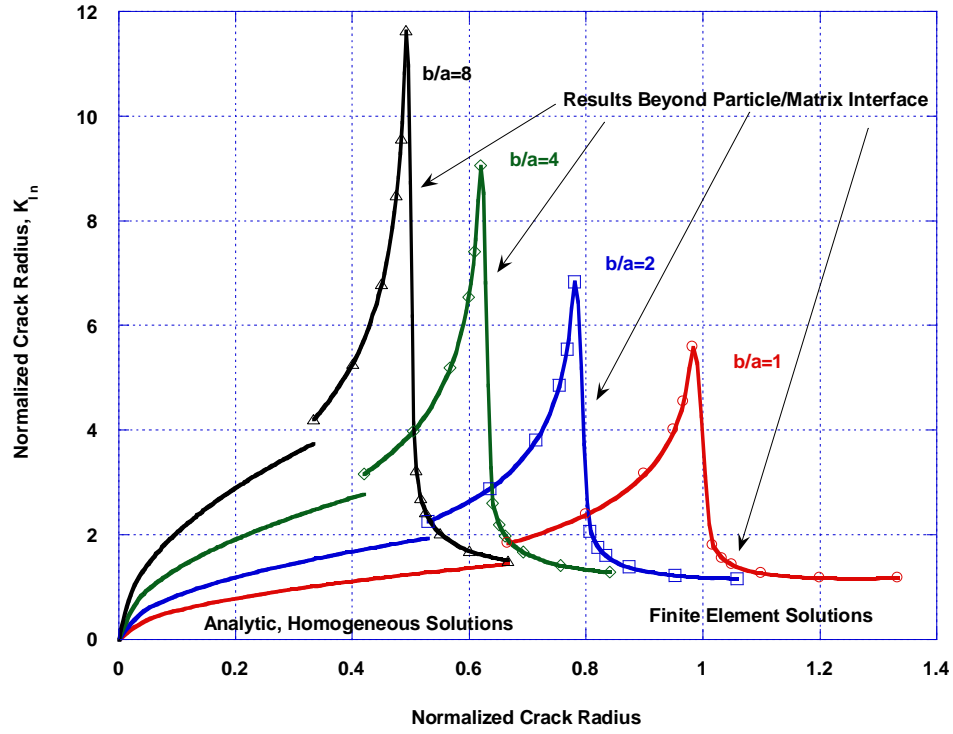
Figure 4.6   Normalized stress intensity factors for cracks within and beyond the particle/matrix interface for ellipsoidal particles with aspect ratios of 1, 2, 4, and 8 for a Young's modulus ratio of Ep/Em = 10.

$$\frac{b}{a} < 1$$

$$\frac{b}{a} \geq 1$$

Elliptical crack front

Circular crack front

One half of fractured particle

b/10

a/10

Crack fronts extending beyond interface into coating matrix
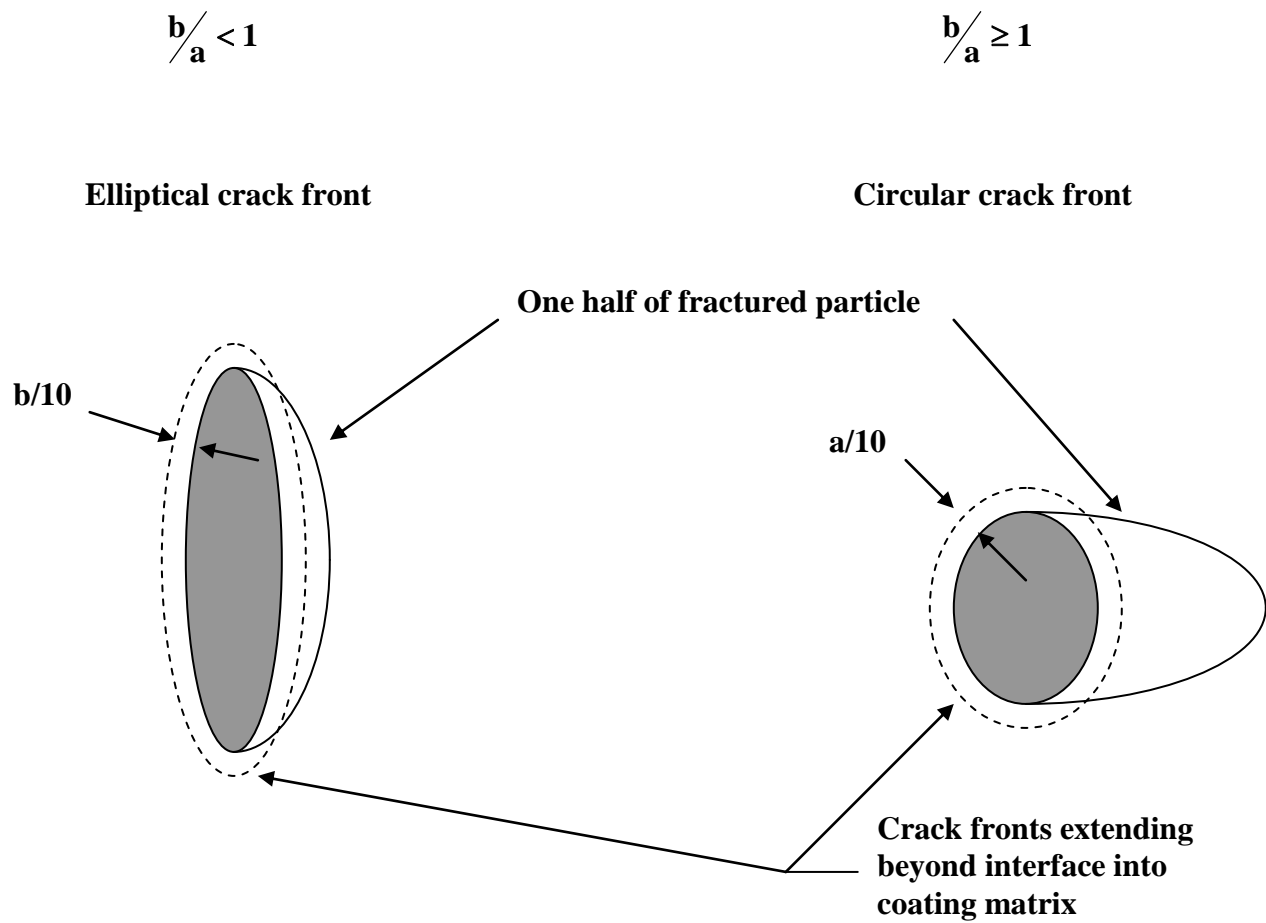
Figure 4.7   Schematic depicting crack fronts extending beyond the particle/matrix interface for particle aspect ratios less than 1 and greater than 1.
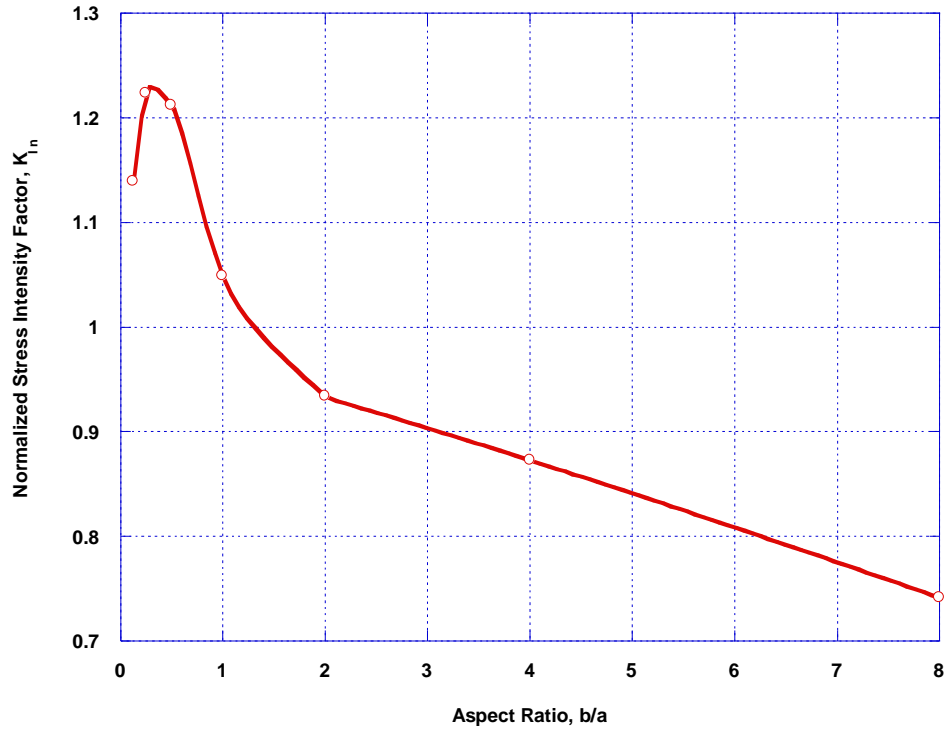
Figure 4.8   Normalized stress intensity factors for aspect ratios ranging from 1/8 to 8 for the homogeneous case of elliptical (b/a <1) and penny shaped (b/a ≥ 1) cracks corresponding to the constant volume particle sizes. In each case, the crack front is extended one tenth of the critical particle dimension (b/10 for elliptical crack faces and a/10 for circular crack faces) beyond the location of the particle/matrix interface.
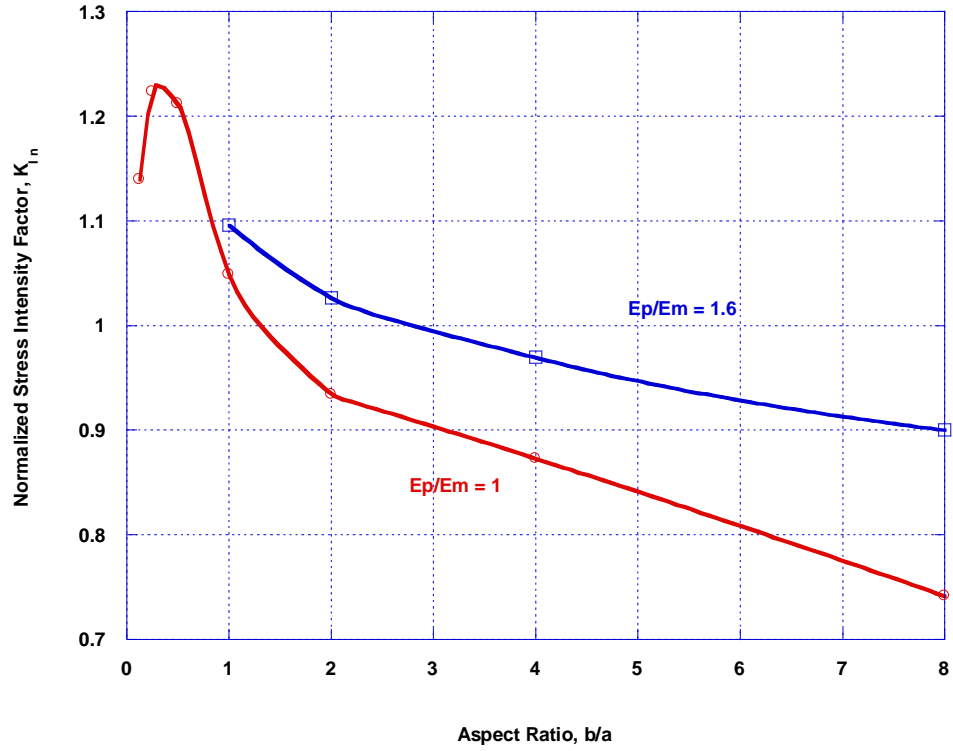
Figure 4.9   Normalized stress intensity factors for crack fronts extended beyond the particle/matrix interface for the homogeneous case (Ep/Em=1) and the case of a silicon particle in an aluminum matrix (Ep/Em=1.6).   For the homogeneous case analytic solutions for elliptical and penny-shaped cracks are shown.   For the silicon particle/aluminum matrix case, finite element predictions are shown.
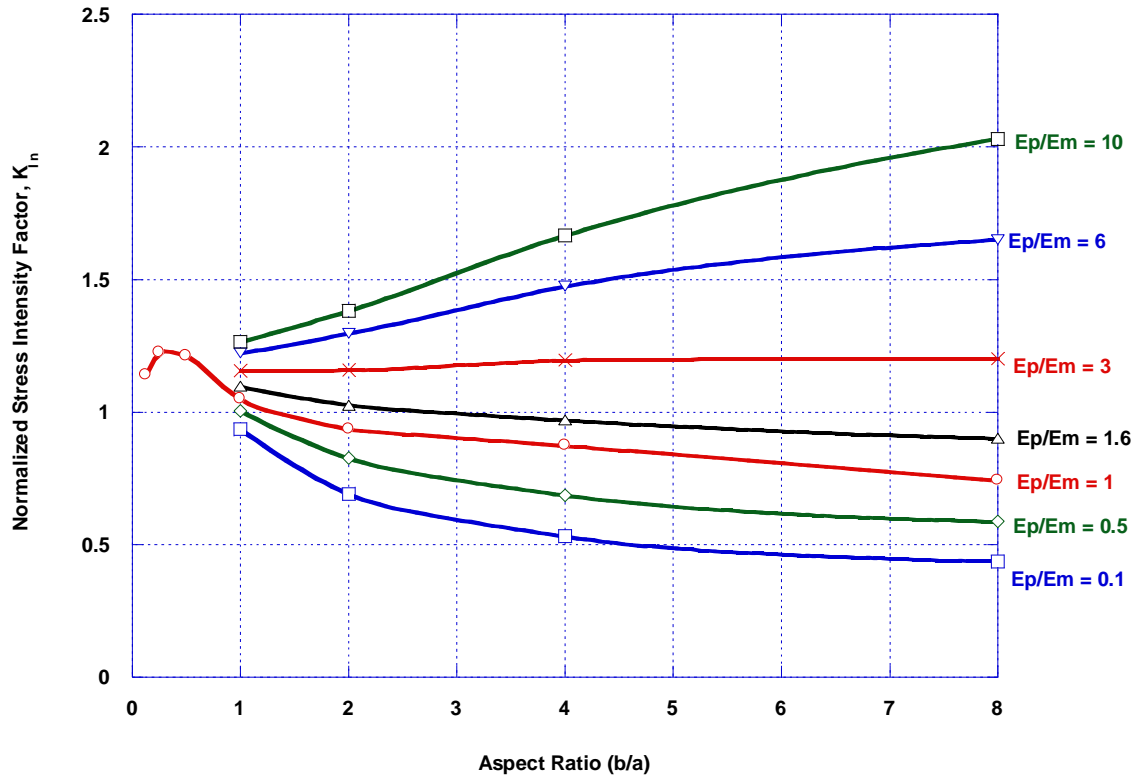
Figure 4.10 The analytic results of Figure 4.9, for Ep/Em=1, plotted with finite element results for normalized stress intensity factor, for b/a = 1 to 8, for Ep/Em values ranging from 0.1 to 10.

Chapter 5

Comparison of Intermetallic Layer and Particle Fracture

5.1 CHAPTER INTRODUCTION

In Chapter 2, it was observed, for the GALVALUME^R coating system, that the intermetallic alloy layer between the coating matrix and steel substrate cracks extensively under applied tension, but those cracks do not propagate into the coating matrix or the substrate. This suggests that the lengths of these cracks are below a critical size required for crack extension. If so, then it should be possible, by comparing stress intensity factors for intermetallic layer cracks with stress intensity factors for cracks resulting from particle fracture, to estimate particle sizes for which matrix crack propagation should not occur. In Chapter 5, two-dimensional finite element models are used to calculate stress intensity factors for cracks extending through the intermetallic layer. These results are then compared with the results of Chapter 4 to estimate particle sizes for which matrix crack propagation should not occur. While these results are estimates subject to some degree of uncertainty, they outline a methodology that could be used to minimize or prevent crack propagation from fractured particles.

5.2 LIMITATIONS ON PARTICLE SIZE ESTIMATION

The primary limitation on using intermetallic layer cracks as a basis for estimating particle sizes for which matrix crack propagation will not occur is the lack of knowledge of the constitutive properties of the intermetallic layer. Stress intensity factors for cracks through the intermetallic layer will depend on the elastic properties of the layer and these

quantities cannot be measured for the nominally 2 micron thick layer. The layer is an iron-zinc-aluminum-silicon alloy that forms between the coating matrix and steel substrate as the coating solidifies. A rule-of-mixtures approach would suggest that the properties of the intermetallic layer might lie somewhere between the extremes given by the values for aluminum and steel. While this approach is used to estimate stress intensity factors, uncertainty regarding the constitutive properties results in the analysis having more qualitative value than quantitative.

5.3 ESTIMATION OF CRITICAL PARTICLE SIZES

The estimation of critical maximum particle sizes below which matrix crack propagation should not occur was done by first estimating stress intensity factors for cracks extending through the intermetallic layer and beyond the interface with the coating matrix by a distance of one tenth the intermetallic half-thickness, similar to what was done for the modeling of cracks through silicon particles in Chapter 4. The stress intensity factors determined for the ellipsoidal silicon particles in Chapter 4 were then scaled to match the stress intensity factor of the intermetallic layer cracks, giving a range of particle sizes for which crack propagation should not occur.

5.3.1 Finite element simulation of intermetallic layer cracks

From metallographic examination, Chapter 2, the thickness of the intermetallic layer was determined to be roughly 2 micron (79 μin). As was the case for the silicon particle models of Chapters 3 and 4, the intermetallic layer thickness was too small to model

directly. Instead a model of a proportionally larger system was used to estimate the stress intensity factor and this result was then scaled to the intermetallic layer thickness.

The two-dimensional finite element mesh used to simulate a crack through the intermetallic layer is shown in Figures 5.1 through 5.3. The model was verified by comparing the finite element prediction for stress intensity factor with the analytic solution for a crack in an infinite plate ($K_I = \sigma\sqrt{\pi a}$) for a homogenous case with constitutive properties of aluminum used for all regions of the model and the results matched to within 0.1%. The model was then used to estimate the stress intensity factor for the crack tip extending a/10 into the coating matrix. This result was then scaled to the intermetallic layer thickness using the dependence of stress intensity factor on $a^{1/2}$.

The results from Chapter 4, for stress intensity factors resulting from fractured silicon particles also have a dependence on the crack length to the one half power. These results were scaled to determine crack sizes, and thus particle sizes, that matched the stress intensity factor determined for the intermetallic layer. The resulting particle sizes are shown in Tables 5.1 through 5.3 for cases in which the Young's modulus of the intermetallic layer was set to the values for aluminum, silicon, and steel, respectively.

While the lack of knowledge of the constitutive properties of the intermetallic layer limits the analysis, examination of the results along with microstructural observations of GALVALUME[R] coating suggest that the results shown in Table 5.1 using the properties of aluminum for the intermetallic layer may be the most reasonable because the critical maximum particle sizes for which matrix crack propagation would not occur become progressively more inconsistent with observations of GALVALUME[R] coating fracture as the modulus of the intermetallic layer is increased. Furthermore, the rule-of-mixtures

approach suggests that the particle sizes represent a reasonable upper bound on the particle sizes because it is likely that the modulus is no less than the modulus of aluminum so, at least from this point of view, cracks resulting from the fracture of particles smaller than those listed in Tale 5.1 should not propagate into the matrix.

5.4 CONCLUSIONS

In Chapter 5, finite element models were used to estimate stress intensity factors for cracks through the intermetallic layer of the GALVALUME^R coating system. Metallographic observation has shown that these cracks do not propagate into the coating matrix. The stress intensity factors calculated in Chapter 4, to evaluate the likelihood of crack propagation from fractured particles, were then scaled to match the stress intensity factor calculated for the intermetallic layer. This scaling was then used to estimate particle sizes for which crack propagation should not occur. The calculation of these particle sizes depends on the constitutive properties of the intermetallic layer and these properties are not known. While this uncertainty limits the quantitative value of the results, the contribution of Chapter 5 is to show how critical maximum particle sizes, below which crack propagation would not occur, could be determined for this type of material system.

Table 5.1

Particle dimensions estimated by equating stress intensity factors from the 2 micron (79micro-inch) thick intermetallic layer to constant volume silicon particles with aspect ratios ranging from 1/8 to 8, with Young's modulus of the intermetallic layer estimated to be 10 Msi.

Aspect Ratio (b/a)	2b (micro-inch)	2a (micro-inch)	2b (micron)	2a (micron)
1/8	71	568	1.80	14.42
1/4	77	308	1.96	7.83
1/2	85	170	2.15	4.31
1	151	151	3.85	3.85
2	274	137	6.96	3.48
4	488	122	12.39	3.10
8	898	112	22.81	2.85

Table 5.2

Particle dimensions estimated by equating stress intensity factors from the 2 micron (79micro-inch) thick intermetallic layer to constant volume silicon particles with aspect ratios ranging from 1/8 to 8, with Young's modulus of the intermetallic layer estimated to be 16 Msi.

Aspect Ratio (b/a)	2b (micro-inch)	2a (micro-inch)	2b (micron)	2a (micron)
1/8	119	949	3.01	24.10
1/4	129	515	3.27	13.09
1/2	142	283	3.60	7.20
1	253	253	6.43	6.43
2	458	229	11.63	5.82
4	815	204	20.71	5.18
8	1501	188	38.12	4.77

Table 5.3

Particle dimensions estimated by equating stress intensity factors from the 2 micron (79micro-inch) thick intermetallic layer to constant volume silicon particles with aspect ratios ranging from 1/8 to 8, with Young's modulus of the intermetallic layer estimated to be 30 Msi.

Aspect Ratio (b/a)	2b (micro-inch)	2a (micro-inch)	2b (micron)	2a (micron)
1/8	263	2108	6.69	53.54
1/4	286	1145	7.27	29.08
1/2	315	630	8.00	15.99
1	562	562	14.28	14.28
2	1017	509	25.84	12.92
4	1811	453	46.00	11.50
8	3334	417	84.68	10.59
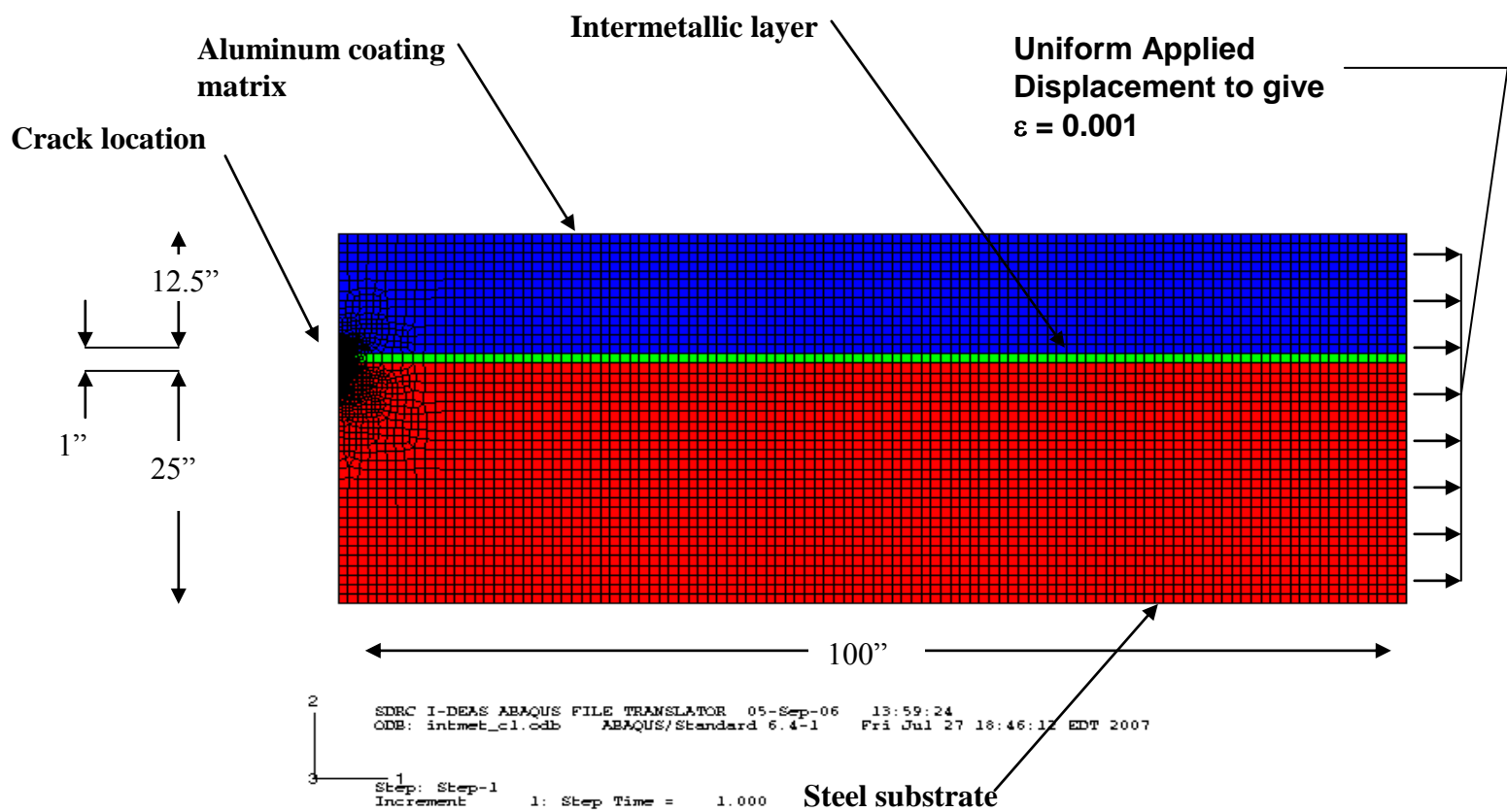
Figure 5.1   Two-dimensional element mesh used to predict stress intensity factors for a
crack extending through the intermetallic layer.
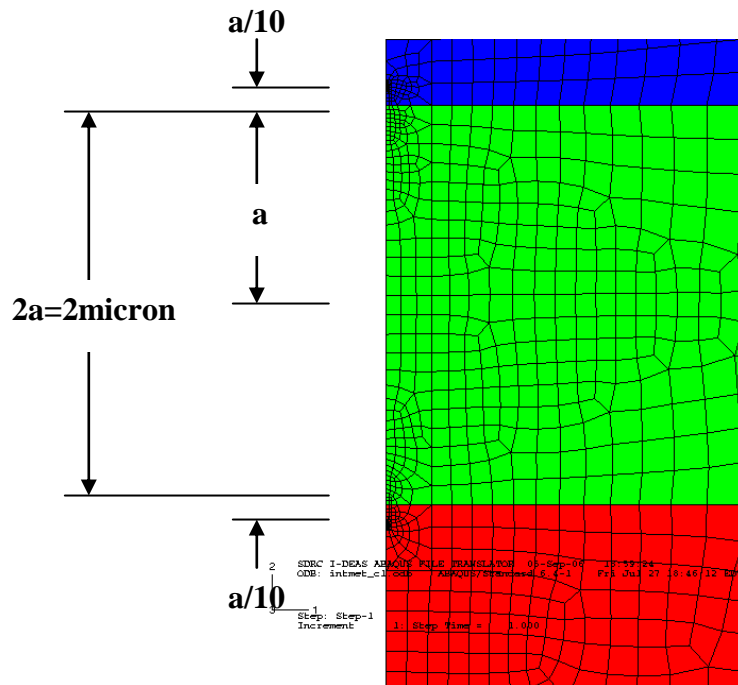
Figure 5.2   The crack tip extended a distance of a/ 10 beyond the interface between the intermetallic layer and the coating matrix. The crack tip was also extended a/10 beyond the interface with the substrate.
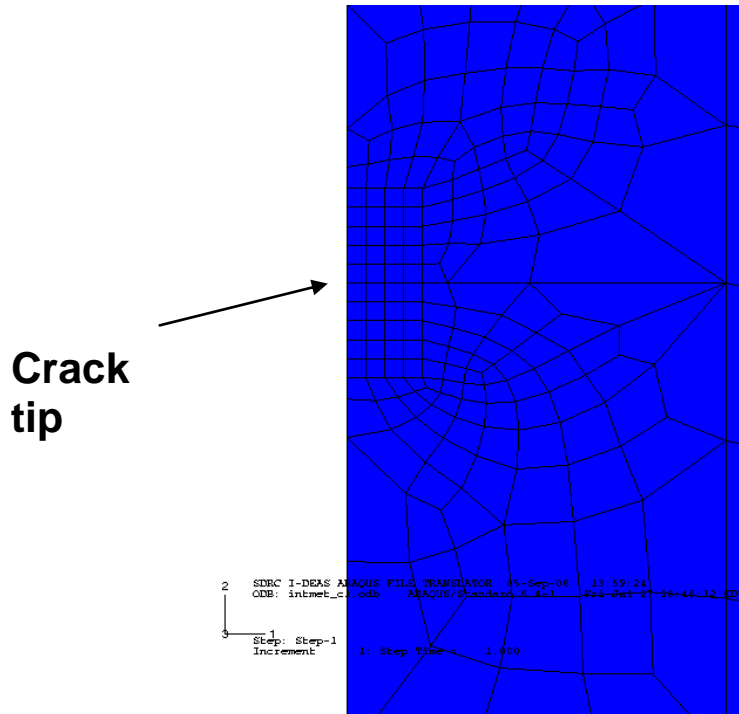
Crack tip

Figure 5.3   Fine mesh region at the crack tip location. The smallest elements at the crack tip location had elements lengths of 0.0001" (model dimension).

Chapter 6

Summary and Conclusions

The topic of this dissertation was initially motivated by the fracture mechanism of commercial GALVALUME^R coatings, in which particle fracture serves as the initial event leading to failure of the coating system. Metallographic analysis and literature review revealed that the failure mode of the GALVALUME^R coating system is similar to and representative of failure in particle reinforced metal matrix composites as well as multiphase metal alloys. It was observed that the effects of particle shape and material property mismatch between particles and matrix on the failure of a composite system had not been systematically addressed. The primary goal of this dissertation was to systematically describe the effect of particle shape and material property mismatch on the initial particle fracture event and on crack propagation from fractured particles, leading to the overall failure of the composite system. The following sections summarize the contributions of this dissertation in attaining this goal.

6.1 FACTORS CONTROLLING PARTICLE FRACTURE

Literature review and the findings of Chapter 2 indicated that particle fracture was influenced by particle shape and material property mismatch but no systematic studies of these effects were found. In Chapter 3, finite element modeling was used to evaluate these effects. In the models, particles were represented as a series of ellipsoidal shapes and the potential for fracture of these shapes was evaluated by examining trends in stress intensity factors for cracks within the particles as they were affected by the

particle/matrix interface. The research documented in Chapter 3 resulted in a number of contributions applicable to particle fracture in a composite system in understanding the behavior of a crack approaching a bi-material interface. The research conducted represents the first systematic Fracture Mechanics analysis of the fracture of brittle particles in a two-phase system. This work demonstrated how the classical Eshelby Problem can be extended to particle fracture and mapped out how the fracture problem transitions from homogenous continuum behavior when cracks are unaffected by the particle/matrix interface to asymptotic behavior as cracks approach and become affected by the particle/matrix interface. It was shown that the asymptotic behavior of stress intensity factor near the particle/matrix interface changes with particle shape. The effect of the particle/matrix interface on stress intensity factor extends further into particles from the interface as aspect ratio is reduced and the gradient in stress intensity factor for cracks approaching the interface reduces. The trends shown for this work build upon existing work documenting the behavior of cracks approaching a linear bi-material interface and show how cracks behave, in terms of trends in stress intensity factor, when approaching curved three-dimensional interfaces.

It was shown that whether a crack is "small" and unaffected by the interface, or "large" and affected by the interface depends on particle shape, crack location within in the particle and crack size in proportion to the particle size.

It was established that trends in stress intensity factor, in terms of relative ranking for potential for fracture or which particles exhibit higher or lower stress intensity factors, that occur when cracks are unaffected by the particle/matrix interface remain unchanged for cracks affected by the particle matrix interface for spheres and prolate spheroid

particles with aspect ratios greater than 1. As a consequence, the relative potential for fracture of particles having flaws of similar size and proximity to the interface can be ranked on the basis of Eshelby stress alone, without considering the fracture problem near the particle matrix interface, providing a simple means for assessing the potential for particle fracture. For prolate spheroid particles having aspect ratios less than 1 it was shown that exceptions to the trends in relative potential for particle fracture may exist if the initial flaws are large enough.

6.2 FACTORS CONTRLLING THE ONSET OF MATRIX CRACK PROPAGATION

In Chapter 3, the fracture of ellipsoidal particles was investigated. In Chapter 4, the modeling of the fracture of ellipsoidal particles was extended to consider the onset of crack propagation into the surrounding matrix from fractured particles. This was done by comparing stress intensity factors for cracks extending beyond the particle/matrix interface and into the matrix. The contribution of this work is to map out the relationship between particle shape, Young's modulus mismatch, and the onset of crack propagation and to specifically show that the onset of crack propagation is strongly dependent on the combined effects of the sizes of cracks that resulting from particle fracture and the Young's modulus mismatch between the particles and matrix. As the Young's modulus mismatch between the particles and matrix increases, long, thin particles become most prone to crack propagation into the matrix. Such particles were also determined to be most prone to fracture for particles stiffer than the matrix, meaning that they represent the greatest potential for failure of the composite particle/matrix system when particles are much stiffer than the matrix. It was also shown that cases exist where the particle most

prone to fracture can also be the least likely to result in crack propagation into the matrix, thus illustrating the complexity of composite system failure.

6.3 COMPARISON OF INTERMETALLIC LAYER AND PARTICLE FRACTURE

In Chapter 5, finite element models were used to estimate stress intensity factors for cracks through the intermetallic layer of the GALVALUME^R coating system. This was done by scaling stress intensity factors calculated in Chapter 4, to evaluate the likelihood of crack propagation from fractured particles, to match the stress intensity factor calculated for the intermetallic layer. While uncertainty due to lack of knowledge of the constitutive properties of the intermetallic layer limited the quantitative value of the results, the contribution of Chapter 5 is to show how critical maximum particle sizes, below which crack propagation would not occur, could be determined for this type of material system.

6.4 FUTURE WORK

The analyses conducted in this dissertation considered a range of ellipsoidal particle shapes that consisted of prolate spheroids and spheres. Finite element simulations of cracks within the particle cross sections could not be conducted for cases of prolate spheroids with the long axes of the particles oriented normal to the direction of load (aspect ratios less than 1) because the elliptical cross sections (normal to the loading direction) prevented the use of axisymmetric element meshes. Because of this, the effect of particle shape on the near interface behavior of stress intensity factor could not be

evaluated, and could only be inferred from simulations conducted for aspect ratios of 1 and higher. Particle shape effects on stress intensity factor could be further explored by considering oblate spheroids. Such shapes would have circular cross sections normal to the loading direction and shorter (as compared to prolate spheroids with aspect ratios of 1 and higher) elliptical cross sections parallel to the loading direction. Cracks in such particles could be simulated with axisymmetric finite element models and would provide additional insight into particle shape effects on the near interface behavior of stress intensity factor for particles having relative lengths, with respect to the loading direction, shorter than those considered in the present analysis.

The analysis could also be extended to consider multiple particles that are close together and to consider yielding in the matrix. Both of these cases would result in non-uniform stresses in the particles, increasing the complexity of the particle fracture problem.

References

1. M. Finot, Y. –L. Shen, A. Needleman, S. Suresh, "*Micromechanical Modeling of Reinforcement Fracture in Particle Reinforced Metal-Matrix Composites,*" Metallurgical and Materials Transactions A, vol. 25A, November, 1994, pp. 2403-2420.

2. S. G. Song, N. Shi, G. T. Gray III, J. A. Roberts, "*Reinforcement Shape Effects of the Fracture Behavior of 6061-Al Matrix Composites,*" Metallurgical and Materials Transactions A, vol. 27, November, 1994, pp. 3739 3746.

3. A. Needleman, "*A Continuum Model for Void Nucleation by Inclusion Debonding,*" Journal of Applied Mechanics, vol. 54, September, 1987, pp. 525-531.

4. Y. Brechet, J. D. Embury, S. Tao, L. Luo, "*Damage initiation in metal matrix composites,*" Acta Metallurgica and Materialia, vol. 39, no. 8, 1991 pp. 1781-1786.

5. M. S. Hu, "*Some effects of particle size on the flow behavior of Al-SiCp Composites,*" Scripta Metallurgica et Materialia, vol.25, pp. 695-700, 1991.

6. W. H. Hunt, Jr., J. R. Brockenbrough, P. E. Magnusen, "*An Al-Si-Mg composite model system: microstructural effects on deformation and damage evolution,*" Script Metallurgica et Materialia, vol. 25, pp.15-20, 1991.

7. G. Bao, "*Damage due to fracture of brittle reinforcements in a ductile matrix,*" Acta Metallurgica et Materialia, vol.40, no. 10, pp. 2547-2555, 1992.

8. M. T. Kaiser, "*Plastic flow and fracture of a particulate metal matrix composite,*" Acta Materialia, vol. 44, no. 9, pp. 3465-3476.

9. X. Q. Xu, D. F. Watt, "*A Numerical Analysis of the Effects of Reinforcement Content on Strength and Ductility in Al/(SiC)p MMCs,*" Acta Materialia, vol.44, no. 11, pp. 4501-4511, 1996.

10. S. Ghosh, S. Moorthy, "*Particle Fracture Simulation in Non-Uniform Microstructures of Metal Matrix Composites,*" Acta Materialia, vol. 46, no. 3, pp.965-982, 1998.

11. P. Scarber, Jr., G. M. Janowski, "*Finite Element Analysis of Reinforcement Particle Cracking in Al/SiCp Composites,*" Materials Science and Technology, vol. 17, pp. 1339-1346, Novemeber 2001.

12. D. Steglich, W. Brocks, "*Micromechanical Modeling of the Behaviour of Ductile Materials Including Particles*," Computational Materials Science, vol. 9, pp. 7-17, 1997.

13. H. J. Bohm, W. Han, A. Eckschlager, "*Multi-Inclusion Unit Cell Studies of Reinforcement Stresses and Particle Failure in Discontinuously Reinforced Ductile Matrix Composites*," Computer Modeling in Engineering and Sciences, vol. 5, no. 1, pp. 5-20, 2004.

14. M. D. Dighe, A. M. Gokhale, M. F. Horstmeyer, "*Effect of Loading Condition and Stress State on Damage Evolution in an Al-Si-Mg Base Cast Alloy*," Metallurgical and Materials Transactions A, vol. 33a, pp. 555-565, March 2002.

15. C. Li, F. Ellyin, "*A Micro-Macro Correlation Analysis for Metal Matrix Composites Undergoing Multi-Axial Damage*," International Journal of Solids and Structures, vol. 35, no. 7-8, pp. 637-639, 1998.

16. C. Maldonado, Y. Zhai, S. Sathian, T. H. North, "*Particle Fracture in Metal-Matrix Composite Friction Joints*," Proceedings from Materials Conference '98 on Joining of Advanced and Specialty Materials, 12-15 October 1998, Rosemont, Illinois, pp. 155-162.

17. M. F. Horstmeyer, S. Ramaswamy, M. Negrete, "*Using a Micromechanical Finite Element Parametric Study to Motivate a Phenomenoligical Macroscale Model for Void/Crack Nucleation in Aluminum with a Hard Second Phase*," Mechanics of Materials 35, pp. 675-687, 2003.

18. K. Gall, M. Horstmeyer, D. L. McDowell, J. Fan, "*Finite Element Analysis of the Stress Distributions Near Damaged Si Particle Clusters in Cast Al-Si Alloys*," Mechanics of Materials, vol. 32, no. 5, pp. 277-301, 2000.

19. S. H. Goods, L. M. Brown, "*The Nucleation of Cavities by Plastic Deformation*," Acta Metallurgica, vol. 27, pp. 1-15, 1979.

20. V. A. Romanova, R.R. Balokhonov, S. Schmauder, "*The influence of reinforcing particle shape an interface strength on the fracture behavior of a metal matrix composite*," ACTA Materialia 57, pp. 97-107, 2009.

21. I. Justice, P. Poza, J. L. Martinez, J. Llorca, "*Reinforcement Stresses during Deformation of Sphere and Particulate-Reinforced Al Matrix Composites*," Metallurgical and Materials Transactions A, vol. 27A, pp. 486-490, February 1996.

22. Y. –T. Cho, "*Elastic Analysis of a Cracked Ellipsoidal Inhomogeneity in an Infinite Body*," KSME International Journal, vol. 15, no. 6, pp. 709-719, 2001.

23. J. Llorca, J. L. Martinez, M. Elices, "*Reinforcement Fracture and Tensile Ductility in Sphere-Reinforced Metal-Matrix Composites*," Fatigue and Fracture in Engineering Materials and Structures, vol. 20, no. 5, pp. 689-702, 1997.

24. W. Han, A. Echschlager, H. J. Bohm, "*Effects of Three Dimensional Multi-Particle Arrangements on the Mechanical Behavior and Damage Initiation of Particle-Reinforced MMC's*," Composites Science and Technology 61, pp. 1581-1590, 2001.

25. A. Eckschlager, W. Han, H. J. Bohm, "*A Unit Cell Model for Brittle Fracture of Particles Embedded in a Ductile Matrix*," Computational Materials Science 25, pp. 85-91, 2002.

26. P. E. McHugh, P. Connoly, "*Modeling the Thermo-Mechanical Behaviour of an Al Alloy-SiCp Composite, Effects of Particle Shape and Microscale Fracture*," Computational Materials Science 3, pp. 199-206, 1994.

27. J. Zhai, M. Zhou, "*Micromechanical Modeling of Mixed-Mode Crack Growth in Ceramic Composites*," Proceedings of the 1998 Symposium on Mixed-Mode Crack Behavior, ASTM Special Technical Publication n1359, pp. 174, 1999.

28. P. M. James, M. Ford, A. P. Jivkov, "*A novel particle failure criterion for cleavage fracture modeling allowing measured brittle particle distributions*," Engineering Fracture Mechanics 121-122, pp. 98-115, 2014.

29. S. R. Ortner, "*The ductile-to-brittle transition in steels controlled by particle cracking*," Fatigue and Fracture of Engineering Materials and Structures 29, pp752-769, 2006.

30. A. Hauert, A. Rossoll, A. Mortensen, "*Ductile-to-brittle transition in tensile failure of particle-reinforced metals*," Journal of the Mechanics and Physics of Solids 57, pp. 473-499, 2009.

31. Eshelby, J. D., "*The determination of the elastic field of an ellipsoidal inclusion, and related problems*," Proceedings of the Royal Society of London, Series A., vol. 241, pp. 377-397, 1957.

32. H. Tada, P. C. Paris, G. R. Irwin, "*The Stress Analysis of Cracks Handbook, 2nd ed.*," 1985, Del Research Corporation.

33. J. L. Beuth, "*Cracking of Thin Bonded Films in Residual Tension*," International Journal of Solids and Structures, vol. 29, no. 13, pp. 1657-1675, 1992.

34. M-C Lu, F. Ergodan, "*Stress Intensity Factors in Two Bonded Elastic Layers Containing Cracks Perpendicular to and on the Interface-Part I. Analysis,*" NASA Contractor Report 159218, January, 1980.

35. M-C Lu, F. Ergodan, "*Stress Intensity Factors in Two Bonded Elastic Layers Containing Cracks Perpendicular to and on the Interface-Part II. Solution and Results,*" NASA Contractor Report 159219, January, 1980.

36. F. Ergogan, G. D. Gupta, "*The Inclusion Problem with a Crack Crossing the Boundary,*" International Journal of Fracture, vol. 11, no. 1, February, 1975, pp. 13-27.

37. X. -P. Xu, A. Needleman, "*Numerical simulations of fast crack growth in brittle solids,*" Journal of the Mechanics and Physics of Solids, vol. 42, no. 9, 1994, pp. 1397-1434.

38. J. Zuo, M. A. Sutton, X. Deng, "*Basic studies of ductile failure processes and implications for fracture prediction,*" Fatigue and Fracture in Engineering Materials and Structures, vol. 27, 2004, pp. 231-243.

39. V. Tvergaard, J. W. Hutchinson, "*The relation between crack growth resistance and fracture process parameters in elastic-plastic solids,*" Journal of the Mechanics and Physics of Solids, vol.40, no. 6, pp.1377-1397, 1992.

40. Y. –L. Shen, J. J. Williams, G. Piotrowski, N. Chawla, Y. L. Guo, "*Correlation between Tensile and Indentation Behavior of Particle-Reinforced Metal Matrix Composites: and Experimental and Numerical Study,*" Acta Materialia, vol. 49, no. 6, pp. 3219-3229, 2001.

41. J. Hohe, S. Goswami, W. Becker, "*Assessment of Interface Stress Concentrations in Layered Composites with Application to Sandwich Panes,*" Computational Materials Science 26, pp. 71-79, 2003.

42. C. Li, F. Ellyin, "*Short Crack Trapping/Untrapping in Particle-Reinforced Metal-Matrix Composites,*" Composites Science and Technology 52, pp. 117-124, 1994.

43. Y. Xue, J. Que, "*On the Energy Release Rate of Elliptical Cracks in Anisotropic Elastic Media,*" Chinese Journal of Mechanics-Series A, vol. 19, no. 1, pp. 233-239, March 2003.

44. H. H. Yu, J. W. Hutchinson, "*Influence of Substrate Compliance on Buckling Delamination of Thin Films,*" International Journal of Fracture 113, pp. 34-55, 2002.

45. C. I. A. Thomson, M. J. Worswick, A. K. Pilkey, D. J. Lloyd, "*Void Coalescence within Periodic Clusters of Particles,*" Journal of the Mechanics and Physics of Solids, vol. 51, pp. 127-146, 2003.

46. H. Berns, C. Broeckmann, D. Weichert, "*Frackture Mechanisms in Particle Reinforced Metal Matrix Composites,*" IFCAP95, Failure Analysis and Prevention, International Conference Proceedings, pp. 219-224, 1995.

47. Broek, D., "*Elementary Engineering Fracture Mechanics, 4th ed.,*" 1987, Martinus Nijhoff**.**

48. S. J. Bianculli, "*Preliminary Evaluation of the Fracture Resistance of GALVALUME Coatings*," U. S. Steel Research Memorandum, August 8, 2001.